ORBITAL SELECTIVE MOTT TRANSITION IN $3D$ AND $5F$ MATERIALS

BY ANTONINA TOROPOVA

A dissertation submitted to the
Graduate School—New Brunswick
Rutgers, The State University of New Jersey
in partial fulfillment of the requirements
for the degree of
Doctor of Philosophy
Graduate Program in Physics and Astronomy

Written under the direction of
Professor Gabriel Kotliar
and approved by

_____

_____

_____

_____

_____

New Brunswick, New Jersey

October, 2007

ABSTRACT OF THE DISSERTATION

Orbital selective Mott transition in $3d$ and $5f$ materials

by Antonina Toropova

Dissertation Director: Professor Gabriel Kotliar

We study two types of strongly correlated electron systems in the example of the transition oxide CrO_2 and actinide series. We found that the physics of both types of materials can be interpreted and discussed using concept of orbital selective Mott transition (OSMT). The theory of OSMT is discussed in framework of the multiorbital Hubbard model applied to the description of t_{2g} orbitals of Cr atoms in chromium dioxide as well as in the framework of a more generalized model for $5f$ materials containing both Hubbard-like and Anderson-like contributions.

The electronic structure, transport, and magnetic properties of selected compounds are investigated by means of *Ab Initio* calculations. The many body techniques such as LDA+U and dynamical mean field theory (DMFT) have been used in addition to density functional based local density approximation (LDA) method.

The half-metallic ferromagnet CrO_2 has been shown to demonstrate effectively weakly correlated behavior in ordered state due to big exchange splitting within t_{2g} orbitals. The detailed DMFT study with Quantum Monte Carlo (QMC)

impurity solver revealed that in the paramagnetic state this compound was on the edge of a quantum transition.

In the case of the actinide series we first demonstrated the choice of basis which optimum for DMFT based calculations. By means of detailed one-electron band structure analysis we showed that hybridization term of $5f$-orbitals with conduction electrons must be included in the actinide Hamiltonian due to permanent presence of uncorrelated states at Fermi level. We conclude study of $5f$-materials presenting tight-binding parametrization and exploring magnetic characteristics.

Acknowledgements

Foremost, I would like to thank my advisor Gabi Kotliar for expert guidance of my research, and for his encouragement and support at all levels. I am very grateful to Chris Marianetti for useful discussions and productive collaboration, for sharing his knowledge and ideas with me. His motivation and enthusiasm helped me a lot to bring this work to conclusion. Thanks to Kristjan Haule, who has been actively interested in my research and always had time to answer my questions. I would like to thank my collaborators Viktor Oudovenko and Sergej Savrasov for their help and encouragement.

I am thankful to present and past members of our group: Alberto Camjayi, Luca De' Medici, Jean-Christophe Domenge, Kasturi Basu, Lorenzo De Leo, Maria Carolina Aguiar, Ping Sun, Thomas Eckert, Marcello Civelli and Sahana Murthy for the friendship and support during my PhD years.

I would like to thank Natan Andrei, Premi Chandra and Aram Mekjian for acting as members of my Ph.D. committee. I want to thank Ron Ransome for his support as graduate director. Thanks to all members of the Department of Physics and Astronomy at Rutgers University for providing an excellent and inspiring working atmosphere.

Many thanks to my friends in physics: Elena Loguinova, Ruslan Usmanov, German Popov, Nikolai Klimov, Marianna Maltseva. To the many friends I made at Rutgers: thanks for making my staying at Rutgers a pleasant experience.

I am grateful for the support and encouragement of my friends outside of Rutgers: Olga Bushueva, Julia Gilman, Dima Volya, Nastya Prochorova, David Ananikian, Alena Lazovskaya, Julia Polovnikova.

Finally, I address my eternal thanks to my family for their love, understanding, patience, encouragement, and support when I most need it. As a small token of my love for them, and of my gratitude for all they have sacrificed for me, I dedicate this dissertation to my mother Lidia and my sister Anna.

Antonina Toropova

Rutgers University

October 2007

Dedication

To Lidia and Anna.

Table of Contents

List of Tables

List of Figures

Introduction

The main goal of condensed matter physics is to understand and accurately describe various states of matter and possible transitions between them. The last one and a half centuries of discovery shows that generally, with rare exceptions, new ideas in the solid state physics come from experimental observations. In keeping with this trend, in the last two decades the discovery of heavy fermion compounds and high- temperature superconductivity has revolutionized condensed matter physics and well-established views on the role of correlations between electrons. Ever-growing classes of materials that lie outside of the conventional weakly-interacting solid-state paradigm stimulated the explosion in theoretical proposals for novel quantum states involving spin, orbital, charge, and ionic degrees of freedom.

The fundamental basis for understanding materials ultimately rests upon understanding their electronic structure [16]. The challenge for the electronic structure theory is that on one hand it requires detailed modelling of real materials involving such specifics as atomic charge and lattice structure, but on the other hand must provide universal quantitative methods which are not limited to any particular type of bonding. With rapid advances in basic theory, new algorithms, and computational physics the field of electronic structure is at a momentous stage. Increasingly, electronic structure calculations are becoming tools used by both experimentalists and theorists to understand the characteristic properties of matter and to make the specific predictions for real materials and experimentally observable phenomena.

Now condensed matter physicists have a firm understanding of weakly correlated materials such as conventional metals and semiconductors. The quantitative techniques applicable to electronic structure calculations for these materials are developed and well tested. These techniques naturally fall into two categories designed, respectively, to describe electronic ground state and electronic excitation spectra. The the most popular "first principle" method used by electronic structure community to calculate ground state properties is density functional theory [17, 18], especially in the local density and generalized gradient approximations (LDA and GGA) [19]. These methods can also be effectively used as starting points for perturbative computation of one-electron spectra [20]. Even though density functional methods have been proved to be very successful in treating weakly correlated compounds they often fail to capture the correct physics in strongly correlated materials [21].

By strongly correlated electron systems one refers to complex materials, with electrons occupying active $3d$ (transition metals), $4f$ (lanthanides), or $5f$ (actinides) orbitals. The excitation spectra in these materials can not be described in terms of well-defined quasiparticles, making conventional band theory insufficient. The exploration of electronic structure of strongly correlated materials became possible with introduction of new concepts such as Hubbard bands and narrow coherent quasiparticle bands [21].

The exotic properties and complex phase diagram of strongly correlated materials result from competing interaction terms in their Hamiltonians. Thus, Mott-Hubbard metal-insulator transition [22, 23] one of the central topics of the strongly correlated field, originates from the competition between tendencies of the correlated electrons to delocalize due to their kinetic energy and localize due to the Coulomb interaction between them. The tendency to delocalize leads to the band formation and in the limiting case has a simple description in momentum space. On the other hand, tendency to localize leads to atomic-like behavior

which is well described in real space. The crossover is difficult to treat theoretically even on the level of models since the electron kinetic energy and interaction energy are of the same order of magnitude and there is no natural small parameter to develop perturbation theory around either metallic or atomic limits.

The dynamical mean field theory (DMFT) [21] is the framework which offers a minimal description of the electronic structure of correlated materials, treating both the atomic Hubbard bands and metallic quasiparticle bands on the same footing. This method is based on the mapping of the full many-body problem onto a quantum impurity model, which is essentially a small number of quantum degrees of freedom embedded in a bath that obeys a self-consistency condition [20]. DMFT studies of one-band Hubbard model dramatically improved understanding of bandwidth-controlled Mott-Hubbard transition [24, 25]. This success stimulated further application of the DMFT to investigate properties and phase diagrams of many other models, among them multiorbital Hubbard model [26, 27], periodic Anderson model [28, 29], and the Kondo lattice [29].

The necessity to understand and describe electronic structure of real strongly correlated compounds resulted in combinational method of LDA and DMFT (LDA+DMFT). This technique treats the light s, p (sometimes d) orbitals, which have extended wave functions, in the LDA and the localized d or f orbitals in the DMFT framework.

Further, the rich physics of real materials stimulated the investigations of Mott transition in more general models than one-band Hubbard model. Many strongly correlated materials, including the ones considered in this thesis, CrO_2 [30] and the actinide series materials [31], have partially filled bands of very different width near the Fermi level. In these circumstances, the nature and the scenario of transition from a weakly correlated metal to an insulating state with increasing interaction U is ambiguous and still not well understood. In particular, the question was raised whether all bands undergo a common transition

at the same critical Coulomb energy, or whether a separate, orbital-dependent, delocalization-localization transitions can take place in a subset of bands. The qualitative idea in the later scenario is that when two bands differ substantially in bandwidth, there should be a sequence of Mott transitions as the interaction strength is increased. First, the most narrow band undergoes a localization transition with a broader band remaining itinerant, while at large U both bands become localized. This phenomenon is known by the name orbital selective Mott transition (OSMT) and currently is a subject of numerous investigations in condensed matter community.

Most of the work so far has focused on the case of half-filled symmetric bands. The results are inconclusive yet. Even in the framework of DMFT, on the level of two-band Hubbard model there are studies reporting single Mott transition [27], and studies which have shown that OSMT is possible when ratio of the bandwidths of narrow and broad bands is small enough [32, 26, 33]. The source of this controversy might be hidden in the fact that in the vicinity of Mott transition different techniques, applied to solve the impurity problem, give slightly different values of critical U, and hence very different spectra for a given value of U [20].

In real materials the bands are not necessarily symmetric and their center of gravity may be shifted relative to each other. Crystal-field effects and the Coulomb exchange energy (J) affect the energy of on-site atomic states, which no longer depend only on the total local charge as in the orbitally degenerate case. A fundamental issue is how crystal-field splittings and spin-orbit splitting are renormalized by many-body interactions, since they both are relevant perturbations and can modify dramatically the nature of the OSMT.

This thesis deals with two selected classes of strongly correlated electron systems: chromium dioxide and the actinide series materials. We carry out realistic modelling of chosen materials adopting conventional electronic structure tools such as LDA, LDA+U, and DMFT, and developing new ones for the electronic

structure analysis. The considered compounds have in common the presence of unfilled bands with substantially different bandwidth at the Fermi level. Also, both systems are on the edge of localization-delocalization transition. Thus, we presumed that the interpretation of the physics of both types of materials within the concept of OSMT would provide original and fruitful discussion. In the case of CrO_2 we discuss possible scenarios of OSMT in the framework of the multiorbital Hubbard model applied to the description of t_{2g} orbitals of Cr atoms. In chapters devoted to actinides, we consider a Hamiltonian which includes terms of both multiorbital Hubbard model and the periodic Anderson model. Here the OSMT point of view is justified by the coexistence of broad $7s$, $6p$, $6d$, and narrow $5f$ bands near the Fermi level.

This thesis is organized as follows. In Chapter 1 we introduce *Ab Initio* methods used throughout the later chapters: LDA, GGA, LDA+U and DMFT. Chapter 2 is devoted to the ground state and transport properties of chromium dioxide. Despite its great technological importance [34] the electronic structure of this rare-earth oxide has not been previously understood. Here we address the problem of the importance of strong correlations for the electronic structure, transport and magnetic properties of half–metallic ferromagnetic CrO_2 by performing density functional electronic structure calculations in LDA scheme as well as using the LDA+U method. We show that the corresponding low–temperature experimental data are best fitted without accounting for the Hubbard U corrections. We conclude that the ordered phase of CrO_2 can be treated as weakly correlated.

In chapter 3 we proceed with a DMFT treatment of CrO_2 at finite temperatures. The Quantum Monte-Carlo technique has been applied to observed OSMT in this compound. Moreover, CrO_2 has been shown to be on the edge of a quantum transition.

Chapter 4 deals with the actinide series and presents detailed analysis of the one-electron band structure in the specific examples of curium, plutonium

and uranium. In Chapter 5 we perform a tight-binding (TB) parametrization of selected actinides. Here we show that the physics of actinides is governed by nearest-neighbor hoppings. The detailed comparison of our TB parametrization to the earlier reports in literature concludes chapter 5.

Curium is the first element from the actinide series experimentally known to develop a macroscopic magnetic moment. In chapter 6 we calculate the exchange constants and Néel temperature for this material and compare them to experimental values. We conclude in chapter 7 with a summary of the thesis, and directions for the future work.

Chapter 1

LDA, LDA+U and LDA+DMFT from the perspective of effective action formalism

Here, we use unified functional approach to introduce electronic structure methods, used in the later chapters of the thesis. First, we review the abstract concept of the effective action formalism. Then, we apply this concept to derive equations of the density-functional theory (DFT) in its local density approximation (LDA). Then we discuss methods that go beyond the LDA and designed to be applied to strongly correlated systems: LDA+U and LDA+DMFT.

1.1 Effective action formalism

Effective action as a term refers to a generalized action functional, constructed within concept of Legendre transformation. As a formalism, Legendre transformation is proven to be one of the most convenient and systematic techniques in discussing field theoretical many particle systems. It allows to rewrite theory by small number of selected variables [35].

The effective action approach for the density-functional theory was introduced by R. Fukuda *et al.* [35]. Then G. Kotliar *et al.* [20] demonstrated that the effective action formalism provides simple and intuitive construction of many other electronic structure methods, differing by the choice of observables or variables of interest. Thus, as we show below, density-functional theory is constructed with electron density being the observable. LDA+U introduces additional variables which are occupancy numbers for the correlated orbitals. In DMFT local Green's

function serves as a variable of interest.

Here we briefly sketch the idea of the effective action formalism. One begins with the partition function of the system,

$$Z = \exp(-F) = \int D[\psi^\dagger \psi] e^{-S}, \tag{1.1.1}$$

where F is free energy, S is the action for a given Hamiltonian, and ψ is a Grassman variable. Then one selects the observable A, and couples source J to this observable. The source J allows to probe the variable A and at the end of calculations will be set to zero. The modified action is $S' = S + AJ$, and the free energy $F[J]$ is now a functional of source J. A Legendre transformation is then used to eliminate the source in favor of the observable yielding a new functional,

$$\Gamma[A] = F[J[A]] - AJ[A]. \tag{1.1.2}$$

The variational derivative of $\Gamma[A]$ with respect to A yields J. Since we are free to set the source to zero, the extremum of $\Gamma[A]$ gives the free energy of the system.

The effective action approach is advantageous since useful approximations to the functional $\Gamma[A]$ can be constructed in practice using the inversion method [20]. The approach consists of carrying out systematic expansion of the functional $\Gamma[A]$ to some order in a parameter or coupling constant λ. The action is written as $S = S_0 + \lambda S_1$ and then a systematic expansion is carried out,

$$\Gamma[A] = \Gamma_0[A] + \lambda \Gamma_1[A] + \ldots, \tag{1.1.3}$$

$$J[A] = J_0[A] + \lambda J_1[A] + \ldots. \tag{1.1.4}$$

The system described by $S_0 + \lambda J_0$ reproduces the correct value of $\hat{A}$ by construction and can be considered as a reference system for the fully interacting problem. Moreover, when observable A is properly chosen other observables of

the system can be obtained perturbatively from their values in the reference system. $J_0[A]$ is a central quantity in this formalism and is referred as "constrained field".

Further, the functional $\Gamma[A]$ can be rewritten as,

$$\Gamma[A] = \Gamma_0[A] + \Delta\Gamma[A], \tag{1.1.5}$$

and since $\Gamma_0[A] = F_0[J_0] - AJ_0$, we can consider

$$\Gamma[A, J_0] = F_0[J_0] - AJ_0 + \Delta\Gamma[A] \tag{1.1.6}$$

as a functional which is stationary in two variables, the constraining field J_0 and A. The equation $\delta\Delta\Gamma/\delta A = J_0[A]$ together with the definition of $J_0[A]$ determines the exact constraining field for the problem.

In practice we decompose $\Delta\Gamma = E_H + E_{xc}$, where Hartree contribution E_H can usually be evaluated explicitly. The success of electronic structure method depends strongly on obtaining good approximations to the "generalized exchange correlation" E_{xc}.

In the subsequent sections we apply the abstract procedure described above to the derivation of the equations of density-functional based methods.

1.2 Density-functional theory

Density functional theory [17, 18] is very popular and basic tool to study weakly interacting electronic systems. Here, for the sake of transparency of the derivation, we construct non spin–polarized version of DFT first, generalizing to the relativistic case in the next section. The central quantity of DFT is the density of electrons $\rho(\mathbf{r})$. It is used as a physical variable in derivation of DFT functional. Let's consider a fermion system that is coupled to an external time-dependent

source field $J(x)$. Here $x = (\mathbf{r}, \tau, \sigma)$ denotes the space–imaginary time coordinates and spin. The action of the system is

$$S'[J] = S + \int dx J(x)\psi^\dagger(x)\psi(x), \tag{1.2.7}$$

where S is action without source

$$S = \int dx \psi^\dagger(x)\partial_\tau \psi(x) + \int d\tau H(\tau). \tag{1.2.8}$$

For the system consisting of electrons moving in a external potential $V_{ext}(x)$ and interacting via Coulomb interactions V the Hamiltonian H is

$$H = \sum_\sigma \int d\mathbf{r}\psi^\dagger_\sigma(\mathbf{r})[-\nabla^2 + V_{ext}(\mathbf{r}) - \mu]\psi_\sigma(\mathbf{r}) \tag{1.2.9}$$
$$+\frac{1}{2}\sum_{\sigma\sigma'} \int d\mathbf{r}d\mathbf{r}'\psi^\dagger(\mathbf{r})\psi^\dagger(\mathbf{r}')V(\mathbf{r}-\mathbf{r}')\psi(\mathbf{r}')\psi(\mathbf{r}).$$

μ stands for chemical potential, for the sake of conciseness we put it to zero through the entire chapter.

The partition function Z becomes a functional of the auxiliary source field J,

$$Z = \exp(-F[J]) = \int D[\psi^\dagger\psi]e^{-S'[J]}. \tag{1.2.10}$$

The effective action for the density, i.e. density functional is obtained as the Legendre transform of F with respect to $\rho(x)$:

$$\Gamma_{\mathrm{DFT}}[\rho] = F[J] - \int dx J(x)\rho(x). \tag{1.2.11}$$

The construction of standard DFT restricts source J to be time independent. The minimum of functional 1.2.11 gives the true density and the total energy. The density appears as the variational derivative of the free energy with respect to the source

$$\rho(\mathbf{r}) = \frac{\delta F}{\delta J(\mathbf{r})}. \tag{1.2.12}$$

To construct approximations to the functional Γ_{DFT} it is very useful to introduce the Kohn-Sham potential, V_{KS}, which is defined as the potential such that

when added to the non-interacting kinetic energy, it produces the given density in a reference system of non-interacting particles, i.e.

$$\rho(\mathbf{r}) = T\sum_{\sigma}\sum_{i\omega_n}\langle\sigma\mathbf{r}|(i\omega_n + \nabla^2/2 - V_{KS})^{-1}|\sigma\mathbf{r}\rangle e^{i\omega 0^+}. \tag{1.2.13}$$

The exact functional can now be viewed as a functional of two variables

$$\Gamma_{\mathrm{DFT}}(\rho, V_{KS}) = -T\sum_{i\omega_n} Tr\log(i\omega_n + \nabla^2/2 - V_{KS}) - \int V_{KS}(\mathbf{r})\rho(\mathbf{r})d\mathbf{r} \tag{1.2.14}$$
$$+\frac{1}{2}\int\frac{\rho(\mathbf{r})\rho(\mathbf{r}')}{|\mathbf{r}-\mathbf{r}'|}d\mathbf{r}d\mathbf{r}' + \int V_{ext}\rho(\mathbf{r})d\mathbf{r} + E_{xc}[\rho].$$

Further, $\Gamma_{\mathrm{DFT}}(\rho)$ is obtained by substituting $V_{KS}(\rho)$ as a solution of equation 1.2.13 (which makes 1.2.14 stationary) into $\Gamma_{\mathrm{DFT}}(\rho, V_{KS})$. $E_{xc}(\rho)$ is the exchange-correlation energy which is a functional of the density and not of the external potential.

Extremizing 1.2.14 with respect to ρ gives

$$V_{KS}(\mathbf{r})[\rho] = \int\frac{\rho(\mathbf{r})\rho(\mathbf{r}')}{|\mathbf{r}-\mathbf{r}'|}d\mathbf{r}d\mathbf{r}' + V_{xc}(\mathbf{r})[\rho] + V_{ext}(\mathbf{r})[\rho], \tag{1.2.15}$$

where $V_{xc}(\mathbf{r})$ is the exchange-correlation potential obtained as

$$\frac{\delta E_{xc}}{\delta\rho(\mathbf{r})} \equiv V_{xc}. \tag{1.2.16}$$

Since $E_{xc}(\rho)$ is not known explicitly some approximations are needed. The LDA assumes

$$E_{xc} = \int\rho(\mathbf{r})\epsilon_{xc}[\rho(\mathbf{r})]d\mathbf{r}, \tag{1.2.17}$$

where $\epsilon_{xc}[\rho(\mathbf{r})]$ is the exchange-correlation energy of the uniform electron gas, and is easily parameterized. In practice one frequently uses analytical formulas, which are empirically designed to fit a functional form to Quantum Monte Carlo (QMC) calculations. Particularly, in this thesis we used analytical approximation to $\epsilon_{xc}[\rho(\mathbf{r})]$ suggested by S. Vosko *et al* [36].

In the Chapter 6 of this thesis we also use Generalized Gradient approach (GGA). This approximation of DFT differs from LDA by the fact that E_{xc} is

considered as functional of two variables: $\rho(\mathbf{r})$ and $\nabla\rho(\mathbf{r})$. Since $\delta\nabla\rho(\mathbf{r}) = \nabla\delta\rho(\mathbf{r})$ the resulting expression for exchange potential is

$$V_{xc}(\mathbf{r}) = \left[\epsilon_{xc} + \rho\frac{\partial\epsilon_{xc}}{\partial\rho} - \nabla\left(\rho\frac{\partial\epsilon_{xc}}{\partial\nabla\rho}\right)\right]. \tag{1.2.18}$$

At zero-temperature the Fermi function is interpreted as step function, then equation 1.2.13 can be rewritten as

$$[-\nabla^2/2 + V_{KS}(\mathbf{r})]\psi_{\mathbf{k}j} = \epsilon_{\mathbf{k}j}\psi_{\mathbf{k}j} \tag{1.2.19}$$

$$\rho(\mathbf{r}) = \sum_{\mathbf{k}j} f(\epsilon_{\mathbf{k}j})\psi^{\dagger}_{\mathbf{k}j}(\mathbf{r})\psi_{\mathbf{k}j}(\mathbf{r}), \tag{1.2.20}$$

and V_{KS} is given as an explicit function of the density.

The total energy of the crystal is given as

$$E^{\mathrm{LDA}}_{tot} = \sum_{\mathbf{k}j} f(\epsilon_{\mathbf{k}j})\epsilon_{\mathbf{k}j} + \frac{1}{2}\int\frac{\rho(\mathbf{r})\rho(\mathbf{r}')}{|\mathbf{r}-\mathbf{r}'|}d\mathbf{r}d\mathbf{r}' \tag{1.2.21}$$
$$+ \int V_{ext}\rho(\mathbf{r})d\mathbf{r} + \int d\mathbf{r}\epsilon_{xc}[\rho(\mathbf{r})]\rho(\mathbf{r}) + E_{dc},$$

where

$$E_{dc} = -\int V_{KS}(\mathbf{r})\rho(\mathbf{r})d\mathbf{r} \tag{1.2.22}$$

simply subtracts the interaction energy from the Kohn-Sham eigenvalues which are explicitly included in the Hartree and exchange-correlation term to avoid double counting.

The density $\rho(r)$ is uniquely expressed in terms of the orbitals $\psi_{\mathbf{kj}}(\mathbf{r})$. In order to truncate the DFT, we introduce a finite basis set $\chi^{\mathbf{k}}_a(\mathbf{r})$ and expand

$$\psi_{\mathbf{k}j}(\mathbf{r}) = \sum_a \chi^{\mathbf{k}}_a A^{\mathbf{k}j}_a \tag{1.2.23}$$

keeping a finite set of a [37]. This truncation restricts the active part of the multiplicative operator associated with the potential V_{KS} to have a form

$$\hat{V} = \sum_{\mathbf{k}} |\chi^{\mathbf{k}}_a\rangle V_{a\beta}\langle\chi^{\mathbf{k}}_\beta|. \tag{1.2.24}$$

For a known potential V_{KS} this construction can be done once and for all. However, since V_{KS} depends on the density, the basis $\chi^{\mathbf{k}}_a$ is adapted iteratively to the self-consistent solution.

1.3 LDA+U and LDA+DMFT

The LDA method is very successful in many materials for which the one–electron model of solids works. However, in correlated electron system this is not always the case. In strongly correlated situations, the total energy is not very sensitive to the potential since the electrons are localized due to the interactions between themselves, and the lack of sensitivity of the functional to the density, does not permit to devise good approximations to the exact functional in this regime. DMFT is a method successfully describing strongly correlated systems [21] and has been extended to electronic structure problems [20].

Here we extend functional formulation of the local density approximation to the relativistic case, sometimes called local spin density approximation (LSDA) [38]. In this thesis we will refer by LDA to both non and spin–polarized versions of LDA method, except cases when it is separately emphasized. We first construct the most generalized functional representation of LDA+DMFT method and then introduce LDA+U as Hartree-Fock approximation of DMFT.

First of all, the relativistic extension of the density-functional approach requires introduction of the additional variable, namely the magnetic moment density $\mathbf{m}$. Further, to account for the strong electron correlation we introduce one more relevant variable, which is the local Green's function. The latter is defined by projecting the full Green's function onto a separate subset of correlated "heavy" orbitals distinguished by the orbital index a and the spin index σ from a complete set of orbitals $\chi_a^\sigma(\mathbf{r}-\mathbf{R}) \equiv \chi_{aR}^\sigma$ of a tight-binding representation which we assume for simplicity to be orthogonal. The local Green function is therefore given by a matrix $\hat{G}$ with elements [39]

$$G_{ab}^{\sigma\sigma'}(i\omega,\mathbf{R}) = -\left\langle c_{aR}^{\sigma}(i\omega) c_{bR}^{\sigma'+}(i\omega)\right\rangle = \tag{1.3.25}$$
$$-\int \chi_a^{\sigma*}(\mathbf{r}-\mathbf{R})\left\langle \psi(\mathbf{r},i\omega)\psi^+(\mathbf{r}',i\omega)\right\rangle \chi_b^{\sigma'}(\mathbf{r}'-\mathbf{R}) d\mathbf{r} d\mathbf{r}'.$$

We then construct a functional $\Gamma[\,\rho,\mathbf{m},\hat{G}\,]$ which gives the exact free energy at a

stationary point.

We consider a fermion system under an external potential V_{ext} and an external magnetic field $\mathbf{h}$. The spin-orbit coupling, whose effects are important for magnetic anisotropy calculations, is also considered. Spin-orbit coupling is included according to the suggestion by Andersen [40]. It is useful to introduce the notion of the Kohn-Sham potential V_{KS}, the Kohn-Sham magnetic field $\mathbf{h}_{KS}$ and its dynamical analog $\Sigma_{ab}^{\sigma\sigma'}(i\omega_n)$. They are defined as the functions that one needs to add to the kinetic energy matrix so as to obtain a given density and spectral function of the heavy orbitals namely:

$$\begin{aligned}\rho(\mathbf{r}) = \quad & T\sum_{i\omega_n} \mathrm{Tr}_s \left\langle \mathbf{r}s \right| [(i\omega_n + \nabla^2/2 - V_{KS})\mathrm{I} \\ & - 2\mu_B \mathbf{s}\cdot\mathbf{h}_{KS} - \xi(\mathbf{r})\mathbf{l}\cdot\mathbf{s} - \Sigma]^{-1} \left| \mathbf{r}s \right\rangle e^{i\omega_n 0^+}, \qquad (1.3.26) \\ \mathbf{m}(\mathbf{r}) = \quad & -2\mu_B T\sum_{i\omega_n} \mathrm{Tr}_s \left\langle \mathbf{r}s \right| \mathbf{s}[(i\omega_n + \nabla^2/2 - V_{KS})\mathrm{I} \\ & -2\mu_B \mathbf{s}\cdot\mathbf{h}_{\mathrm{KS}} - \xi(\mathbf{r})\mathbf{l}\cdot\mathbf{s} - \Sigma]^{-1} \left| \mathbf{r}s \right\rangle e^{i\omega_n 0^+}, \qquad (1.3.27)\end{aligned}$$

where Tr_s is the trace over spin space, $\mathbf{l}$ and $\mathbf{s}$ are one-electron orbital and spin angular momentum operator, respectively. The spin angular momentum operator is expressed in terms of Pauli matrices $\mathbf{s} = \vec{\sigma}/2$ and I is 2×2 unit matrix. V_{KS} and $\mathbf{h}_{KS}$ are functions of $\mathbf{r}$. The chemical potential μ is set to zero throughout the current chapter, and Σ is given by

$$\Sigma \equiv \Sigma(\mathbf{r}, \mathbf{r}', i\omega) = \sum_{ab\sigma\sigma'\mathbf{R}} \chi_a^{\sigma *}(\mathbf{r} - \mathbf{R})\Sigma_{ab}^{\sigma\sigma'}(i\omega)\chi_b^{\sigma'}(\mathbf{r}' - \mathbf{R}).$$

$\xi(\mathbf{r})$ determines the strength of spin–orbit coupling and in practice is determined [41] by radial derivative of the $l = 0$ component of the Kohn–Sham potential inside an atomic sphere:

$$\xi(r) = \frac{2}{c^2}\frac{dV_{KS}(r)}{dr}. \qquad (1.3.28)$$

When spin–orbit coupling is present, the intra–atomic magnetization $\mathbf{m}(\mathbf{r})$ is not collinear, i.e., the direction of magnetization depends on the position $\mathbf{r}$.

Therefore, the magnetization must be treated as a general vector field, due to the non-collinear intra-atomic nature of this quantity. Such a general magnetization scheme has been recently discussed [42].

In terms of these quantities and the matrix of local interactions $\hat{U}$, we write down the DMFT+LSDA functional:

$$\begin{aligned}
&\Gamma_{\mathrm{LSDA+DMFT}}(\rho, V_{\mathrm{KS}}, \mathbf{m}, \mathbf{h}_{\mathrm{KS}}, \hat{G}, \hat{\Sigma}) = \\
&-T\sum_{\omega} e^{i\omega 0^+} \mathrm{Tr}\log[(i\omega + \nabla^2 - V_{\mathrm{KS}})\mathrm{I} - 2\mu_B \mathbf{s}\cdot\mathbf{h}_{\mathrm{KS}} \\
&-\xi(\mathbf{r})\mathbf{l}\cdot\mathbf{s} - \Sigma] - \int d\mathbf{r} V_{KS}(\mathbf{r})\rho(\mathbf{r}) + \int d\mathbf{r}\mathbf{m}(\mathbf{r})\cdot\mathbf{h}_{\mathrm{KS}}(\mathbf{r}) \\
&-\sum_{\omega} e^{i\omega 0^+} \mathrm{Tr}[\hat{\Sigma}(i\omega)\hat{G}(i\omega)] + \int d\mathbf{r} V_{ext}(\mathbf{r})\rho(\mathbf{r}) \\
&-\int d\mathbf{r}\mathbf{h}(\mathbf{r})\cdot\mathbf{m}(\mathbf{r}) + \frac{1}{2}\int d\mathbf{r}d\mathbf{r}' \frac{\rho(\mathbf{r})\rho(\mathbf{r}')}{|\mathbf{r}-\mathbf{r}'|} \\
&+E_{\mathrm{xc}}^{\mathrm{LSDA}}[\rho, \mathbf{m}] + \sum_R [\Phi[\hat{G}] - \Phi_{DC}].
\end{aligned} \tag{1.3.29}$$

$\Phi[\hat{G}]$ is the sum of the two–particle irreducible local diagrams constructed with the local interaction matrix $\hat{U}$, and the local heavy propagator $\hat{G}$. Φ_{DC} is the double counting term which subtracts the average energy of the heavy level already described by LDA. Expression (1.3.29) ensures that the Green's function obtained from its extremization will satisfy the Luttinger theorem.

$E_{xc}^{\mathrm{LDA}}[\rho, \mathbf{m}]$ is the LDA exchange correlation energy. When a nontrivial magnetic moment is present, the exchange correlation energy functional is assumed to be dependent on density and magnetization:

$$E_{xc}^{\mathrm{LSDA}}[\rho, \mathbf{m}] = \int d\mathbf{r}\epsilon_{\mathrm{xc}}[\rho(\mathbf{r}),\ m(\mathbf{r})]\rho(\mathbf{r}) + \int d\mathbf{r} f_{xc}[\rho(\mathbf{r}), m(\mathbf{r})]\ m(\mathbf{r}), \tag{1.3.30}$$

where $m = |\mathbf{m}|$.

The functional (1.3.29) can be viewed as a functional of six independent variables, since the stationary condition in the conjugate fields reproduces the definition of the dynamical potential and the Weiss field. Extremizing it with respect

$V_{\rm KS}$, $\mathbf{h}_{\rm KS}$, and Σ lead us to compute the density 1.3.26, the magnetic moment density 1.3.27, and the Green's function $G^{\sigma\sigma'}_{ab}(i\omega)$ 1.3.34, respectively. The Kohn–Sham potential $V_{\rm KS}(\mathbf{r})$ and Kohn–Sham magnetic field $\mathbf{h}_{\rm KS}(\mathbf{r})$ are obtained by extremizing the functional with respect to $\rho(\mathbf{r})$ and $\mathbf{m}(\mathbf{r})$:

$$V_{\rm KS}(\mathbf{r}) = V_{\rm ext}(\mathbf{r}) + \int d\mathbf{r}' \frac{\rho(\mathbf{r}')}{|\mathbf{r}-\mathbf{r}'|} + \frac{\delta E^{\rm LDA}_{\rm xc}[\rho,\mathbf{m}]}{\delta\rho(\mathbf{r})}, \tag{1.3.31}$$

$$\mathbf{h}_{\rm KS}(\mathbf{r}) = \mathbf{h}(\mathbf{r}) + \frac{\delta E^{\rm LDA}_{\rm xc}[\rho,\mathbf{m}]}{\delta\mathbf{m}(\mathbf{r})}. \tag{1.3.32}$$

Extremizing with respect to $G^{\sigma\sigma'}_{ab}$ yields the equation for self energy

$$\Sigma^{\sigma\sigma'}_{ab}(i\omega) = \frac{\delta\Phi}{\delta G^{\sigma\sigma'}_{ab}(i\omega)} - \frac{\delta\Phi_{DC}}{\delta G^{\sigma\sigma'}_{ab}(i\omega)}. \tag{1.3.33}$$

The physical meaning of the dynamical potential Σ is parallel to the meaning of the original Kohn-Sham potential $V_{\rm KS}$: it is the function that one needs to add to the correlated block of the one-electron Hamiltonian in order to obtain the desired local Green function:

$$G^{\sigma\sigma'}_{ab}(i\omega) = \sum_{\mathbf{k}} [i\omega - \hat{H}^{\mathbf{k}} - \hat{\Sigma}(i\omega)]^{\sigma\sigma' -1}_{ab}, \tag{1.3.34}$$

where $H^{\sigma\sigma'\mathbf{k}}_{ab} = \langle\chi^{\sigma}_{a\mathbf{k}}|(-\nabla^2 + V_{KS})\hat{I} + 2\mu_B\mathbf{s}\cdot\mathbf{h}_{KS} + \xi(\mathbf{r})\mathbf{l}\cdot\mathbf{s}|\chi^{\sigma'}_{b\mathbf{k}}\rangle$ is the one-electron Hamiltonian in $\mathbf{k}$-space. It is the frequency dependence of the dynamical potential which allows us to treat Hubbard bands and quasiparticle bands on the same footing.

In general, an explicit form of $\Phi[G]$ is not available. DMFT maps the DMFT+LDA function to an Anderson impurity model. Self–consistency equations obtained in this way are used to find the self energy (1.3.33). To introduce LDA+U method we confine ourselves to zero temperature and make an additional assumption on solving the impurity model using the Hartree–Fock approximation. In this limit an explicit form of $\Phi[G]$ is available and DMFT self–consistency loop is unnecessary. We first determine the Coulomb interaction by considering a Hartree–Fock averaging of the original expression for the Coulomb interaction

given by

$$\frac{1}{2}\sum_{\sigma\sigma'}\sum_{abcd}\langle a\sigma b\sigma'|\frac{e^2}{r}|c\sigma d\sigma'\rangle c_a^{\sigma+}c_b^{\sigma'+}c_d^{\sigma'}c_c^{\sigma}. \tag{1.3.35}$$

In this limit, the sum of local graphs reduce to

$$\begin{aligned}\Phi[\hat{G}] &= \frac{1}{2}\sum_{abcd\sigma}U_{abcd}n_{ab}^{\sigma\sigma}n_{cd}^{-\sigma-\sigma}\\ &+ \frac{1}{2}\sum_{abcd\sigma}(U_{abcd}-J_{abcd})n_{ab}^{\sigma\sigma}n_{cd}^{\sigma\sigma}\\ &- \frac{1}{2}\sum_{abcd\sigma}J_{abcd}n_{ab}^{\sigma-\sigma}n_{cd}^{-\sigma\sigma}.\end{aligned} \tag{1.3.36}$$

Here, the matrices $U_{abcd}=\langle ac|v_C|bd\rangle$ and $J_{abcd}=\langle ac|v_C|db\rangle$ have the following definitions:

$$\begin{aligned}U_{abcd} &= \int \chi_a^{\sigma*}(\mathbf{r})\chi_c^{\sigma*}(\mathbf{r}')v_C(\mathbf{r}-\mathbf{r}')\chi_b^{\sigma}(\mathbf{r})\chi_d^{\sigma}(\mathbf{r}')d\mathbf{r}d\mathbf{r}',\\ J_{abcd} &= \int \chi_a(\mathbf{r})^{\sigma*}\chi_c^{\sigma*}(\mathbf{r}')v_C(\mathbf{r}-\mathbf{r}')\chi_d^{\sigma}(\mathbf{r})\chi_b^{\sigma}(\mathbf{r}')d\mathbf{r}d\mathbf{r}',\end{aligned}$$

where the Coulomb interaction $v_C(\mathbf{r}-\mathbf{r}')$ has to take into account the effects of screening by conduction electrons. Note that the matrices U_{abcd} and J_{abcd} are spin independent since the Coulomb interaction is independent of spin. The occupancy matrix $n_{ab}^{\sigma\sigma'}$ is a derived quantity of the Green function:

$$n_{ab}^{\sigma\sigma'}=T\sum_{\omega}G_{ab}^{\sigma\sigma'}(i\omega)e^{i\omega 0^+}. \tag{1.3.37}$$

Notice that when spin–orbit coupling is taken into account, the occupancy matrix becomes non–diagonal with respect to spin index even though the interaction matrices U_{abcd} and J_{abcd} are spin independent.

The self-energy $\Sigma_{ab}^{\sigma\sigma'}$ now takes the from for spin diagonal elements

$$\begin{aligned}\Sigma_{ab}^{\sigma\sigma} &= \sum_{cd}U_{abcd}n_{cd}^{-\sigma-\sigma}+\sum_{cd}(U_{abcd}-J_{abcd})n_{cd}^{\sigma\sigma}\\ &- \frac{\delta\Phi_{DC}}{\delta G_{ab}^{\sigma\sigma}(i\omega)},\end{aligned} \tag{1.3.38}$$

and for spin off–diagonal elements it is given by

$$\Sigma_{ab}^{\sigma-\sigma}=-\sum_{cd}J_{abcd}n_{cd}^{-\sigma\sigma}-\frac{\delta\Phi_{DC}}{\delta G_{ab}^{\sigma-\sigma}(i\omega)}. \tag{1.3.39}$$

The off–diagonal elements of the self energy are only present when spin–orbit coupling is included, hence it is a relativistic effect. To make it more physically transparent we can introduce magnetic moments at the given shell by

$$m^{\mu}_{ab} = \sum_{\sigma\sigma'} s^{\mu}_{\sigma\sigma'} n^{\sigma\sigma'}_{ab} \tag{1.3.40}$$

where μ runs over x, y, z for Cartesian coordinates, or over,$-1, 0, +1$ $(z, \pm)$ for spherical coordinates. Relativistic correction from strong correlations can be written in physically transparent form

$$\begin{aligned} \frac{1}{2}\sum_{abcd\sigma} J_{abcd} n^{\sigma-\sigma}_{ab} n^{-\sigma\sigma}_{cd} &\equiv \frac{1}{2}\sum_{abcd} m^{(+)}_{ab} J_{abcd} m^{(-)}_{cd} \\ &+ \frac{1}{2}\sum_{abcd} m^{(-)}_{ab} J_{abcd} m^{(+)}_{cd} \end{aligned} \tag{1.3.41}$$

and in principle has room for further generalization of exchange matrix J_{abcd} to be anisotropic, i.e depend on $\mu\mu'$: $J^{\mu\mu'}_{abcd}$.

Part of the energy added by $\Phi[\hat{G}]$ is already included in LDA functional. The double counting term Φ_{dc} is added to subtract this already included part of $\Phi[\hat{G}]$. It was proposed [43] that the form for $\Phi[\hat{G}]$ is

$$\Phi^{Model}_{dc} = \frac{1}{2}\bar{U}\bar{n}(\bar{n}-1) - \frac{1}{2}\bar{J}[\bar{n}^{\uparrow}(\bar{n}^{\uparrow}-1) + \bar{n}^{\downarrow}(\bar{n}^{\downarrow}-1)], \tag{1.3.42}$$

where

$$\bar{U} = \frac{1}{(2l+1)^2}\sum_{ab}\langle ab|\frac{1}{r}|ab\rangle, \tag{1.3.43}$$

$$\bar{J} = \bar{U} - \frac{1}{2l(2l+1)}\sum_{ab}(\langle ab|\frac{1}{r}|ab\rangle - \langle ab|\frac{1}{r}|ba\rangle), \tag{1.3.44}$$

and $\bar{n}^{\sigma} = \sum_a n^{\sigma}_{aa}$, and $\bar{n} = \bar{n}^{\uparrow} + \bar{n}^{\downarrow}$. The subtraction by 1 is made to take the self-interaction into account. This generates the self energy in the form:

$$\begin{aligned} \Sigma^{\sigma\sigma}_{ab} &= \sum_{cd} U_{abcd} n^{-\sigma-\sigma}_{cd} + \sum_{cd}(U_{abcd} - J_{abcd}) n^{\sigma\sigma}_{cd} \\ &- \delta_{ab}\bar{U}(\bar{n} - \frac{1}{2}) + \delta_{ab}\bar{J}(\bar{n}^{\sigma} - \frac{1}{2}) \end{aligned} \tag{1.3.45}$$

$$\Sigma^{\sigma-\sigma}_{ab} = -\sum_{cd} J_{abcd} n^{-\sigma\sigma}_{cd}. \tag{1.3.46}$$

As an example, when only the effect of U is under investigation, the U and J matrices are $U_{abcd} = \delta_{ab}\delta_{cd}U$, $J_{abcd} = \delta_{ad}\delta_{cb}U$, $\bar{U} = U$, and $\bar{J} = 0$. This simple U and J matrices make it possible to write down corrections to LDA functional and LDA Kohn-Sham potential:

$$\Phi[\hat{G}] - \Phi_{\rm dc}^{\rm Model} = -\frac{1}{2}\sum_{\sigma}\sum_{ab} U(n_{ab}^{\sigma\sigma}n_{ba}^{\sigma\sigma} + n_{ab}^{\sigma-\sigma}n_{ba}^{-\sigma\sigma}) - \frac{1}{2}U\bar{n} \quad (1.3.47)$$

$$\Sigma_{ab}^{\sigma\sigma} = U(\frac{1}{2}\delta_{ab} - n_{ba}^{\sigma\sigma}) \quad (1.3.48)$$

$$\Sigma_{ab}^{\sigma-\sigma} = Un_{ba}^{-\sigma\sigma} \quad (1.3.49)$$

The DMFT self consistency equation identifies the Green function of the original model and the Green function of the mapped impurity model to find the self energy. Now that we can express the sum of local graphs $\Phi[\hat{G}]$ in terms of the original Green function, the DMFT loop need not to be performed. The problem is now reduced to extremizing the functional [Eq. (1.3.29)] with the expression for the sum of local graphs [Eq. (1.3.36)], which is exactly the LDA+U method [44].

The DMFT functional and its static correspondent LDA+U functional are defined once a set of projectors $\{\chi_a^{\sigma}(\mathbf{r})\}$ and a matrix of interactions U_{abcd} and J_{abcd} are prescribed. When l orbitals are used as the projection operators, the matrix is expressed in terms of Slater parameters F^k. For $a \equiv lm, b \equiv lk, c \equiv l'm', d \equiv l'k'$ and representing $\chi_a^{\uparrow}(\mathbf{r}) = \phi_{lm}(\mathbf{r})(1,0)^{\rm T}$, where $\phi_{lm}(\mathbf{r}) = \phi_l(r)i^lY_{lm}(\hat{r})$, we can express the matrices U_{abcd} and J_{abcd} in the following manner:

$$\begin{aligned}\langle lml'm'|\frac{1}{r}|lkl'k'\rangle &= \sum_{l''=0,2,\ldots}^{\min(2l,2l')} \frac{4\pi}{2l''+1}F_{ll'}^{(u)l''} \quad (1.3.50)\\ &\times (-1)^{m''}C_{lklm}^{l''m''=m-k}C_{l'm'l'k'}^{l''m''=k'-m'}\\ \langle lml'm'|\frac{1}{r}|l'k'lk\rangle &= \sum_{l''=0,2,\ldots}^{\min(2l,2l')} \frac{4\pi}{2l''+1}F_{ll'}^{(j)l''} \quad (1.3.51)\\ &\times (-1)^{m''}C_{l'k'lm}^{l''m''=m-k'}C_{l'm'lk}^{l''m''=k-m'}\end{aligned}$$

where the quantities $C_{LL'}^{L''}$ are the Gaunt coefficients which are the integrals of the

products of three spherical harmonics

$$C_{LL'}^{L''} = \int Y_L(\hat{\mathbf{r}}) Y_{L'}^*(\hat{\mathbf{r}}) Y_{L''}(\hat{\mathbf{r}}) d\hat{\mathbf{r}}. \tag{1.3.52}$$

The quantities $F^{(u)}$ and $F^{(j)}$ are given by the following radial integrals

$$F_{ll'}^{(u)l''} = \int \frac{r^{l''}}{r^{l''+1}} \phi_l^2(r) \phi_{l'}^2(r') dr dr' \tag{1.3.53}$$

$$F_{ll'}^{(j)l''} = \int \frac{r^{l''}}{r^{l''+1}} \phi_l(r) \phi_{l'}(r) \phi_l(r') \phi_{l'}(r') dr dr'. \tag{1.3.54}$$

When $l \equiv l'$, the quantities $F^{(u)}$ and $F^{(j)}$ are equal and have a name of Slater integrals which for s–electrons are reduced to one constant $F^{(0)}$, for p–electrons there are two constants: $F^{(0)}$, $F^{(2)}$, for d's: $F^{(0)}$, $F^{(2)}$, $F^{(4)}$, etc. In this case, the expressions for U and J are reduced to

$$\langle m, m'' | v_C | m', m''' \rangle = \sum_k a_k(m, m', m'', m''') F^k, \tag{1.3.55}$$

where $0 \leq k \leq 2l$, and

$$a_k(m, m', m'', m''') = \frac{4\pi}{2k+1} (-1)^q C_{lmlm'}^{kq=m-m'} C_{lm''lm'''}^{kq=m'''-m''}. \tag{1.3.56}$$

Slater integrals can be linked to Coulomb and Stoner parameters U and J obtained from LSDA supercell procedures via $U = F^0$ and $J = (F^2 + F^4)/14$. The ratio F^2/F^4 is to good accuracy a constant ~ 0.625 for d electrons. For f electrons, the corresponding expression is $U = F^0$ and $J = (286F^2 + 195F^4 + 250F^6)/6435$.

To summarize, we have shown the equivalence of Hartree–Fock approximation of DMFT and LDA+U method. LDA+U is the method proposed to overcome the difficulties of LDA when strong correlations are present [45]. Since the density uniquely defines the Kohn–Sham orbitals, and they in turn, determine the occupancy matrix of the correlated orbitals, once a choice of correlated orbitals is made, we still have a functional of the density alone. However it is useful to proceed with Eq. (1.3.29), and think of the LDA+U functional as a functional of ρ,

V_{KS}, $\mathbf{m}$, $\mathbf{h}_{\mathrm{KS}}$, $G_{ab}^{\sigma\sigma'}$, and $\Sigma_{ab}^{\sigma\sigma'}$, whose minimum gives better approximations to the ground–state energy in strongly correlated situations. Allowing the functional to depend on the projection of the Kohn–Sham energies onto a given orbital, allows the possibility of orbitally ordered states. This is a major advance over LDA in situations where this orbital order is present. As recognized many years ago, this is a very efficient way of gaining energy in correlated situations, and is realized in a wide variety of systems.

1.4 Conclusion

We used effective action formalism to describe density-functional based methods, used in the later chapters. In particular, we presented LDA and LDA+DMFT methods, and introduce LDA+U as Hartree–Fock approximation of LDA+DMFT.

Chapter 2
Half-metallic Ferromagnet CrO_2

In this chapter, the problem of the importance of strong correlations for the electronic structure, transport and magnetic properties of half–metallic ferromagnetic CrO_2 is addressed by performing density functional electronic structure calculations in the local spin density approximation (LSDA) as well as using the LSDA+U method. It is shown that the corresponding low–temperature experimental data are best fitted without accounting for the Hubbard U corrections. We conclude that the ordered phase of CrO_2 is weakly correlated.

2.1 Introduction and motivation

Chromium dioxide is an unusual member of wide class of $3d$ metal oxides. CrO_2 is a half metallic ferromagnet, which means that it is a conductor in one spin channel and a semiconductor in the other. The highest measured spin-polarization of all materials [46], [47] together with a Curie temperature $393^{\circ}K$ allows one to consider CrO_2 as a good candidate for spinotronic and magnetoelectronic devices [34]. These and other multiple industrial applications as well as fundamental interest in its half-metallic electronic structure led to intensive theoretical [2, 48, 3, 4, 49, 50, 30] and experimental [6, 51, 52, 5, 53, 54] studies of chromium dioxide in recent years.

The main discussion was centered around the role of strong correlations for the description of CrO_2 ferromagnetic phase. Since Cr in its formal 4+ valence state has two $3d$ electrons of t_{2g} symmetry, one would expect manifestation of

correlation effects of the Mott–Hubbard nature. On the other hand, the metallic behavior of the spin majority band suggests that Coulomb interactions of the Hubbard type can be screened out [3]. The comparison with the available photoemission and optical conductivity data did not clarify the situation. One–electron spectra calculated using the LSDA+U method [55, 44] fit the photoemission and inverse photoemission experiments well with the choice of intra–atomic Coulomb and exchange parameters $U = 3$ eV and $J = 0.87$ eV [3, 6]. This indicates the importance of strong correlations. Contrary to this result, the LSDA optical conductivity calculations explain experimental data [4], suggesting the regime of weak coupling.

In this chapter we address the controversial role of strong correlations in ferromagnetic CrO_2 by presenting combined studies of its electronic structure, optical conductivity, and magnetic anisotropy using the LSDA and LSDA+U schemes. We employ a linear–muffin–tin–orbital (LMTO) method in its atomic sphere approximation (ASA) [40, 56] (also will be discussed in Section 4.2.2) for our electronic structure calculations. The chapter is organized as follows. In Section 2.2 the crystalline structure of CrO_2 is described. The rutile structure of this material causes additional technical difficulties in computations. Two subsections are devoted to their solutions. In Section 2.3 the calculated densities of states (DOSes) and band structure are presented and compared with the photoemission spectroscopy (PES) data. Sections 2.4 and 2.5 are devoted to calculations and to comparison with experimental data of optical conductivity and magnetic anisotropy energy respectively. Finally, we conclude in Section 2.6.

2.2 Rutile Structure

2.2.1 Description of unit cell of CrO_2

CrO_2 is a challenging material for *ab Initio* calculations due to its open rutile structure with space group $D_{4h}^{14}(P4_2/mnm)$. The unit cell contains two CrO_2 formula units. The Bravais lattice is tetragonal with $c/a = 0.65958$ and a constant lattice a =0.4421 nm [57]. The Cr atoms, surrounded by a slightly distorted octahedras of oxygen atoms, form a body-centered tetragonal lattice. The octahedra surrounding Cr at the center and corner positions differ by a 90° rotation about z-axis (see Figure 2.1).

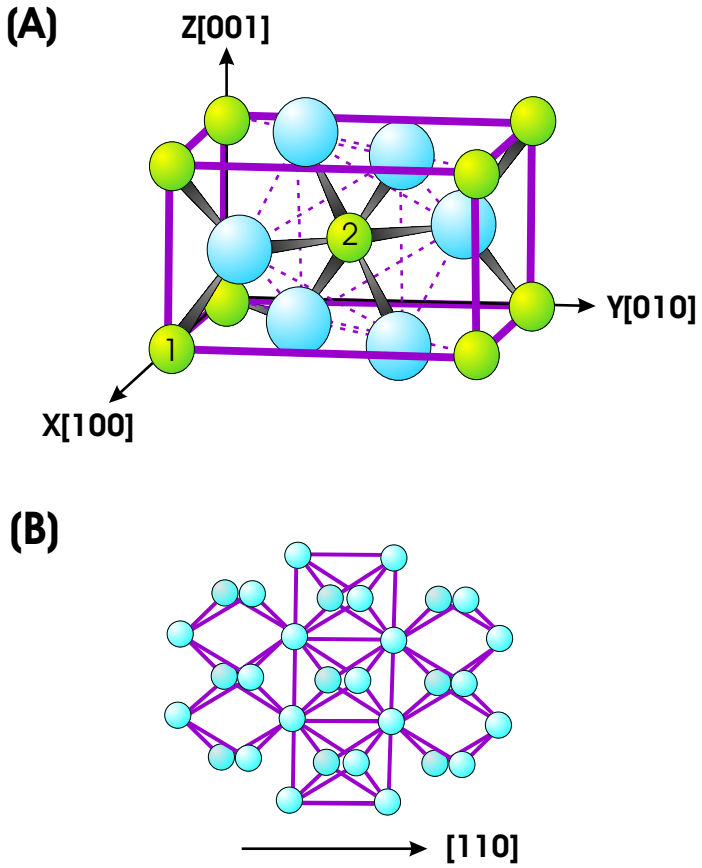

Figure 2.1: Primitive unit cell for CrO_2 in the rutile structure. (A) larger spheres represent the O atoms and smaller Cr. Two Cr atoms with non-equivalent positions are indicated by numbers 1 (at position (0,0,0)) and 2 (at position (1/2,1/2,1/2)). In (B) the connectivity of the oxygen octahedra projected on the [110] plane is demonstrated.

Table 2.1: High-symmetry sites of the rutile structure [1] ($\bar{x} \equiv 1 - x$).

Atom	Wyckoff notation	coordinates			
Cr	2 a m.mm	$0,0,0$	$\frac{1}{2},\frac{1}{2},\frac{1}{2}$		
O	4 f m.2m	$x,x,0$	$\bar{x},\bar{x},0$	$\bar{x}+\frac{1}{2},x+\frac{1}{2},\frac{1}{2}$	$x+\frac{1}{2},\bar{x}+\frac{1}{2},\frac{1}{2}$
E_1	4 c 2/m	$0,\frac{1}{2},0$	$0,\frac{1}{2},\frac{1}{2}$	$\frac{1}{2},0,\frac{1}{2}$	$\frac{1}{2},0,0$
E_2	4 g m.2m	$x,\bar{x},0$	$\bar{x},x,0$	$x+\frac{1}{2},x+\frac{1}{2},\frac{1}{2}$	$\bar{x}+\frac{1}{2},\bar{x}+\frac{1}{2},\frac{1}{2}$

The rutile structure can also be described by considering an array of anions of approximately hexagonal close packed form in which only half of the octahedral holes are occupied by metal atoms. The half occupation of the octahedral, however, leads to a low packing fraction, so that no more than 36% of the unit cell volume can be filled with touching hard spheres. This is caused by the short anion-anion distance between the positions $(x, x, 0)$ and $(1-x, 1-x, 0)$. In order to increase the filling factor of unit cell in ASA calculations we introduce two types of "empty spheres" E_1 and E_2 (for details see Section 2.3.1). All atoms and empty spheres positions are listed in Table 2.1. In the case of CrO_2 the parameter $x = 0.3053$ a.u.

2.2.2 Local basis of Cr atoms

The natural classification of crystalline field for Cr atoms could be performed only in the local basis by taking into account the symmetry of surrounding oxygen octahedra. Thus, the electronic structure of chromium dioxide could be understood and analyzed only in terms of this local coordinates. The surrounding oxygen octahedra leads to new natural local coordinate system for spheres of chromium (see Figure 2.2). Strictly speaking, due to distortion each octahedra has a rectangular rather than a square in the base. Thus, in the Figure 2.2 local axes X and Y point not to the exact locations of O atoms, but slightly off to the outer directions.

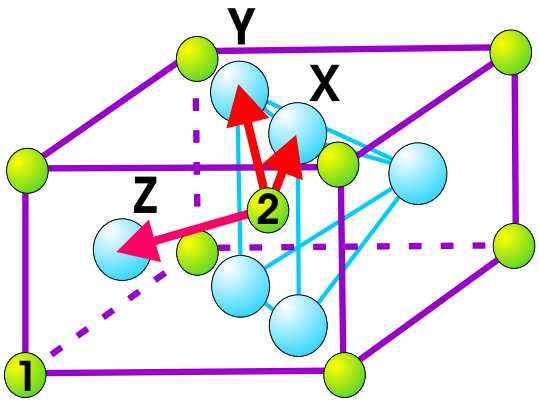

Figure 2.2: Local coordinate system for chromium atom Cr at the position $(1/2, 1/2, 1/2)$, indicated by number 2. Z axis points exactly to the location of O atom, while axes X and Y point to the outer directions slightly off the locations of O atoms.

Each of two Cr atoms in the unit cell has its one local basis. Even though orientation of two neighbor oxygen octahedras differs by 90° in the ab-plane the transformation to the local basis cannot be done for both Cr atoms simultaneously because of noncommutativity of space rotations. Thus, each Cr atom requires its own matrix of rotation to the local basis. For Cr atom at $(0, 0, 0)$ (here and later we refer to this atom as Cr@1) the new local coordinates (primed) are related to Cartesian coordinates of the unit cell as:

$$\begin{pmatrix} x' \\ y' \\ z' \end{pmatrix} = \begin{pmatrix} -1/2 & 1/2 & 1/\sqrt{2} \\ 1/2 & -1/2 & 1/\sqrt{2} \\ 1/\sqrt{2} & 1/\sqrt{2} & 0 \end{pmatrix} \begin{pmatrix} x \\ y \\ z \end{pmatrix} \tag{2.2.1}$$

This matrix has eigenvector $(1, 1, \sqrt{2})$ with corresponding eigenvalue 1. So transformation 2.2.1 is equivalent to the rotation about $(1, 1, \sqrt{2})$ axis for π.

For Cr at $(1/2, 1/2, 1/2)$ (here and later we refer to this atom as Cr@2) the new coordinates are related to the old ones as:

$$\begin{pmatrix} x' \\ y' \\ z' \end{pmatrix} = \begin{pmatrix} 1/2 & -1/2 & 1/\sqrt{2} \\ 1/2 & -1/2 & -1/\sqrt{2} \\ 1/\sqrt{2} & 1/\sqrt{2} & 0 \end{pmatrix} \begin{pmatrix} x \\ y \\ z \end{pmatrix} \tag{2.2.2}$$

This matrix has eigenvector $(\sqrt{2},0,1)$ with corresponding eigenvalue 1. So transformation (2.2.2) is equivalent to the rotation about $(\sqrt{2},0,1)$ axis for $2\pi/3$.

Before the discussion of the structure of Cr $3d$ orbitals in the local basis, we note that cubic harmonics in Cartesian coordinates are defined according to the following formulas[58]:

$$Y_{21}(\vec{r}) = \frac{2yz}{r^2}a, \quad Y_{22}(\vec{r}) = \frac{2zx}{r^2}a, \quad Y_{23}(\vec{r}) = \frac{2xy}{r^2}a, \tag{2.2.3}$$
$$Y_{24}(\vec{r}) = \frac{x^2-y^2}{r^2}a, \quad Y_{25}(\vec{r}) = (\frac{3z^2}{r^2}-1)\frac{a}{\sqrt{3}}$$

where $a = \sqrt{15/\pi}/4$ is a normalization constant and $r^2 = x^2+y^2+z^2$. Here and below we will refer to these orbitals as (yz), (zx), (xy), (x^2-y^2), and $(3z^2-1)$ correspondingly due to their symmetry properties.

In the local basis the cubic component of the octahedral crystal field splits the fivefold degenerate $3d$ orbital into higher energy doubly degenerate e_g level and lower energy triple degenerate t_{2g} level. Distortions of oxygen octahedra further split the t_{2g} states into lower energy $t_{2g}^{\parallel}$ orbital (xy character) and higher energy twofold degenerate $t_{2g}^{\perp}$ orbitals (yz and zx characters) [3]. The t_{2g} and e_g orbitals of the rutile structure in the local basis in terms of cubic harmonics of the unit cell are given in Table 2.2.

Table 2.2: Expressions for $3d$ e_g and t_{2g} orbitals in rutile structure through cubic harmonics.

Type of atom	Cr@1	Cr@2
$(e_g)_1 : (3z'^2-1)$	$3(xy)_1 - \frac{1}{2}(3z^2-1)_1$	$3(xy)_2 - \frac{1}{2}(3z^2-1)_2$
$(e_g)_2 : (x'^2-y'^2)$	$\frac{1}{\sqrt{2}}((yz)_1-(zx)_1)$	$\sqrt{2}((zx)_2-(yz)_2)$
$(t_{2g})_1 : (x'y')$	$\frac{1}{2}(xy)_1 - \frac{1}{4}(3z^2-1)_1$	$\frac{1}{2}(xy)_2 + \frac{1}{4}(3z^2-1)_2$
$(t_{2g})_2 : (y'z')$	$\frac{1}{2}(yz)_1 + \frac{1}{2}(zx)_1 + \frac{1}{2\sqrt{2}}(x^2-y^2)_1$	$-\frac{1}{2}(yz)_1 - \frac{1}{2}(zx)_1 + \frac{1}{2\sqrt{2}}(x^2-y^2)_1$
$(t_{2g})_3 : (z'x')$	$\frac{1}{2}(yz)_1 + \frac{1}{2}(zx)_1 - \frac{1}{2\sqrt{2}}(x^2-y^2)_1$	$\frac{1}{2}(yz)_1 + \frac{1}{2}(zx)_1 + \frac{1}{2\sqrt{2}}(x^2-y^2)_1$

Since the physical interpretation of calculated quantities can be done only in the local basis it is useful to write down corresponding transformations for the

Hamiltonian and overlap matrix. The Hamiltonian H' and overlap matrix O' in the local basis are related to the Hamiltonian H and overlap matrix O in the cartesian basis as:

$$H' = U^{\dagger} H U, \tag{2.2.4}$$

$$O' = U^{\dagger} O U, \tag{2.2.5}$$

where matrix U has block diagonal structure with identity matrices for s and p orbitals and 5×5 matrices J_1 and J_2 for $3d$ orbitals of atoms Cr@1 and Cr@2 correspondingly:

$$U = \begin{pmatrix} I & 0 & 0 & 0 \\ 0 & J_1 & 0 & 0 \\ 0 & 0 & I & 0 \\ 0 & 0 & 0 & J_2 \end{pmatrix}.$$

With the following order of orbitals:

$$\begin{bmatrix} yz \\ zx \\ xy \\ x^2 - y^2 \\ 3z^2 - 1 \end{bmatrix} \Rightarrow \begin{bmatrix} y'z' \\ z'x' \\ x'y' \\ x'^2 - y'^2 \\ 3z'^2 - 1 \end{bmatrix}$$

the J_1 and J_2 matrices are:

$$J_1 = \begin{pmatrix} 1/2 & 1/2 & 0 & \sqrt{2} & 0 \\ 1/2 & 1/2 & 0 & -\sqrt{2} & 0 \\ 0 & 0 & 1/2 & 0 & 3 \\ 1/2\sqrt{2} & -1/2\sqrt{2} & 0 & 0 & 0 \\ 0 & 0 & 1/4 & 0 & -1/2 \end{pmatrix}$$

and

$$J_2 = \begin{pmatrix} -1/2 & 1/2 & 0 & -\sqrt{2} & 0 \\ -1/2 & 1/2 & 0 & \sqrt{2} & 0 \\ 0 & 0 & -1/2 & 0 & 3 \\ 1/2\sqrt{2} & 1/2\sqrt{2} & 0 & 0 & 0 \\ 0 & 0 & -1/4 & 0 & -1/2 \end{pmatrix}.$$

2.3 Electronic structure of CrO_2

2.3.1 Details of calculations

We performed LSDA and LSDA+U calculations within the atomic sphere approximation (ASA) [16]. As was mentioned before in order to increase the filling factor of CrO_2 unit cell we introduce two types of "empty spheres" E_1 and E_2. The necessity of empty spheres was proven by the fact that without them within LSDA calculations ASA predicted CrO_2 to be a metal in both channels in contradiction with the experiment. The strong sensitivity of the calculated total energy on the filling factor of the unit cell forced us to use three different sets of MT-spheres. Set I was generated by LMTART program, set II and III were used in [3] and [2] respectively. The radii of all MT-spheres as well as corresponding filling factor of the unit cell are listed in Table 2.3. For the electronic structure and transport calculations set I of MT-spheres has been used. However, taking into account small values of magnetic anisotropy energy and strong sensitivity of LDA+U approximation to the filling factor of unit cell we used all three MT-spheres sets for MAE calculations.

The basis set adopted in the calculations is consist of $4s$, $4p$, and $3d$ orbitals for Cr atoms, and $2s$, $2p$ orbitals for O atoms.

Table 2.3: Coordinates and Muffin-Tin Radii R_{MT} of the Atomic Spheres for three different sets (x=0.3053 a.u.).

Atom	Cr	O	E_1	E_2	filling
Wyckoff notation	2a	4f	4c	4g	
Coordinates	0 0 0	x x 0	0 1/2 0	x -x 0	
Radii of MT-sp.(au), set I	1.974707	1.615	1.378	1.434	0.59
Radius of MT-sp.(au), set II	2.06	2.06	1.78	1.62	0.88
Radius of MT-sp.(au), set III	2.12381	2.12381	1.9	1.2	0.86

2.3.2 Fat Bands and Density of States

The results of the LSDA band structure calculation for the spin majority and spin minority carries in the vicinity of the Fermi energy are shown in Figures 2.3 and 2.4 correspondingly. The Fermi level crosses the spin majority t_{2g} manifold. The rest of the Cr $3d$ states is formed from four e_g bands and three t_{2g} spin minority bands which are located above the Fermi level. In both spin channels e_g and t_{2g} bands are well separated for all momenta except for the Γ-point. The whole $3d$ complex is strongly hybridized with oxygen $2p$ bands.

In Figure 2.4 one can see that there is a gap of approximately 1.3 eV between the oxygen $2p$ band and the chromium d band in the spin minority channel. This gap leads to 100% spin polarization at E_F and assures the magnetic moment to be precisely equal to 4 μ_B per unit cell. The t_{2g} bands that cross the Fermi level in the spin majority channel mainly consist of the $t_{2g}^{\perp}$ orbitals (see Figure 2.3). Almost non–dispersive narrow band below E_F (shown as lightly shaded, green in color version) is formed by the $t_{2g}^{\parallel}$ orbital. This localized state undergoes large exchange splitting Δ^{ex} making spin minority $t_{2g}^{\parallel}$ orbitals unoccupied (see Figure 2.4).

The main changes which occur in the band structure for non–zero values of

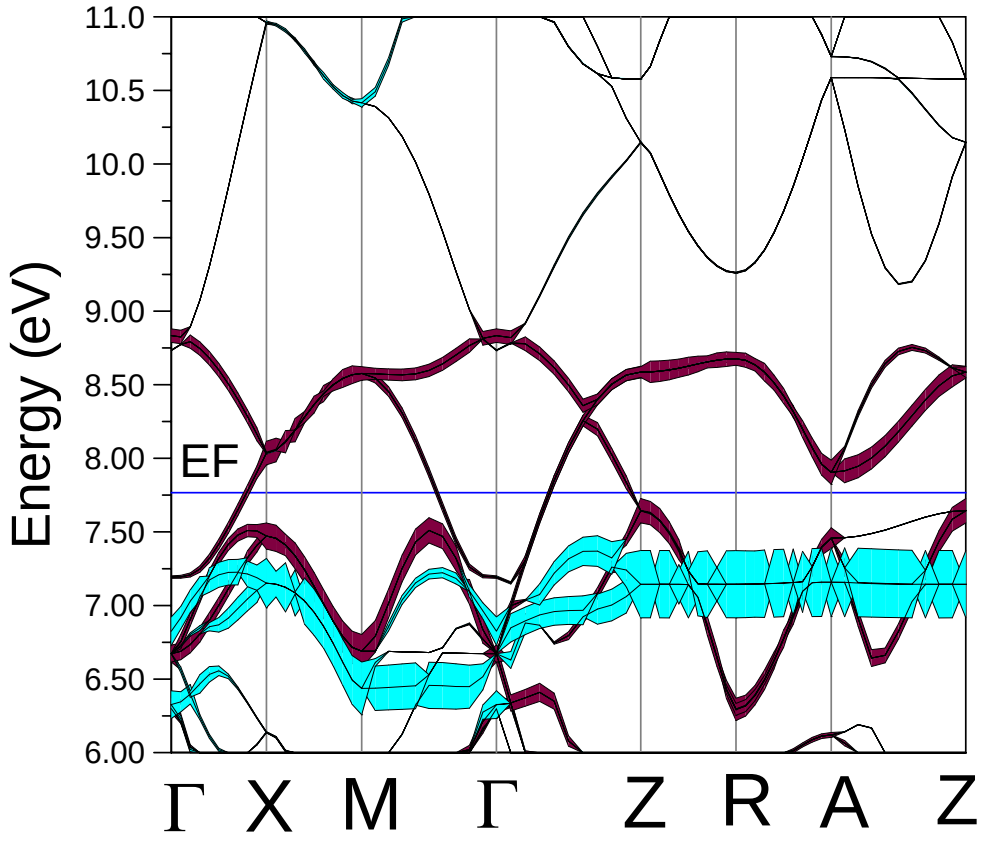

Figure 2.3: LSDA band structure of CrO_2 for spin majority carriers. Dark and light shaded areas (red and green in color version) show the specific weight of $t_{2g}^{\perp}$ and $t_{2g}^{\parallel}$ orbitals respectively in the particular band.

U and J within the LSDA+U method are schematically shown in Figure 2.5. These calculations were performed with $U = 3$ eV and $J = 0.87$ eV. The center of gravity of occupied $t_{2g}^{\parallel}$ band is pushed down by 0.6 eV. The spin minority unoccupied e_g bands are pushed up by 0.6 eV, which opens 0.4 eV gap between $t_{2g}^{\perp}$ and e_g bands above the Fermi level. In the spin minority channel the occupied oxygen bands are shifted up by 0.3 eV. The upper unoccupied t_{2g} and e_g bands are shifted up by 1.1 eV. As a result, the insulating gap is increased and reaches the value of 2.1 eV.

Before we proceed we would like to compare our results with earlier reported

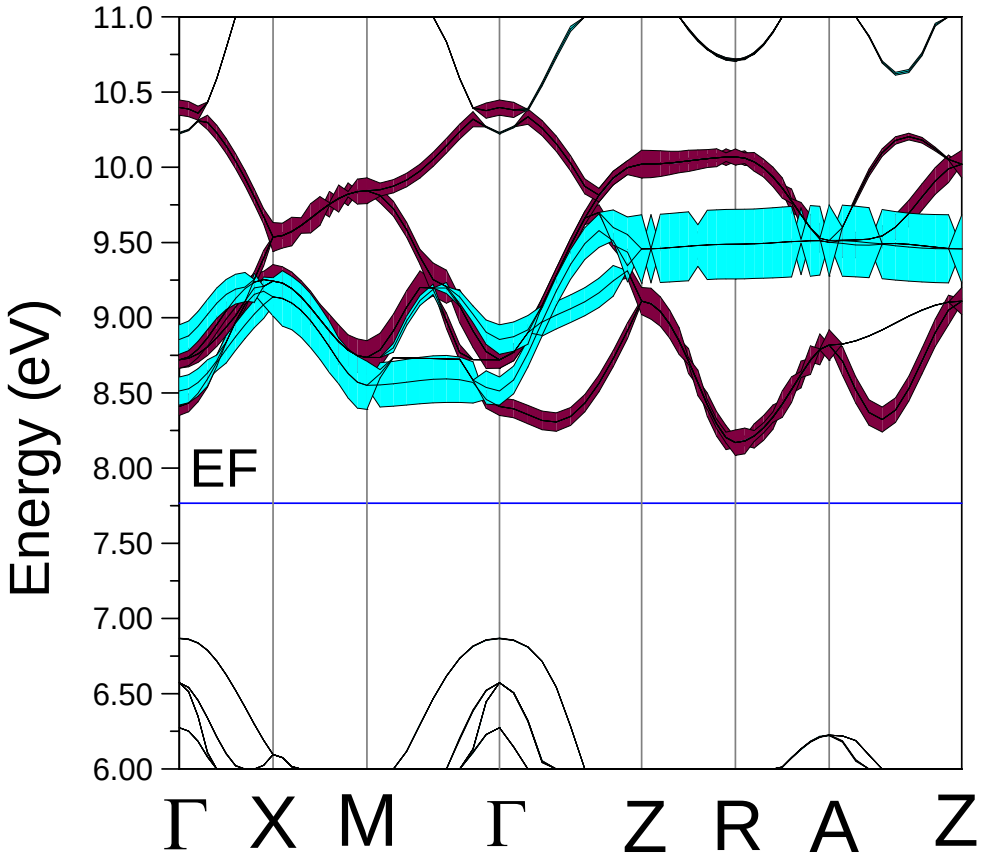

Figure 2.4: LSDA band structure of CrO_2 for spin minority carriers. Dark and light shaded areas (red and green in color version) show the specific weight of $t_{2g}^{\perp}$ and $t_{2g}^{\parallel}$ orbitals respectively in the particular band.

calculations. Table I summarizes values of spin minority energy gap Δ and exchange splitting Δ_{ex}, reported in literature as well as the ones obtained by us. We would like to emphasize that our results obtained using ASA are in the excellent agreement with full potential calculations performed by I. I. Mazin and coworkers [4].

Now we compare calculated electronic structure using the LSDA and the LSDA+U methods with the available experimental data. Figure 2.6 shows comparison of ultraviolet photoemission spectroscopy (UPS) experiments [6] (photon energy $h\nu = 40.8$ eV) with the theoretical spectra which are calculated densities

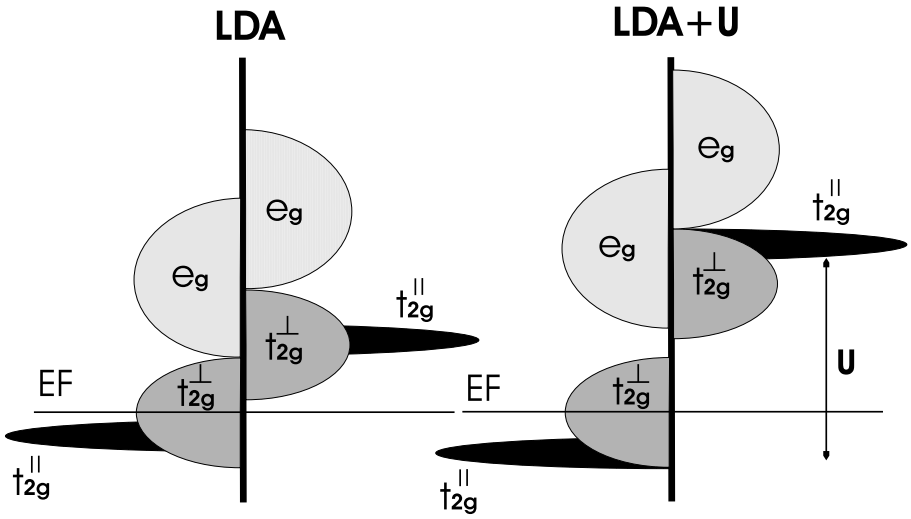

Figure 2.5: Schematic density of states (DOS) of CrO_2 deduced from the LSDA and LSDA+U calculations. Shaded semicircles from right and left represent the bands for spin majority and spin minority carriers.

Energy gap and exchange splitting (in eV).

	LSDA[a]	LSDA+U[a]	LSDA[b]	LSDA+U[c]	GGA[d]	GGA[g]
Δ	1.3	2.1	1.5	2.0	1.3	1.8
Δ_{ex}	2.3	4.6	1.8	4.5	2.5	2.9

Table 2.4: Here [a] our calculations, [b] as reported by Schwartz [2], [c] as reported by Korotin et al. [3] , [d] as reported by I.I. Mazin et al. [4], [g] as reported by Kunes et al. [5]. Values of Δ and Δ_{ex} in b-g are approximate and extracted from the DOS reported in these papers.

of states smeared by both Gaussian and Lorentzian broadening functions. The Gaussian broadening takes into account experimental resolution while Lorentzian takes into account finite lifetime effects. The Gaussian broadening parameter is taken to be 0.4 eV. The full width at half maximum (FWHM) of the Lorentzian was taken to be energy dependent and equal to $0.2|E - E_F|$ eV. We can distinguish two main features in the UPS spectra: (i) a small hump in around -1.5 eV which arises from the t_{2g} band of Cr, and (ii) a big hump around -6.0 eV which comes from the broad $2p$ oxygen band. Both features are fairly well described by

both the LSDA and the LSDA+U calculation. The small discrepancy between the LSDA calculation and experiment could be referred to the fact that at small photon energies photoemission is a more surface sensitive technique. Indeed, recent PES studies of Vanadium oxides [59] have been found to yield spectra not characteristic of the bulk, but rather of surface atoms whose lower coordination number can render more strongly correlated surface layer.

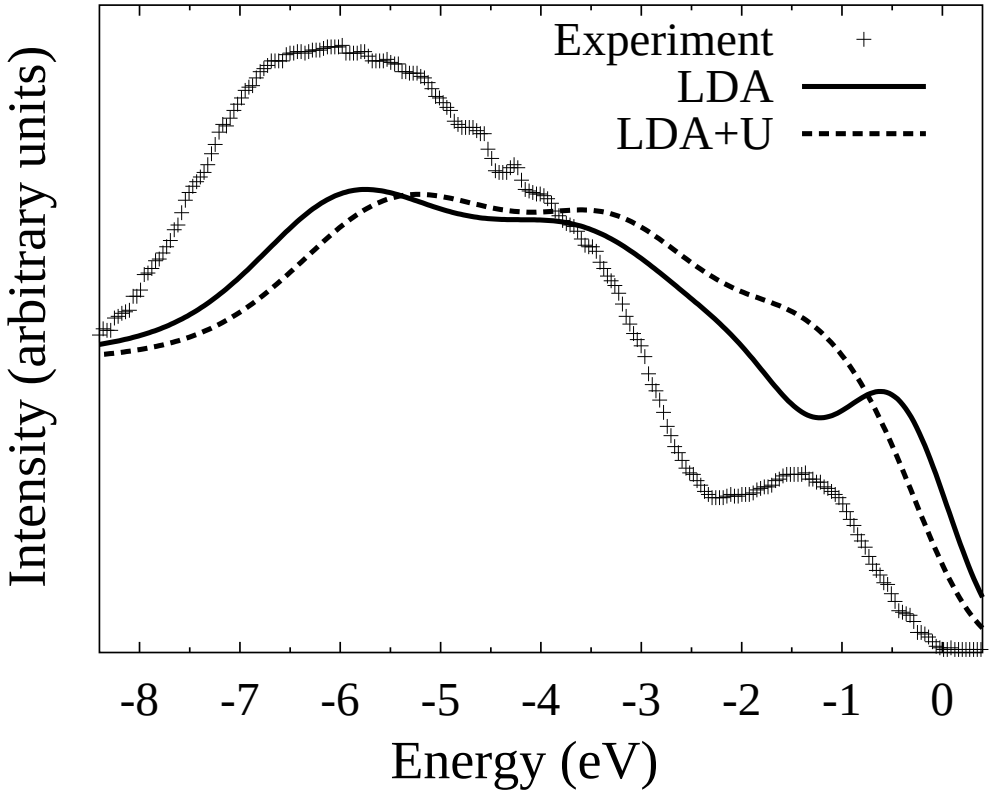

Figure 2.6: Comparison between theoretical densities of states and experimental [6] UPS spectra for CrO_2. The theoretical DOS were smeared out by Gaussian and Lorentzian broadening functions to account for experimental resolution and lifetime effects. The secondary electron background has been taken into account.

For the unoccupied states we have chosen to compare our results with the available x–ray absorption spectra (XAS) [7] rather than with the inverse photoemission as it had been done before [6]. The main reason for this is that XAS is a bulk (not surface) sensitive method. The $2p$ Cr XAS spectrum [7] is compared to our theoretical calculations in Figure 2.7. To deduce theoretical spectra we

performed both Gaussian and Lorentzian broadening of $3d$ and $4s$ partial DOSes. Two first peaks around 0.5 eV and around 1.5 eV come from the unoccupied $3d$ orbitals of chromium. The main contribution to the second peak comes from the t_{2g} orbitals in the spin minority channel. Thus, the LSDA+U overestimates the spin minority gap by a factor of two.

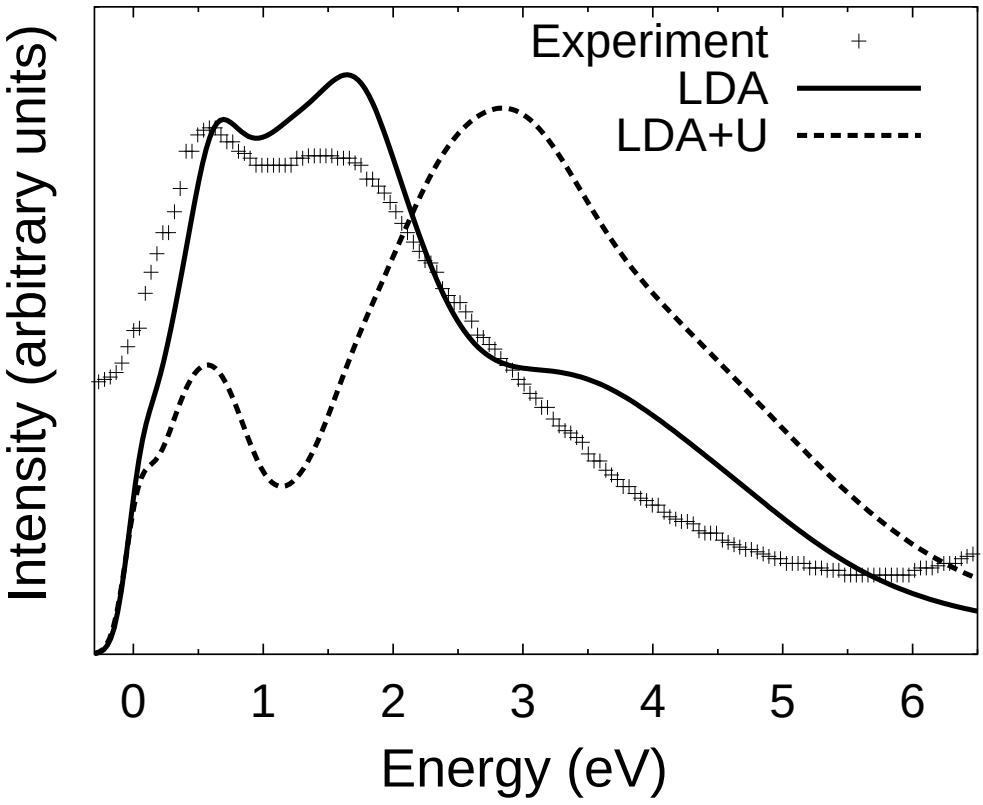

Figure 2.7: Comparison between theory and experiment[7] for Cr 2p x-ray absorption (XAS) spectrum. To deduce theoretical curve from the partial Cr 3d DOS we used 0.1 eV for Gaussian FWHM. The Lorentzian FWHM was taken to be energy dependent and equal to $0.2|E - E_F|$. The binding energy of core $2p_{3/2}$ Cr state 577 eV has been subtracted from the experimental spectrum.

2.4 Optical conductivity

Below we discuss the optical conductivity of CrO_2. In Figure 2.8 diagonal x-components of the optical conductivity calculated using the LSDA and LSDA+U

methods are compared with the experimental results reported by Basov and coworkers [8] (x coordinate refers to the basis of unit cell).

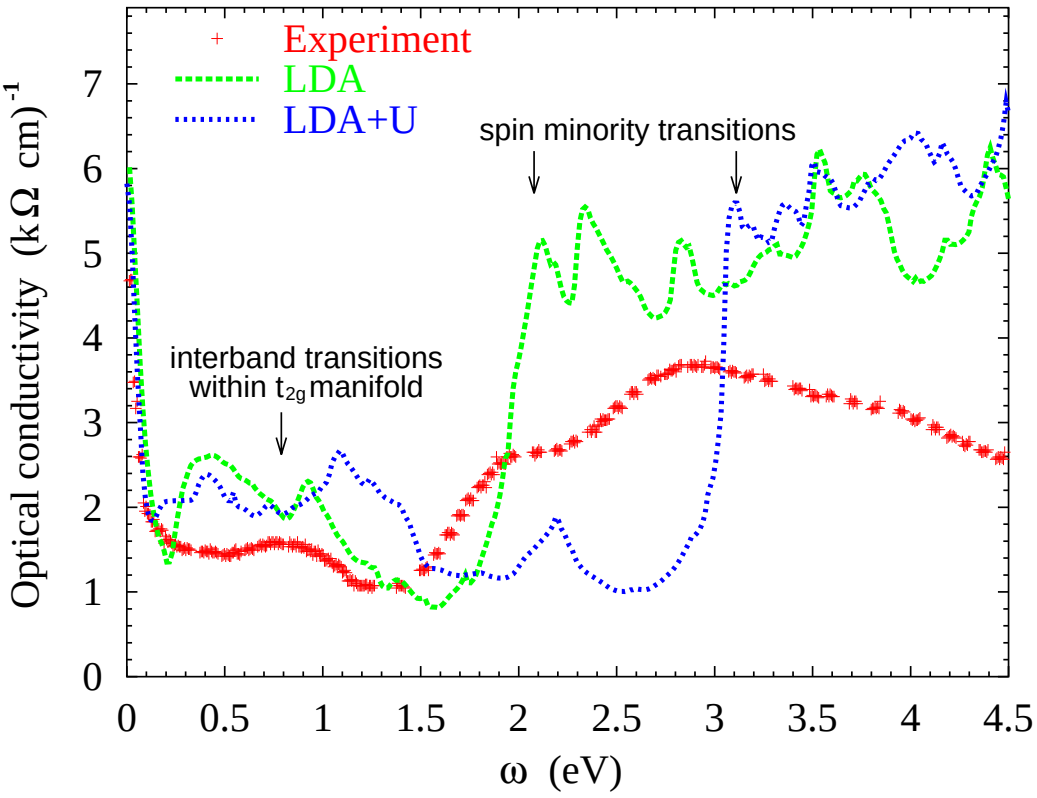

Figure 2.8: Comparison of the optical conductivity of CrO_2 obtained using the LSDA and LSDA+U methods against the experimental data [8].

The main two features of the calculated optical conductivity are a shoulder around $2-3$ eV and a broad hump located at energies $0.2-1.5$ eV. In both LSDA and LSDA+U schemes the shoulder can be identified with two types of transitions. First contribution arises from the minority spin gap transitions and the second one comes from transitions between the occupied $t_{2g}^{\|}$ and unoccupied e_g bands. The hump is formed by interband transitions within the t_{2g}-manifold and the oxygen $2p$ bands near the Fermi level in the spin majority channel. The LSDA prediction is much closer to the experimental curve than the LSDA+U one. The LSDA+U calculations overestimate the minority gap, and hence, the spin

minority transitions occur at higher energies. Our conclusion completely agrees with conclusions of earlier published studies by I. I. Mazin and coworkers [4], as well as by J. Kuneš and coworkers [60].

2.5 Magnetic Anisotropy Energy

Results of calculated magnetic anisotropy energy (MAE) for CrO_2 are presented below. We remind that magnetic anisotropy is the dependence of the internal energy on the direction of spontaneous magnetization. The magnetic anisotropy is a relativistic phenomenon arising due to spin–orbit coupling, where the spin degrees of freedom interact with the spatial anisotropy through the coupling to the orbital degrees of freedom. The experimental measurement of MAE for CrO_2 were hindered by the fact that chromium dioxide is a metastable compound, which irreversibly decomposes at about 200°C [61]. The most recent reliable measurements were performed on epitaxial CrO_2 layers [62, 63, 64]. For thicker films (0.7 - 1.2μm) the in–plane magnetic anisotropy was observed with [001] and [010] easy and hard axis directions respectively. The value of magnetocrystalline anisotropy constant K_1 reported by different groups are 6.7μeV [62], 9.6μeV [63] and 15.6μeV per cell [64]. These values are bigger than typical values of MAE for metals (e.g. for Ni and Fe they are 2.8 and 1.4 μeV per atom correspondingly [65]). This may be due to the fact that such metals as Fe and Ni have cubic crystal structure where MAE identically vanishes in the second order and arises as fourth order effect in the spin-orbit coupling [65]. The low crystal symmetry of CrO_2 provides MAE to appear already in the second order of the perturbation theory, leading to the bigger value of MAE than typical metal values.

Within our LSDA calculation the direction [001] was found to be the easy magnetization axis, which is consistent with latest thin film experiments [62, 63, 64]. To calculate the magnetic anisotropy energies (MAEs) we subtract the total

energy for easy magnetization axis from the total energies with different directions of magnetization ([010], [111] and [102]). For the momentum space integration in the total energy calculations, we follow the analysis given by Trygg and co–workers [66] and use the special point method [67] with a Gaussian broadening [68] of 15 mRy. The validity and convergence of this procedure has been tested in their work [66]. We used about 1000 **k**–points in the irreducible Brillouin zone, while the convergence of MAE is tested up to 8000 **k**–points for all three sets of MT-spheres listed in Table 2.3. Numerical values of MAE in LSDA calculation exceed the maximum experimental value by approximately four times [64].

To determine the influence of intra–atomic repulsion U on the magnetic anisotropy, we have performed LSDA+U calculations for different values of U increasing it from 0 to 6 eV ($J = 0.87$ eV was kept constant except for the LSDA $U = 0$ case). The results of these calculations are presented in Figure 2.9. MAE decreases rapidly starting from the LSDA value (which is approximately equal to 68 μeV per cell) and changes its sign around $U \approx 0.9$eV. This leads to switching correct easy magnetization axis [001] to the wrong one, namely [102]. The biggest experimental value of the MAE reported in the literature is 15.6 μeV per cell [64]. The calculated MAE approaches this value around $U = 0.6$ eV. This signals that correlation effects in the d–shell may be important for this compound although they are strongly screened out.

Another question can arise whether DMFT treatment would change the values of MAE or not. From our experience we expect the total energy to be sufficiently robust quantity, almost insensitive to whether we include dynamical correlations or not. Within the DMFT framework the redistribution of the spectral weight near the Fermi level usually occurs, but the total energy seems to remain almost the same.

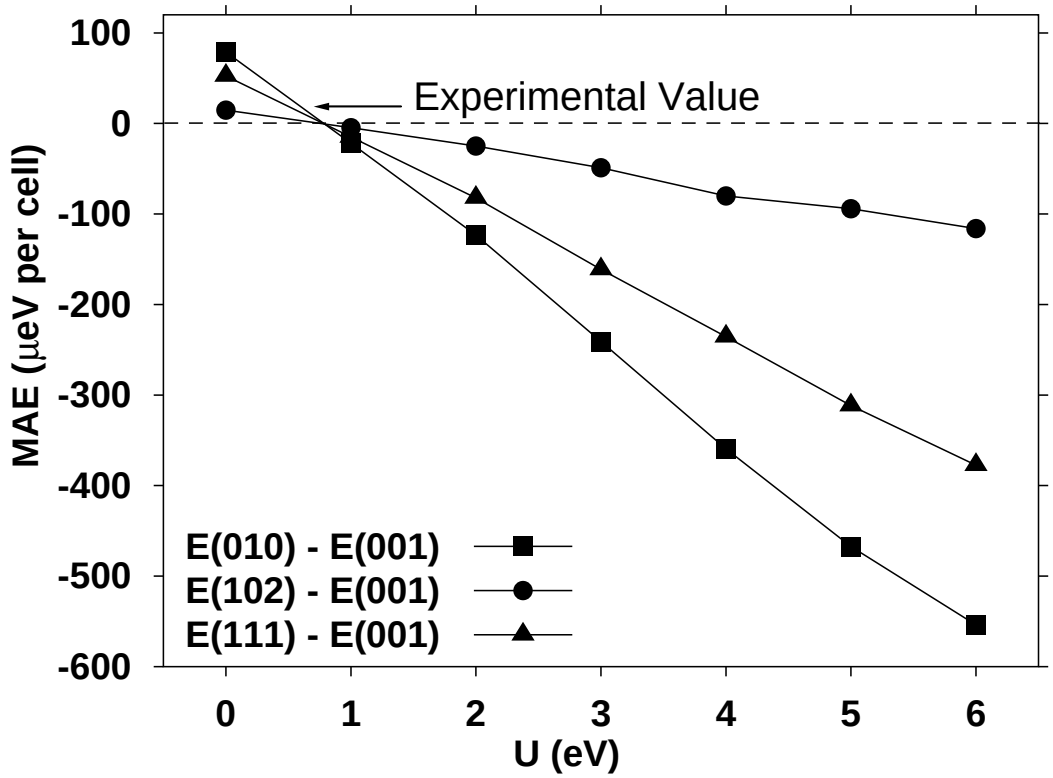

Figure 2.9: The magneto–crystalline anisotropy energies for CrO_2 as functions of U. The experimental value of MAE $E[010] - E[001] = 15.6\mu$eV per cell is shown by arrow.

2.6 Conclusion

To conclude, we have reported the LSDA and LSDA+U calculations of electronic structure, optical conductivity and magnetic anisotropy of CrO_2. Our comparisons with the experimental data point out the local spin density approximation as the proper method to describe this material. We explained the discrepancy between the LSDA and photoemission studies, discussed earlier by other authors [3, 6], by the fact that due to small photon energies used in PES, it is more surface rather than bulk sensitive technique. We resolved this problem by showing that XAS spectrum is unambiguously described by the LSDA calculation. Is has been also shown that even intermediate values of U(of the order of 1-2 eV) lead to the failure of the LSDA+U method to describe the magnetic anisotropy

and the optical conductivity of CrO_2. Since the LSDA+U is not adequate for the description of electronic structure of CrO_2 as well as of its optical and magnetic properties, we conclude that the ordered phase of CrO_2 could be described as weakly correlated material with small values of on-site Coulomb repulsion. It is important to notice that while we have found that the simple one-electron picture describes the ferromagnetic phase of this material well, there is a narrow band formed by the non-dispersive $t_{2g}^{||}$ orbitals (xy character) which in the paramagnetic phase will be single occupied, due to the on-site Coulomb interactions, an effect which cannot be described in LDA and will require a dynamical mean-field treatment for this materials as done in Ref. [49]. The physical basis for the applicability of static mean–field picture in the ferromagnetic phase of this material is due to the large exchange splitting which is able to effectively enforce the single occupancy of the $t_{2g}^{||}$ orbitals.

Chapter 3

DMFT study: CrO_2 on the edge of orbital selective Mott transition

In this chapter we discuss the possible scenarios of orbital selective Mott transition (OSMT) in the case of two-bands Hubbard model on the example of paramagnetic CrO_2. DMFT calculations are performed for the block of t_{2g} orbitals. CrO_2 is shown to be on the edge of a quantum transition, where small energy scales (of the order $\lesssim 0.5$eV) separate phases with completely different physics.

3.1 Introduction and Motivation

We discuss the scenario for metal insulator transition for the case of two bands, considering particular case of chromium dioxide. The electronic structure for ordered phase of this material has been discussed in details in the previous chapter with conclusion that low-energy physics of this compound is ruled by three bands (two of them are degenerate) around Fermi level, formed by t_{2g}-orbitals of Cr atoms. The discussion will be restricted to paramagnetic case only to clarify the nature of Mott transition and all calculations will be performed for temperature $\approx 390K$ ($\beta = 1/16$).

As was discussed earlier, the position of a narrow $t_{2g}^{||}$ band was the source of numerous debates in the literature, particularly for recent DMFT and LDA+DMFT studies [50, 69]. In order to investigate all possible scenarios for the Mott transition we carried out DMFT calculations for several shifted positions of narrow $t_{2g}^{||}$ band. The starting point was LDA paramagnetic partial DOSes shown in

Figure 3.1 with occupancies and bands positions listed in Table 3.1 (the positions are given in half band width of the broad band $(h.b.w.)$,$(h.b.w \approx 1.1632eV)$).

Table 3.1: Partial LDA occupancies and band positions in paramagnetic case.

	$t_{2g}^{\perp}$	$t_{2g}^{\perp}$
$\langle n_\sigma \rangle$	0.267	0.489
ϵ $(h.b.w.)$	-0.038	-0.341

Thus, there is in total approximately one electron per spin per three bands. The narrow $t_{2g}^{||}$ band is almost completely occupied, containing one-half of an electron per each spin. The other one-half of an electron is accommodated by two degenerate half-filled broad $t_{2g}^{\perp}$ bands centered around the Fermi level. The discussion here and below will refer to occupancies of t_{2g} bands per spin.

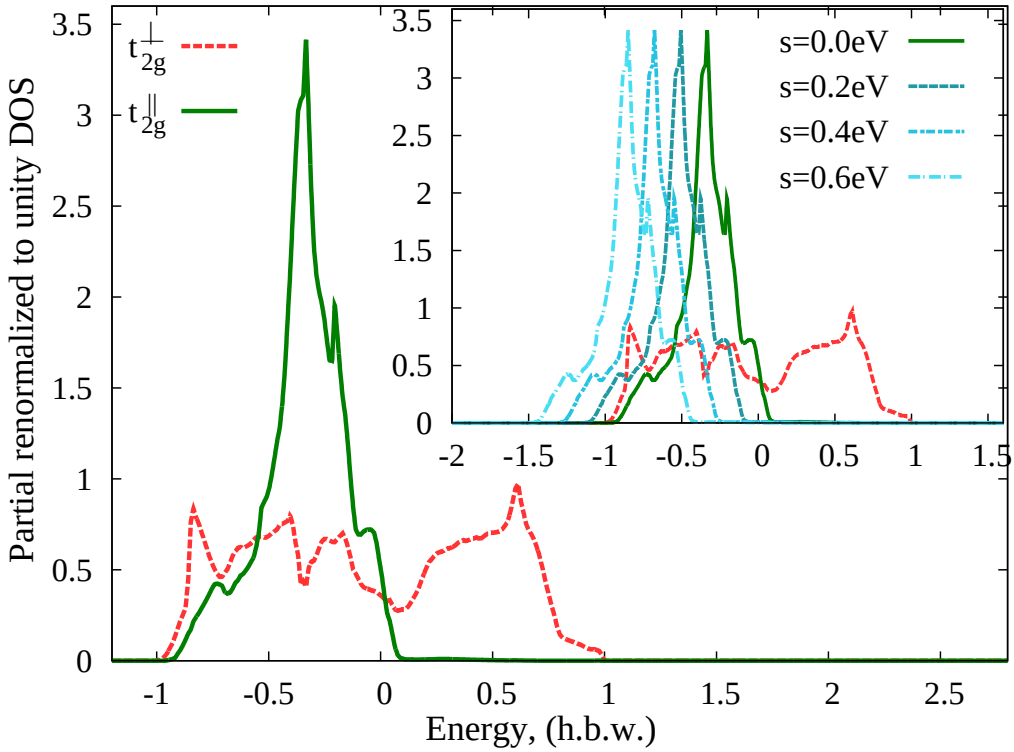

Figure 3.1: The renormalized to unity partial LDA DOSes for t_{2g} bands of Cr were used as input for DMFT calculations. Energy scale h.b.w $\approx 1.1632eV$. Inset: to investigate all possible scenarios of OSMT in CrO_2 the position of narrow band was shifted down in energies by value of parameter s.

Starting with different relative positions of t_{2g} bands: $\epsilon^{||} = \epsilon^{||}_{LDA} - s$ and

$\epsilon^{\perp} = \epsilon^{\perp}_{LDA}$, controlled by parameter s, we investigate evolution of the system under applied Coulomb interaction U and seek for the metal and insulating states for each orbital in (s, U)-parameter space.

3.2 Model Hamiltonian and self-consistent DMFT loop

We consider the symmetric case of multiorbital Hubbard model:

$$H = \sum_{i\alpha\sigma}(\epsilon_\alpha - \mu)d^\dagger_{i\alpha\sigma}d_{i\alpha\sigma} - \sum_{\langle ij\rangle,\alpha\beta\sigma} t^{\alpha\beta}d^\dagger_{i\alpha\sigma}d_{j\beta\sigma} \qquad (3.2.1)$$
$$+\frac{1}{2}\sum_{i\alpha\sigma} U n_{i\alpha\sigma}n_{i\alpha-\sigma} + \frac{1}{2}\sum_{i\alpha\alpha'\sigma}(U' - J)n_{i\alpha\sigma}n_{i\alpha'\sigma},$$

with Coulomb interaction parameters $U' = U$ and $J = 0$. Here $d^\dagger_{i\alpha\sigma}$ ($d_{i\alpha\sigma}$) creates (annihilates) an electron on the site i, in the orbital α, with spin σ. The ϵ_α's are crystal-field levels, and μ is chemical potential. The index α refers to three t_{2g} orbitals: xy (also referred as $t^{||}_{2g}$) and two degenerate yz and zx (also referred as $t^{\perp}_{2g}$).

The self-consistent DMFT loop starts with the solution of the impurity problem stated by Hamiltonian 3.2.1 carried out by quantum Monte Carlo (QMC) method. A seed Weiss function was chosen to be $\mathcal{G}_\alpha(\tau) = \tau - 1 + i(\tau - 1)$ at the first step. The Green's function $G_\alpha(\tau)$ obtained in the QMC routine for orbital α was Fourier transformed to the imaginary frequencies axis and used to calculate self-energies:

$$\Sigma_\alpha(i\omega_n) = \mathcal{G}^{-1}_\alpha(i\omega_n) - G_\alpha(i\omega_n)^{-1}. \qquad (3.2.2)$$

We used the following DMFT self-consistency condition:

$$G^{new}_\alpha(i\omega_n) = \int_{-\infty}^{\infty} d\epsilon\ \frac{D_\alpha(\epsilon)}{i\omega_n + \mu - \Sigma_\alpha(i\omega_n) - \epsilon}, \qquad (3.2.3)$$

where $D_\alpha(\epsilon)$ are partial DOS for orbital α obtained from LDA calculations (see below for detailed description of Input parameters). The new Weiss function is

calculated as

$$[\mathcal{G}_\alpha^{new}(i\omega_n)]^{-1} = [G_\alpha^{new}(i\omega_n)]^{-1} + \Sigma_\alpha(i\omega_n), \tag{3.2.4}$$

Fourier transformed back to the time axis and feed to the QMC solver. This concludes the DMFT loop.

Once consistency is reached the analytical continuation of a new Green's functions $G_\alpha^{new}(i\omega_n)$ to real frequencies was performed using the maximum entropy method.

3.3 Impurity solver: Quantum Monte Carlo

In these calculations we used the QMC solver (version 9.0) implemented by V. S. Oudovenko (for the description of code see online material of [20]). Below we sketch the main ideas behind Hirsch-Fye QMC method for generalized case of n bands (in the present study $n = 3$). The purpose of the QMC impurity solver is to compute the Green's function

$$G_m(\tau) = \langle T d_m(\tau) d^\dagger_{m'}(0)\rangle_S. \tag{3.3.5}$$

Here τ is imaginary time and index m represents pair (α, σ). For our case of three bands:

$$\begin{aligned} &m = 1 \Rightarrow \alpha = yz(t_{2g}^\perp), \sigma = \uparrow; \quad m = 2 \Rightarrow \alpha = yz(t_{2g}^\perp), \sigma = \downarrow; \\ &m = 3 \Rightarrow \alpha = yz(t_{2g}^\perp), \sigma = \uparrow; \quad m = 4 \Rightarrow \alpha = yz(t_{2g}^\perp), \sigma = \downarrow; \\ &m = 5 \Rightarrow \alpha = xy(t_{2g}^{||}), \sigma = \uparrow; \quad m = 6 \Rightarrow \alpha = xy(t_{2g}^{||}), \sigma = \downarrow . \end{aligned} \tag{3.3.6}$$

The average in 3.3.5 is taken with effective action

$$S = -\int\int_0^\beta d\tau d\tau' \sum_m d^\dagger_m(\tau)\mathcal{G}^{-1}_m(\tau - \tau') d_m(\tau') + \int_0^\beta d\tau H_{int}(\tau). \tag{3.3.7}$$

The bath Green's function $\mathcal{G}_m(\tau, \tau')$ is guessed to be $\mathcal{G}_m(\tau) = \tau - 1 + i(\tau - 1)$ at first step and derived from self-consistency condition 3.2.3 at all subsequent

steps. For the purpose of equation derivation we denote Hamiltonian generating $\mathcal{G}_m(\tau)$ by H_0. The interaction term reads

$$H_{int} = \sum_m \sum_{m'>m} U(n_m n_{m'} - \frac{1}{2}(n_m + n_{m'})). \tag{3.3.8}$$

To start the calculation of partition function $Z = Tr\, e^{-\beta(H_0+H_{int})}$ we discretize imaginary time interval $[0, \beta]$ into L slices of length $\Delta\tau$ so that $\tau_l = l\Delta\tau$, $l = 1, 2, \ldots, L$. Then expression for partition function:

$$Z = Tr \prod_{l=1}^{L} e^{-\Delta\tau(H_0+H_{int})} \tag{3.3.9}$$

can be simplified further using the Trotter formula

$$Z \approx Z^{\Delta\tau} = Tr \prod_{l=1}^{L} e^{-\Delta\tau H_0} \prod_{l=1}^{L} e^{-\Delta\tau H_{int}}. \tag{3.3.10}$$

Hirsch-Fye QMC requires Gaussian type of integral for partition function. The Hubbard – Stratonovich transformation is usually used to decouple the interaction term H_{int}:

$$e^{-i\Delta\tau H_{int}} = \frac{1}{2} \sum_{S_{mm'}=\pm 1} \exp\left[\sum_{m<m'} \lambda S_{mm'}(n_m - n_{m'})\right], \tag{3.3.11}$$

with

$$\lambda \equiv arccosh\left[exp\left(\frac{\Delta\tau}{2}U\right)\right]. \tag{3.3.12}$$

The introduced discrete variables $S_{mm'}$ are auxiliary Ising fields at each time slice taking values $S_{mm'} = \pm 1$. The number of auxiliary fields is equal to the number of (m, m')-pairs, i.e. ${}^6C_2 = 15$ in our case. Thus,

$$e^{-\Delta\tau_{l-1}H_{int}} = \frac{1}{2} \sum_{S_{mm'}=\pm 1} \exp\left(\sum_m d_m^\dagger V_m^l(\{S\}) d_m\right) \tag{3.3.13}$$

with diagonal matrix

$$V_m^l(\{S\}) = \lambda \sum_{m'(\neq m)} S_{mm'}(\tau_l)(\theta(m-m') - \theta(m'-m)), \tag{3.3.14}$$

where $\theta(x)$ is step-function.

The final expression for the partition function:

$$Z = Tr_{S_{mm'}(\tau_l)} \prod_m \det O_m[\{S_{mm'}(\tau_l)\}], \tag{3.3.15}$$

where $(2nL) \times (2nL)$ matrix O_m consist of zero elements except:

$$(O_m)_{l,l} = I \tag{3.3.16}$$

$$(O_m)_{l,l-1} = -\exp(-\Delta\tau H_0)\exp(V_m^{l-1})(1 - 2\delta_{l,1}).$$

It can be shown [20] that Green's function G_m can be expressed trough O_m matrix:

$$G_m = O_m^{-1}. \tag{3.3.17}$$

Further, for two different configurations of Ising fields $\{S_{mm'}\}$ and $\{S'_{mm'}\}$ there exist two different matrices V_m and V'_m. The corresponding Green's functions G_m and G'_m are related by (we omit index m for the sake of clarity):

$$G' = G + (G - I)[e^{V'-V} - I]G'. \tag{3.3.18}$$

The last relation can be rewritten as:

$$G' = A^{-1}G, \tag{3.3.19}$$

where

$$A = I + (I - G)[e^{V'-V} - I]. \tag{3.3.20}$$

We note that Dyson equation 3.3.18 also holds for a special case $V_m = 0$ and $G_m = \mathcal{G}_m$.

The Boltzmann factor for different configurations is given by:

$$R = \prod_m R_m, \tag{3.3.21}$$

where

$$R_m = \frac{det(O'_m)}{det(O_m)} = det[I - (G_m - I)[e^{V'_m - V_m} - I]]. \tag{3.3.22}$$

If we make a local change in the field $S_{mm'} \rightarrow S'_{mm'} = S_{mm'}$ for $m < m'$ at time slice l, then the matrix $[\exp(V'_m - V_m) - I]$ has only one non-zero diagonal element at the f-location in the l-th submatrix. Then determinants 3.3.22 are just those non-zero elements and:

$$R = R_m R_{m'}, \tag{3.3.23}$$

$$R_m = 1 - (g_m(l,l) - 1)[e^{-2\lambda S_{mm'}} - 1], \tag{3.3.24}$$

$$R_{m'} = 1 - (g_{m'}(l,l) - 1)[e^{+2\lambda S_{mm'}} - 1], \tag{3.3.25}$$

where g_m is $L \times L$ matrix of f-Greens function. Further we use the heat bath condition to accept or reject flip:

$$R/(1+R) > rand() \quad \Rightarrow \quad flip\ accepted,$$
$$R/(1+R) \leq rand() \quad \Rightarrow \quad flip\ rejected.$$

If the flip is accepted then all time components of the f-Green's function for the new configuration are obtained from the old one through the relation:

$$g'_m(l_1,l_2) = g_m(l_1,l_2) + \sum_l (g_m(l_1,l) - \delta_{l_1,l}) \frac{e^{-2\lambda S_{mm'}}}{R_m} g_m(l,l_2), \tag{3.3.26}$$

$$g'_{m'}(l_1,l_2) = g_{m'}(l_1,l_2) + \sum_l (g_{m'}(l_1,l) - \delta_{l_1,l}) \frac{e^{+2\lambda S_{mm'}}}{R_{m'}} g_{m'}(l,l_2), \tag{3.3.27}$$

which follows from Dyson equation 3.3.18.

Finally, the physical Green's function is calculated as:

$$G_m^{physical}(\tau_l, \tau_{l'}) = \frac{1}{Z} Tr_{S_{mm'}} g_m(l,l') detO_m[\{S_{mm'}\}]. \tag{3.3.28}$$

Now we can describe implementation of Hirsch-Fye algorithm in QMC code:

(1) The calculation starts from discretized version of Weiss function $\mathcal{G}(\tau)$, which must be provided as input file (see for details section 3.5). Weiss function is used from the previous iteration of DMFT loop or guessed on the first step.

(2) The Green's function $G_m(\tau_l, \tau_{l'})$ for an arbitrary initial configurations of $S_{mm'}(\tau_l) = \pm 1$ is calculated by explicit inversion of matrix A 3.3.19-3.3.20.

(3) From then on, configurations are visited using single spin flip at time τ_l. The determinants 3.3.22 and their product 3.3.22 are calculated. If the heat bath condition allows acceptance of the spin flip, Green's functions are updated with 3.3.26-3.3.26. After specified number of so called dirty updates the clean update of Green's function is done using formulas 3.3.19 and 3.3.19.

(4) The physical Green's function is determined as averages of configuration-dependent functions $g_m(\tau_l, \tau_{l'})$ 3.3.28.

3.4 Analytical Continuation

The output of DMFT loop is Green's function at imaginary time. To analytically continue to the real axis we used standard technique called Maximum Entropy method (MEM) [70], which was developed to circumvent the solution of the following integral equation:

$$G(\tau) = \int d\omega f(-\omega) e^{-\tau\omega} A(\omega). \tag{3.4.29}$$

Here $A(\omega)$ is the unknown spectral function and $f(\omega)$ is the Fermi function. The solution of Eq. 3.4.29 is known to be numerically ill-posed problem since at large positive and negative frequencies the kernel of 3.4.29

$$K(\tau, \omega) = f(-\omega) e^{-\omega\tau} = \frac{e^{-\omega\tau}}{1 \pm e^{-\omega\tau}} \tag{3.4.30}$$

is exponentially small, so the high frequency features of $A(\omega)$ depend upon subtle features in $G(\tau)$. Furthermore, obtaining $G(\tau)$ from QMC complicates the problem as the data are incomplete and noisy.

The MEM combines the use of Bayesian inference and the principle of maximum entropy. The ill-posed inverse problem 3.4.29 strictly speaking has an infinite number of solutions because of insensitivity to high-frequency details of $A(\omega)$ and noisy QMC information about $G(\tau)$. The idea of MEM is to choose among those solutions spectral density which is the most probable. The non-negativity

($A(\omega) > 0$ for fermions) and normalizibility ($\int_{-\infty}^{\infty} A(\omega)d\omega < \infty$) allows one to interpret spectral density as a probability function. If we choose as events functions $\bar{G}(\tau)$ and $A(\omega)$, where $\bar{G}(\tau)$ is measured value of $G(\tau)$, then the criterion for a best solution will be a function that maximizes the conditional probability $Pr[A|\bar{G}]$ over all possible A. The Bayes's theorem gives the following equality:

$$Pr[A|\bar{G}] = Pr[\bar{G}|A]Pr[A]/Pr[\bar{G}]. \tag{3.4.31}$$

Thus, the problem of maximization with respect to A breaks down into two parts: (1) maximize $Pr[\bar{G}|A]$, and (2) maximize $Pr[A]$.

The maximization of $Pr[\bar{G}|A]$ can be done with a maximum likelihood method. Using the data to find$A(\omega)$ is type of parameter fitting problem as much as we determine a set $\mathbf{A} = (A_1, A_2, \ldots, A_N)$ of values A at a number of discrete values ω_i of ω. The discrete version of Eq. 3.4.29:

$$G_i = \Sigma_j K_{ij} A_j \Delta\omega_j, \tag{3.4.32}$$

where $K_{ij} = K(\tau_i, \omega_j)$, suggests that a given $\mathbf{A}$ makes a specific prediction for a set of $G(\tau)$ values $\mathbf{G} = (G_1, G_2, \ldots, G_L)$ at various discrete values τ_i of τ. In the maximum likelihood method, the $\bar{G}(\tau)$ are regarded as random variables drawn from a likelihood function $f(\mathbf{G}; \bar{\mathbf{G}})$ specified by $\mathbf{G}$. For a single $\bar{\mathbf{G}}^{(j)}$ the number $dP^{(j)} = f(\bar{\mathbf{G}}^{(j)}; \mathbf{G})d\mathbf{G}$ represents probability for given measurement to occur. For M independent measurements, $dP = \prod_{j=1}^{M} f(\bar{\mathbf{G}}^{(j)}; \mathbf{G})d\mathbf{G}$. The logarithm of the likelihood function is $L = \sum_{j=1}^{M} f(\bar{\mathbf{G}}^{(j)}; \mathbf{G})$ and thus $Pr[A|\bar{G}] \propto e^{-L}$. The method of maximum likelihood is based on the assumption that a single peak in the space of the parameters $\mathbf{G}$ dominates likelihood function and when the number of measurements become large, by Central Limit Theorem:

$$Pr[A|\bar{G}] \propto e^{-L} = e^{-\chi^2/2} \tag{3.4.33}$$

where

$$\chi^2 = \sum_{ij}^{L} (\bar{G}_i - G_i)[c^{-1}]_{ij}(\bar{G}_j - G_j) \tag{3.4.34}$$

and

$$\bar{G}_i = \frac{1}{M}\sum_{j=1}^{M} \bar{G}_i^{(j)}. \tag{3.4.35}$$

C is the covariance matrix

$$C_{ik} = \frac{1}{M(M-1)}\sum_{j=1}^{M}(\bar{G}_i - \bar{G}_i^{(j)})(\bar{G}_k - \bar{G}_k^{(j)}). \tag{3.4.36}$$

The principle of maximum entropy says that the values of a probability function $A(\omega)$ are to be assigned by maximizing the entropy, and thus

$$Pr[A] \propto e^{\alpha S}, \tag{3.4.37}$$

where entropy term S takes form

$$S[A] = -\int d\omega\{A(\omega) - m(\omega) - A(\omega)ln[A(\omega)/m(\omega)]\}. \tag{3.4.38}$$

Here $m(\omega)$ is so called default model, usually constant, or, alternatively, taken to be the solution of the same model but calculated by an approximation.

Substitution of results 3.4.33 and 3.4.37 into Bayes's formula 3.4.31 gives:

$$Pr[A|\bar{G}] \propto e^{Q} \tag{3.4.39}$$

with a new functional to be maximized:

$$Q[A] = \alpha S[A] - \frac{1}{2}\chi^2[A]. \tag{3.4.40}$$

For each value of parameter α, numeric maximization of Q gives the corresponding spectral function $A(\omega)$. The classical MEM[71] incorporates empirical Bayesian methods to fix the parameter α. Making explicit the dependence in 3.4.31 on α:

$$Pr[A, \alpha|\bar{G}] = Pr[\bar{G}|A]Pr[A|\alpha]Pr[\alpha]/Pr[\bar{G}], \tag{3.4.41}$$

one can obtain the following algebraic equation for α:

$$-2\alpha S(\alpha) = Tr\{\Lambda(\alpha)[\alpha I + \Lambda(\alpha)]^{-1}\}. \tag{3.4.42}$$

Here $S(\alpha)$ in the solution A^α which maximizes Q, and $\Lambda(\alpha)$ is:

$$\Lambda(\alpha)_{ij} = \sqrt{A_i^\alpha}[K^T C^{-1} K]_{ij} \sqrt{A_j^\alpha}. \tag{3.4.43}$$

$K_{ij} \equiv K(\tau_i, \omega_j)$ i discretized kernel and $A_i = A(\omega_i)d\omega_i$ and C_{ij} is defined above covariant matrix.

3.5 Technical note on the DMFT run

Here we describe technical details on the conduction of DMFT run.

Code compilation.

To compile QMC code the file *param.dat*, containing information about imaginary time step and number of bands must be provided. The example of the file *param.dat* is shown below in Table 3.5. We used mesh of imaginary time axis $\Delta\tau = \beta/L$ with $L = 128$. Also, we considered case of three bands. The corresponding parameter is Nlm, the total number of bands is controlled by parameter $Nd = 2Nlm$.

Table 3.2: Example of param.dat

IMPLICIT REAL∗8 (A-H,O-Z)
parameter(L= 128, Iwmax= 2 ∗ ∗13, Nom=Iwmax+1)
parameter(Nlm= 3,Nd= 2∗Nlm,Nf=Nlm∗(Nd−1),Ns= 1)
complex*16 ci
parameter (ci=(0.d0,1.d0))
parameter (pi=3.1415926535898d0)
common/global/Beta,Zero,One,Two

By default the degeneracy among bands trough computations is forced by parameter SUN. Since in our calculations the degeneracy among t_{2g} bands is broken we put in *main.f* flag SUN=.FALSE.

Input files.

Once the code is compiled to make QMC run one has to provide three files: *inp,*

Table 3.3: Explanation of input parameters in *param.dat*

L	– Number of time slices
Iwmax	– Number of points on imaginary frequencies axis
Nlm	– Number of orbitals
Nd	– Number of orbitals with accounted spin degeneracy
Nf	– Number of Ising spins

pdos.in, and *g0init*. Below we explain the contents of each file. The template used for file *inp* is demonstrated in Table 3.5. The meaning of input parameters is explained in Table 3.5.

Table 3.4: Example of *inp* file.

3.0	0.0		U,	J	
16	280000		Beta,	Nsweep	
0.0	0.0	1.0	Ef,	dEf,	Znm (Not used if def=null)
0	20	1	istart,	nscf,	iout
0.5	0.0005		alpha,	small	
1	T		NewFourier	FS (T or F)	
T	F		TBDOS	(T or F)	

Once parameter TB in file *inp* set to be TRUE, the file *pdos.in* must be provided. The file contains Nlm+1 columns. The first column must list energies with prescribed by *param.dat* mesh, and the other Nlm columns – partial renormalized DOSes. The file can be prepared in the following 3 steps:

1. LDA DOS around Fermi level is selected with identifiable bandwidth D.

2. LDA DOS are renormalized to range: $D \rightarrow [-1:0; 1:0]$

3. The derived DOS is extended by zeros to be defined on range $[-10, 10]$.

4. The energy mesh is redefined to contain Iwmax number of points

5. the integrated intensity of all bands in renormalized to be 1.0 per spin.

Table 3.5: Explanation of input parameters in *inp*

U, J	– Hubbard parameters
beta	– inverse temperature
Nsweep	– number of Mote-Carlo sweeps
Ef	– the chemical potential
dEf	– energy step to search Fermi level
	= 0 the chemical potential is fixed and program finds doping
	else the doping is fixed (znum) and program searches for Ef
znum	– Guess for doping
istart	– controls status of file *Sig* containing self-energy
	= 0 program does not read *Sig*
	= 1 program reads in self-energy from *Sig*, but does not rewrites it
	= 2 program reads and rewrite self-energy stored in file *Sig*
nscf	– maximal number of iterations
iout	– controls output files
	= 0 keeps only one last iteration in output files
alpha	– small mixing coefficient (of the order of 0.05-0.5)
small	– Self-consistency threshold for self-energy
NewFourier	– identify different Fourier Transformation (FT) routines to be used
	= 1 most precise scheme (first derivatives of function to be provided)
	= 2 less precise scheme (the moments of the function to be provided)
	= 3 least precise scheme (does not requires any information)
FS	provides extrapolated first derivatives in FT1 (LOGICAL)
TB	– chooses between semicircular and arbitrary DOS (LOGICAL)
	=F, then semicircular DOS is used
	=T, DOS in file *pdos.in* (must be provided) is used
LSC	– reserved for external **k**-summations (LOGICAL)

The result of this procedure for the case of paramagnetic CrO_2 is shown in Figure 3.1.

The third input file *g0init* must contain 2∗Nlm+1 columns corresponding to τ, $\mathrm{Re}\,\mathcal{G}_i(\tau)$, $\mathrm{Im}\,\mathcal{G}_i(\tau)$ for $i = 1, 2, \ldots$,Nlm. The functions must be given for the negative $L/2$ time slices. We chose the initial Weiss function to be $\mathrm{Re}\,\mathcal{G}_i(\tau) = \mathrm{Im}\,\mathcal{G}_i(\tau) = \tau$ for $\tau < 0$ and $i = 1, 2, 3$.

Analytical continuation.

The output of QMC code is Green's function on the imaginary time axis. To

find the spectral density we use the maximum entropy code for the analytical continuation to the real axis. The *MaxEnt* code takes two input files and produces output file with partial DOSes. The first input file called *inpmax* contains information about input parameters of MEM and its example shown in Table 3.5. We run *MaxEnt* code separately for each band, thus number of degenerate bands (first line in *inpmax*) equals 1. The explanation of the other parameters is given in Table 3.5.

Table 3.6: Example of *inpmax* file.

1		! Ns	
65		! L	
1	0.004	! idg,	delta-G
16.0		! Beta	
600		! Ne	
0.02		! De	
3000		! Nmc	
1200		! alpha	
1		! Nrun	
1234		! rand	
0	0.040	! iflat,	eim
-1.5	1.0	!mu	U

The other input file called *Gtau1.dat* must contain imaginary time mesh, real and imaginary parts of Green's function for the given band. The output of *MaxEnt* is written to the files with name *dos.*

3.6 Calculated DOSes and observation of OSMT

The DOS for different pairs of (s, U) parameters are shown in Figures 3.2-3.6.

Table 3.7: Explanation of input parameters in *inpmax*

Ns	– number of time slices
L	– number of time slices, defined in QMC code
idg	– identifies way the model function for MEM is built
delta-G	– deviation from GF (recommended 0.001-0.005 range)
Beta	– inverse temperature
Ne	– number of points on real axis (maximum 600)
de	– frequency step on real axis
Nmc	– number of annealing steps
alpha	– α parameter in functional 3.4.42
Nrun	– number of smoothing runs
rand	– random seed number
Iflat	=0 selects default model in 3.4.38 to be a constant
Eim	– irrelavant for the choice of iflat = 0
mu	– chemical potential
U	– Coulomb repulsion

We start discussion with case of $s = 0.0$, i.e. when paramagnetic LDA partial DOSes were used in self-consistency condition 3.2.3. In Figure 3.2 the DOSes for narrow $t_{2g}^{||}$ and broad $t_{2g}^{\perp}$ bands are shown as function of Coulomb repulsion U measured in half bandwidth of broad LDA band. For $U = 1.0$ the narrow band becomes almost unoccupied shifting its spectral weight higher the Fermi level. The broad band stays half-filled and increases in bandwidth. Both bands formed sharp quasiparticle peaks and noticeable upper and lower Hubbard bands. As U increases to value of 2.0 the Hubbard bands become bigger accumulating spectral weight from quasiparticle peak. The narrow band is already approaching insulating stage as Coulomb parameter is usually quite small for transition oxides. Finally, at $U = 3.0$ the narrow band underwent localization transition, and broad band approaching it while still being conducting. The last plot of Figure 3.2 suggests that localization transition occurs at different values of U for narrow and broad t_{2g} bands.

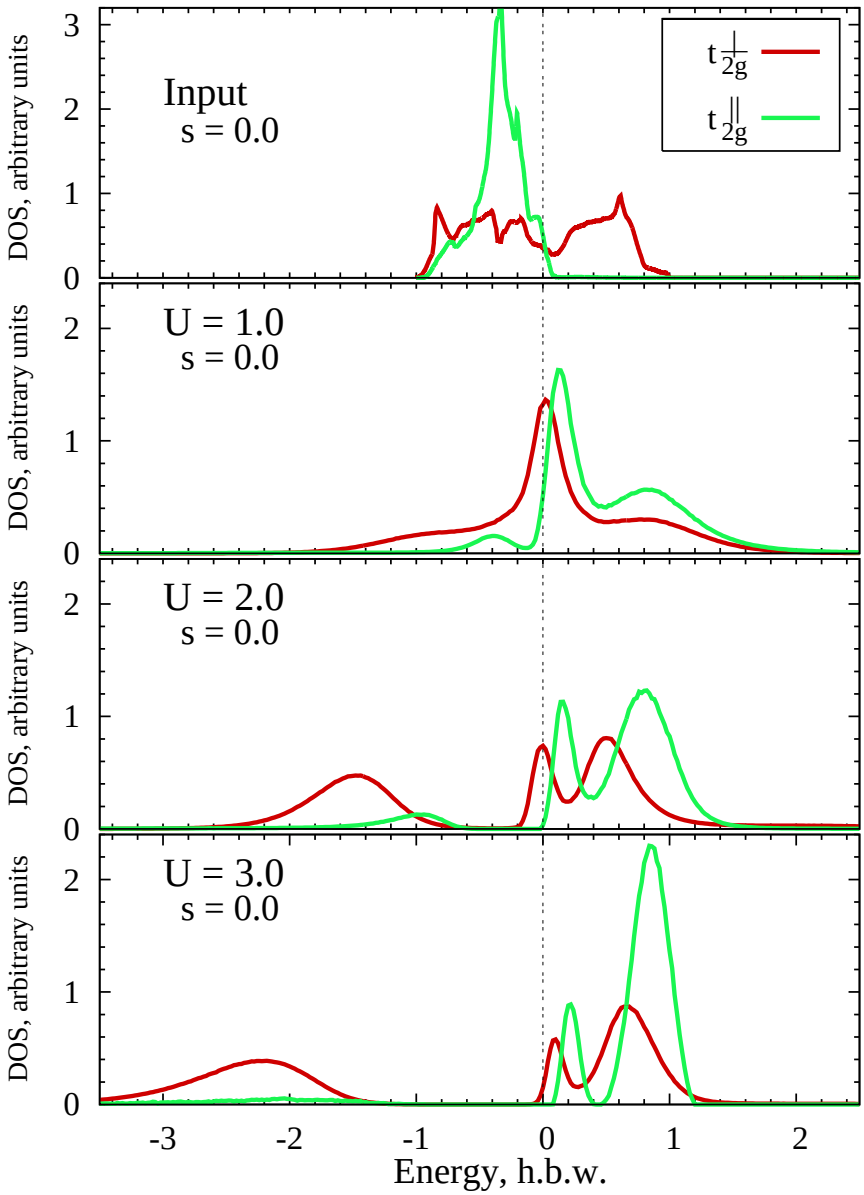

Figure 3.2: DOS for $s = 0.0$ and $U = 0.0$, 1.0, 2.0 and 3.0.

Since DOSes are derived through analytical continuation of Green's function from imaginary times to the real axis employing MEM which by construction may produce small noises. To assure the insulating behavior of narrow band at $U = 3.0$ we show in Figure 3.3 the imaginary part of Green's function on the axis of imaginary frequencies which is output of QMC routine. The shape of $\mathrm{Im}\, G_{t_{2g}^{\perp}}(i\omega_n)$ suggests that broad band remains conducting up to $U = 3.0$, while $\mathrm{Im}\, G_{t_{2g}^{II}}(i\omega_n)$ curves up for $U = 2.0$

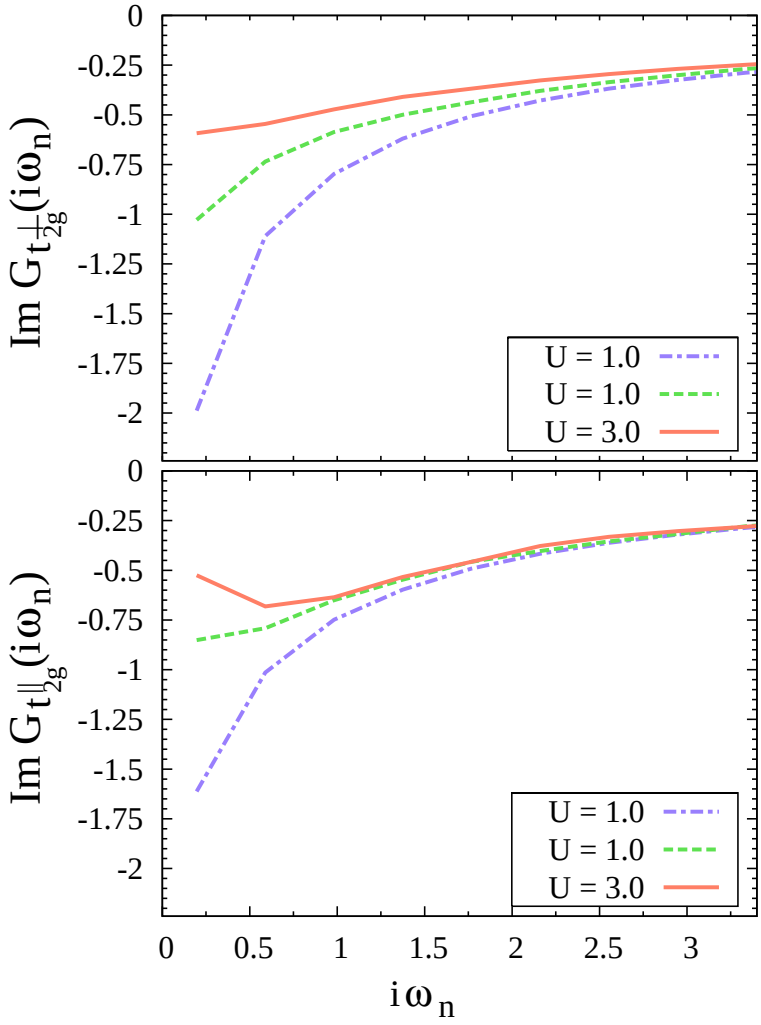

Figure 3.3: The imaginary part of Green's function on imaginary frequencies axis for broad (top) and narrow (bottom) bands for different values of U.

In Figure 3.4 the DOS are shown for the case $s = 0.1$ h.b.w. The third panel of Figure 3.4 demonstrate that already for $U = 2.0$ the narrow band becomes insulating while the broad band still metallic with almost smoothed out quisiparticle peak. The fourth panel of Figure 3.4 shows that for $U = 3.0$ both bands developed upper and lower Hubbard bands which are separated by $\approx$ 1.2eV energy gap.

The comparison of Figures 3.2 where $s = 0.0$ and 3.4 where $s = 0.1$ leads to the conclusion that localization transition occurs for smaller values of U in the case of $s = 0.1$. Also, while in the case of $s = 0.0$ narrow band becomes almost

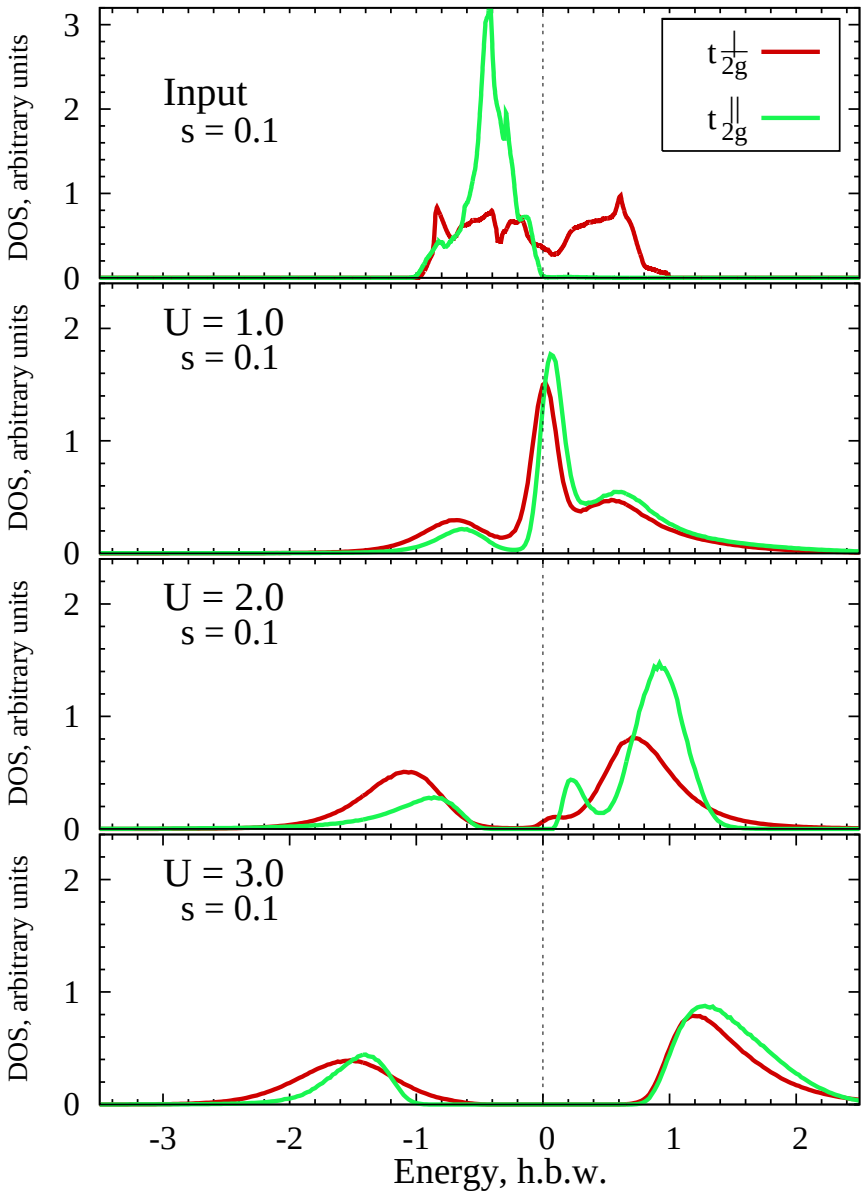

Figure 3.4: DOS for $s = 0.1$ and $U = 0.0$, 1.0, 2.0, and 3.0.

fully unoccupied, in the case of $s = 0.1$ the spectral weight of broad and narrow bands become comparable below the Fermi energy.

This tendency of the narrow band to become more occupied and leave more spectral weight below the Fermi level persists with further increase of parameter s. As a result more and more spectral weight of the broad band is pushed above the Fermi level. The dynamics of spectral weight redistribution can be traced in Figures 3.5 and 3.6. All three panes of the Figure 3.6 where $s = 0.4$ indicate the situation opposite to one when $s = 0.0$ (see Figure 3.6). Now the narrow band

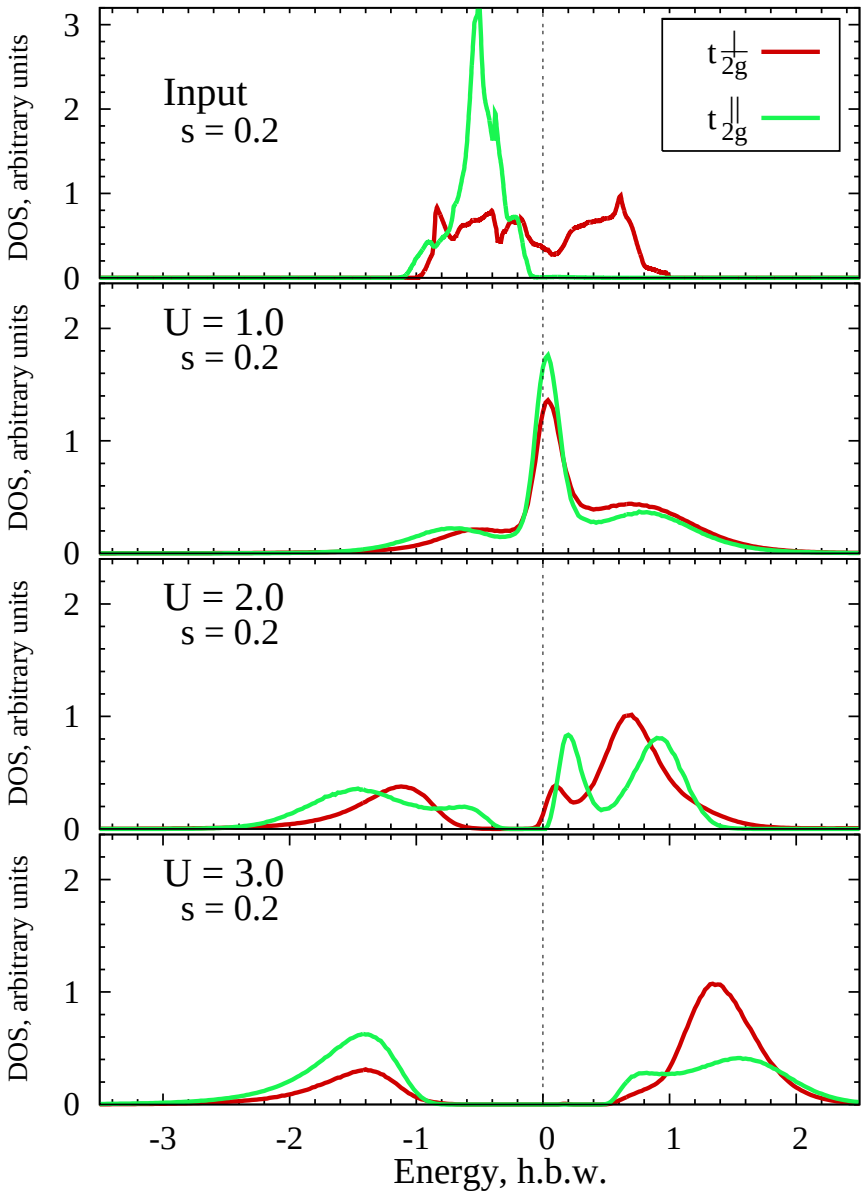

Figure 3.5: DOS for $s = 0.2$ and $U = 0.0$, 1.0, 2.0, and 3.0.

is almost completely occupied, but the broad band shifted all its spectral weight above the Fermi level. It should be noticed that increase of s did not accelerate further the localization transition with increase of U.

We studied the redistribution of electron density between the narrow and broad bands in the space of parameters (U, s). The three lower panels of Figure 3.7 present partial occupancies of narrow and broad bands per spin as function of parameter s for U =1.0, 2.0 and 3.0. First, we discuss case $U = 1.0$ (see

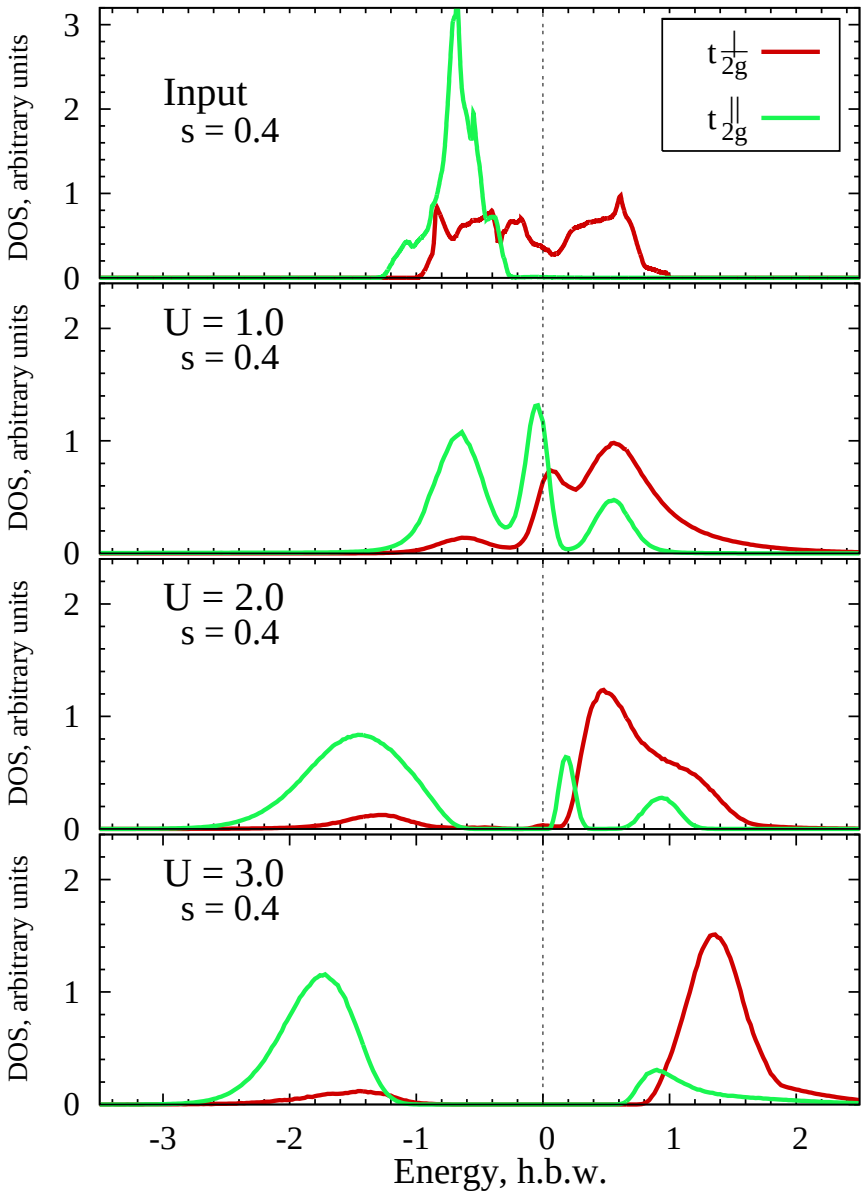

Figure 3.6: DOS for $s = 0.4$ and $U = 0.0$, 1.0, 2.0, and 3.0.

to panel of Figure 3.7). Here and later, the occupancies of broad bands represent the summary electron occupancy of two degenerate broad bands per spin. The total occupancy of all three bands is also demonstrated to be 1 per spin as expected. For small values of parameter s, i.e. if one starts with LDA DOSes, the narrow band becomes almost completely unoccupied left with only $\sim 15\%$ of total electron density. The situation is changing rapidly with increase between initial relative positions of narrow and broad bands. As s becomes bigger by magnitude the narrow band is accumulating electron density leaving broad bands

less occupied. At $s \approx -0.28\, h.b.w.$ the narrow and broad bands have equal occupancies of 0.5 each. This cross-section is followed by the narrow band being more and more occupied and the broad bands correspondingly unoccupied. Finally at $s \approx -0.6\, h.b.w.$ the narrow band gains almost 100% of electron density pushing the broad bands above Fermi energy.

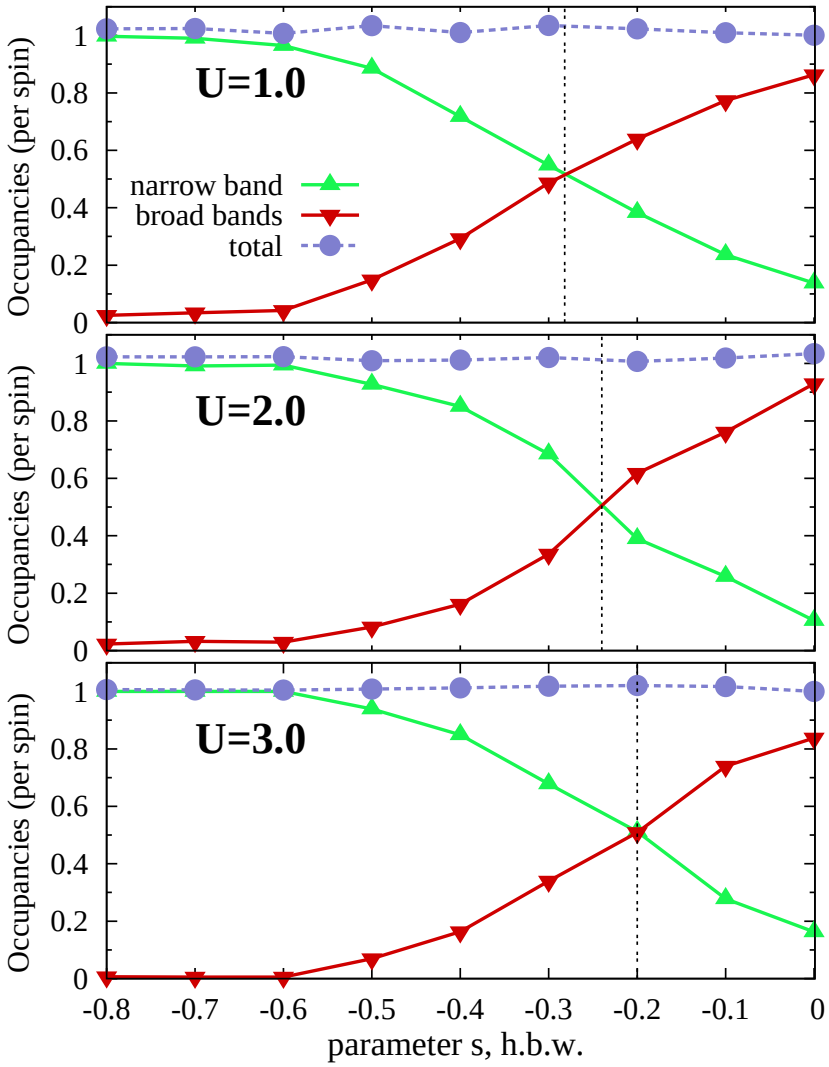

Figure 3.7: The partial occupancies of broad and narrow bands as a function of parameter s for different values of U. The dashed vertical line in each panel indicates that the transition occurs for s with smaller magnitudes as U increases.

In the cases of $U = 2.0$ and $U = 3.0$ the similar dynamics of electron density can be observed with correction that the cross-section occurs for smaller values of parameters s. For $U = 2.0$ the transition takes place at $s \approx -0.24\, h.b.w.$ and for $U = 3.0$ at $s \approx -0.28\, h.b.w.$

Thus, a very small difference (of ≈ 0.5 eV) in the parameter s leads to completely different physics. As s varies from 0 to ≈ -0.5 eV the three possible scenarios of orbital selective Mott transition take over each other:

Scenario 1 ($\mathbf{s \lesssim 0.1}$) – the broad band undergoes a localization transition while the narrow band shifts above the Fermi level (see Figure 3.8).

Scenario 2 ($\mathbf{0.1 \lesssim s \lesssim 0.4}$) – both broad and narrow bands undergo a localization transition (see Figure 3.9).

Scenario 3 ($\mathbf{0.4 \lesssim s}$) – the broad band shifts its spectral weight while the narrow band stays completely occupied (see Figure 3.10).

The extreme sensitivity to the small changes of parameter s suggests that CrO_2 is on the edge of a quantum transition. The discussion in the previous chapter implies that parameter $s \approx 0$ in CrO_2, indicating the scenario 1 of Mott transition (Figure 3.8).

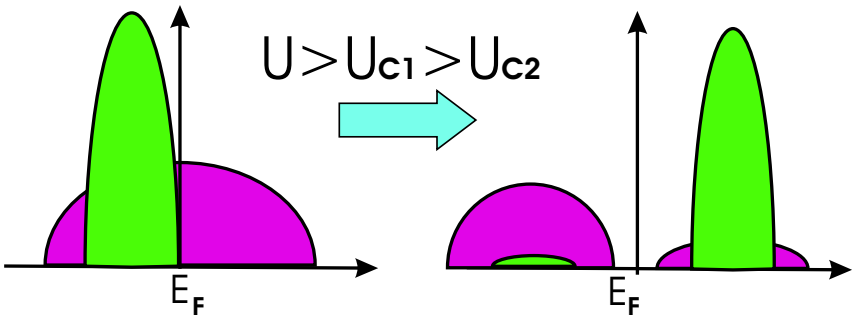

Figure 3.8: Schematic representation of Scenario 1 of OSMT. Under application of Coulomb repulsion U broad band undergoes localization transition, forming upper and lower Hubbard bands while narrow band from completely occupied becomes almost completely unoccupied. The scheme is shown for big values of U ($U > U_{c1} > U_{c2}$), where U_{c1} and U_{c2} – critical U for broad and narrow band correspondingly.

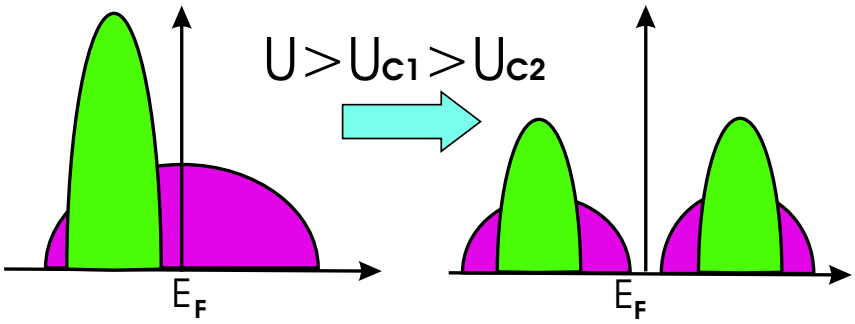

Figure 3.9: Schematic representation of Scenario 2 of OSMT. Under application of Coulomb repulsion U both broad and narrow bands undergo localization transition. The scheme is shown for big values of U ($U > U_{c1} > U_{c2}$), where U_{c1} and U_{c2} – critical U for broad and narrow band correspondingly.

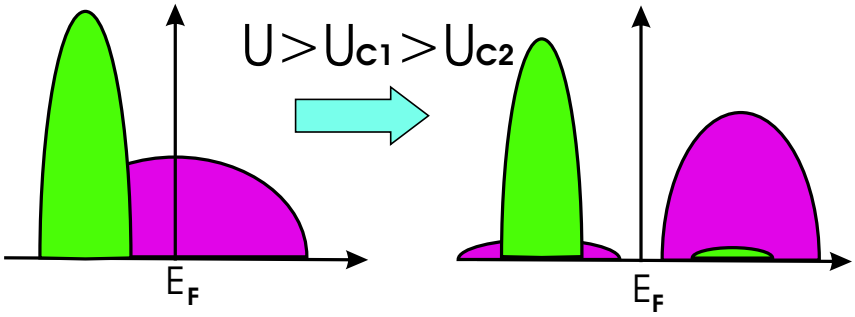

Figure 3.10: Schematic representation of Scenario 3 of OSMT. Under application of Coulomb repulsion U broad band becomes completely unoccupied and narrow band stays completely occupied. The scheme is shown for big values of U ($U > U_{c1} > U_{c2}$), where U_{c1} and U_{c2} – critical U for broad and narrow band correspondingly.

3.7 Model Hartree calculations

To investigate the role of many-body effects in considered quantum transition we perform model Hartree calculations for three bands with semicircle DOSes. Namely, we have three bands, each of them is normalized to have on electron. Two bands are degenerate, broad and half filled. The third narrow band is fully occupied, has width twice as less and shifted down to have its upper edge exactly at the Fermi level. The initial density of states is shown in Figure 3.7.

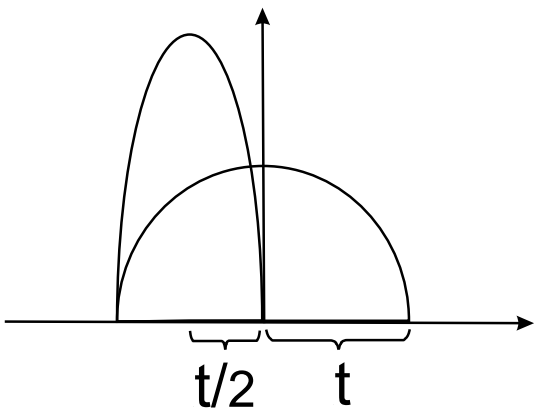

Figure 3.11: Input DOS for model Hartree calculations.

Let's recall that the self-consistency condition in DMFT for one-band case is:

$$\sum_{\mathbf{k}} \frac{1}{\omega + \mu - \epsilon_{\mathbf{k}} - \Sigma_{imp}(\omega)} = \frac{1}{\omega + \mu - \Sigma_{lat}(\omega) - \Delta(\omega)}, \qquad \Sigma_{imp}(\omega) = \Sigma_{lat}(\omega). \tag{3.7.44}$$

Here $\Sigma_{imp}(\omega)$ is self-energy of the impurity, $\Sigma_{imp}(\omega)$ is self-energy of the particle in the lattice, $\Delta(\omega)$ is the bath spectral density, and μ is chemical potential. For Bethe lattice $\Delta(\omega)$ and Weiss function are related through

$$\Delta(\omega) = t^2 \mathcal{G}\omega, \tag{3.7.45}$$

where t is hopping parameter.

Let's denote by indexes 1 and 2 two degenerate broad bands and by index 3 narrow band. Then $t_1 = t_2 = 2t_3 = t$ and by n_i we will refer to the occupancy of i-th band. Then for three bath Green's functions, using condition 3.7.45 we have self-consistent quadratic equations:

$$\begin{aligned} \mathcal{G}_i &= \frac{1}{\omega + \mu - \Sigma_i - t_i^2 \mathcal{G}_i} \\ \Rightarrow \quad -t_i^2 \mathcal{G}_i^2 + (\omega + \mu - \Sigma_i)\, \mathcal{G}_i - 1 &= 0, i = 1, 2, 3, \end{aligned} \tag{3.7.46}$$

which have the following solutions:

$$\mathcal{G}_i = \frac{1}{2t_i^2}[\,\omega + \mu - \Sigma_i \pm \sqrt{(\omega + \mu - \Sigma_i)^2 - 4t_i^2}]. \tag{3.7.47}$$

In the Hartree approximation:

$$\Sigma_i = U(N - n_i), \tag{3.7.48}$$

where $N = n_1 + n_2 + n_3$. Since occupancies can be found out as:

$$n_i = -\frac{1}{\pi}\int_{-\infty}^{\mu} \text{Im } \mathcal{G}_i(\omega)d\omega, \tag{3.7.49}$$

one finally can obtain the following system of equations:

$$\begin{aligned} n_1 &= n_2 \\ n_1 + n_2 + n_3 &= N \\ n_1 &= \frac{2}{\pi}\int_{-\infty}^{(\mu - U(N-n_2-n_3))/2t} \sqrt{1-z^2}dz \\ n_3 &= \frac{8}{\pi}\int_{-\infty}^{(\mu+s+t/2-U(N-n_1-n_2))/t} \sqrt{1-z^2}dz \end{aligned} \tag{3.7.50}$$

With $N = 2$, $n_1 = n_2 = n$ and therefore $n_3 = 2 - 2n$, this system can be rewritten as system of two equations for μ and n. Parameters t, s and U we assume to be given:

$$\begin{aligned} n &= \frac{2}{\pi}\int_{-\infty}^{(\tilde{\mu}-\tilde{U}n)/2} \sqrt{1-z^2}dz, \\ 1-n &= \frac{4}{\pi}\int_{-\infty}^{\tilde{\mu}+0.5+\tilde{s}-2\tilde{U}(1-n)} \sqrt{1-z^2}dz. \end{aligned} \tag{3.7.51}$$

Here $\tilde{\mu}$, $\tilde{s}$ and $\tilde{U}$ are measured in terms of half band width of broad band t.

Using the fact that

$$\int \sqrt{1-z^2}dz = -\frac{1}{2}\arcsin z + \frac{1}{2}z\sqrt{1-z^2} \tag{3.7.52}$$

one finds:

$$\begin{aligned} n = \frac{1}{2} + \frac{1}{\pi}\arcsin\left[\frac{\tilde{\mu}-\tilde{U}n}{2}\right] - \frac{1}{\pi}\frac{\tilde{\mu}-\tilde{U}n}{2}\sqrt{1-\left[\frac{\tilde{\mu}-\tilde{U}n}{2}\right]^2} \\ -n = \frac{2}{\pi}\arcsin[\tilde{\mu}+\tilde{s}-2\tilde{U}(1-n)] \\ -\frac{2}{\pi}[\tilde{\mu}+\tilde{s}-2\tilde{U}(1-n)]\sqrt{1-[\tilde{\mu}+\tilde{s}-2\tilde{U}(1-n)]^2} \end{aligned} \tag{3.7.53}$$

The numerical solution of the system 3.7.53 gave the curves for occupancies of broad and narrow bands compared to the ones provided by QMC in Figure 3.7. The same slope but still quite different shape suggests that Hartee approximation can be used as tool to see general tendency of electron density redistribution but consideration of many-body effects is crucial in CrO_2.

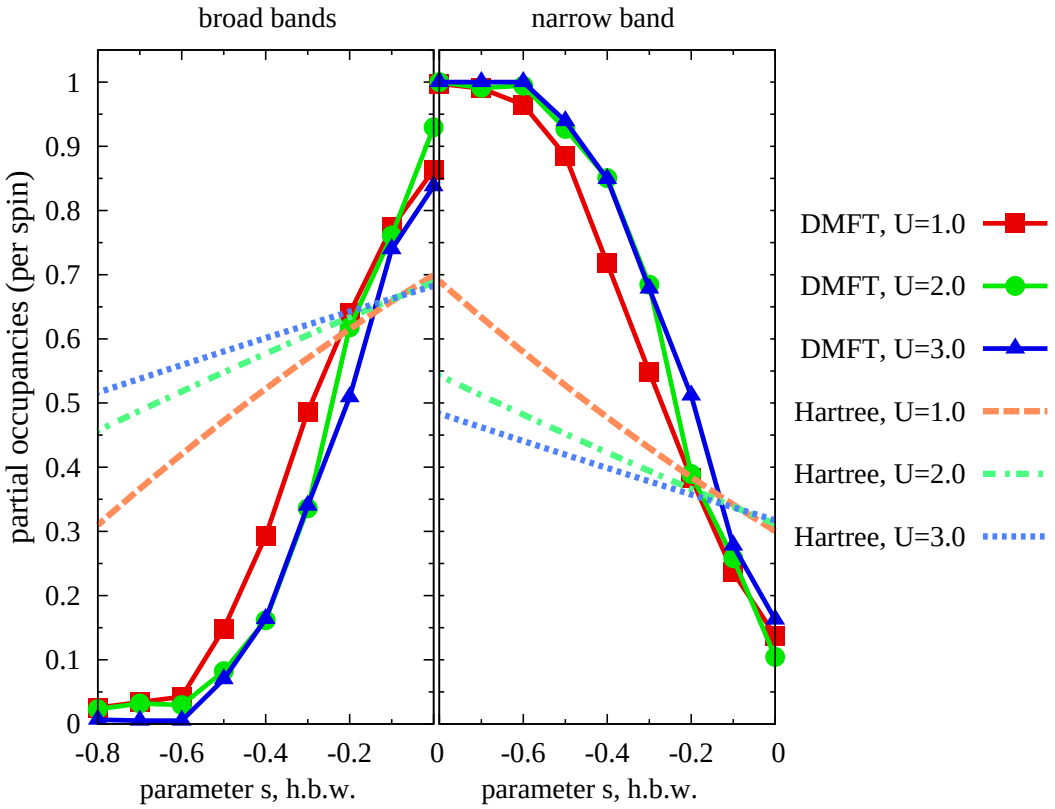

Figure 3.12: The occupancies calculated in Hartree approximation are compared to occupancies calculated within DMFT with QMC impurity solver for broad bands (left panel) and narrow band (right panel).

3.8 Conclusion

In this chapter we used the DMFT technique with QMC impurity solver to show that normal state of CrO_2 is on the edge of a quantum transition when small energy scales (≈ 0.5 eV) lead to the phases with completely different physics. Also, we observed OSMT taking place in t_{2g} manifold of Cr atoms. The application of

considerably small Coulomb repulsion U to the t_{2g} orbitals lead to the opposite of intuitively expected result when the broad initially half-filled band undergoes localization transition while the narrow band where applied U must be effectively stronger becomes completely unoccupied.

Chapter 4

Electronic structure of actinides under ambient pressure

In this chapter we discuss in details the localization-delocalization transition in actinides, accompanying low-energy physics, and appropriate model for its description within one-electron picture. The first section is devoted to the review of basic facts of actinide physics and theoretical studies reported earlier in the literature. In section 4.2 various LMTO basis sets are analyzed in order to determine a robust bare Hamiltonian for the actinides. Finally, having chosen a basis we report a detailed analysis of the one-electron band-structure of actinides in Section 4.3. The hybridization between f- an *spd*- states is compared with the $f-f$ hopping in order to understand the Anderson-like and Hubbard-like contributions to itineracy in the actinides. We show that both contributions decrease strongly as one move from the light actinides to the heavy actinides.

4.1 Introduction

4.1.1 Background of the actinides

The actinide series encompasses the 15 chemical elements that lie between actinium and lawrencium on the periodic table, with atomic numbers 89 - 103 and generally characterized by filling $5f$ sub-shell. Here we will concentrate on the part of series from Thorium till Einsteinium. The corresponding valent states of those elements are provided in Tables 4.1 and 4.2.

Table 4.1: Valent states of Actinides I.

$\mathbf{Th}^{90}_{232}$	$\mathbf{Pa}^{91}_{231}$	$\mathbf{U}^{92}_{238}$	$\mathbf{Np}^{93}_{237}$	$\mathbf{Pu}^{94}_{244}$
$6d^2 7s^2$	$5f^2 6d^1 7s^2$	$5f^3 6d^1 7s^2$	$5f^4 6d^1 7s^2$	$5f^6 6d^0 7s^2$

Table 4.2: Valent states of Actinides II.

$\mathbf{Am}^{95}_{243}$	$\mathbf{Cm}^{96}_{247}$	$\mathbf{Bk}^{97}_{247}$	$\mathbf{Cf}^{98}_{251}$	$\mathbf{Es}^{99}_{252}$
$5f^7 6d^0 7s^2$	$5f^7 6d^1 7s^2$	$5f^9 6d^0 7s^2$	$5f^{10} 6d^0 7s^2$	$5f^{11} 6d^0 7s^2$

It is well accepted [72] that the actinides are divided into two groups based on the behavior of the $5f$-electrons. The lighter actinides (Th to Pu) have smaller atomic volumes, low-symmetry crystal structures and itinerant $5f$ states that participate in metallic bonding [73]. Alternatively, the heavy actinides (Am to Es) have larger atomic volumes, high-symmetry crystal structures, and relatively localized $5f$-electrons. The disparity in behavior is associated with delocalization-localization transition of $5f$-electrons happening in the vicinity of Pu. In light actinides $5f$-orbitals are not localized due to particular screening of nuclei charge by $4f$-electrons and extend enough to participate in metallic bonding. Narrow $5f$-bands with high density of states at Fermi level result in low symmetry crystal structure and small atomic volumes. As nuclei charge increases with increase of atomic number $5f$-electrons are pulled stronger into the core and at Am become completely localized. As a result unit cell volume increase dramatically (see inset of Figure 4.1) and *spd*-orbitals become solely responsible for bonding favoring high symmetry crystal structures observed in conventional metals.

The big atomic volumes and small bulk modulus make heavy actinides to be "soft" materials. Applying pressure to the heavy actinides results in a series of crystallographic phase transitions, and the respective phases often have significantly smaller volumes [12, 11] (see Figure 4.1). Transitions of this sort are often referred to as "volume collapse" transitions. Given that the application of ample pressure to any system of localized electrons will eventually cause a delocalization

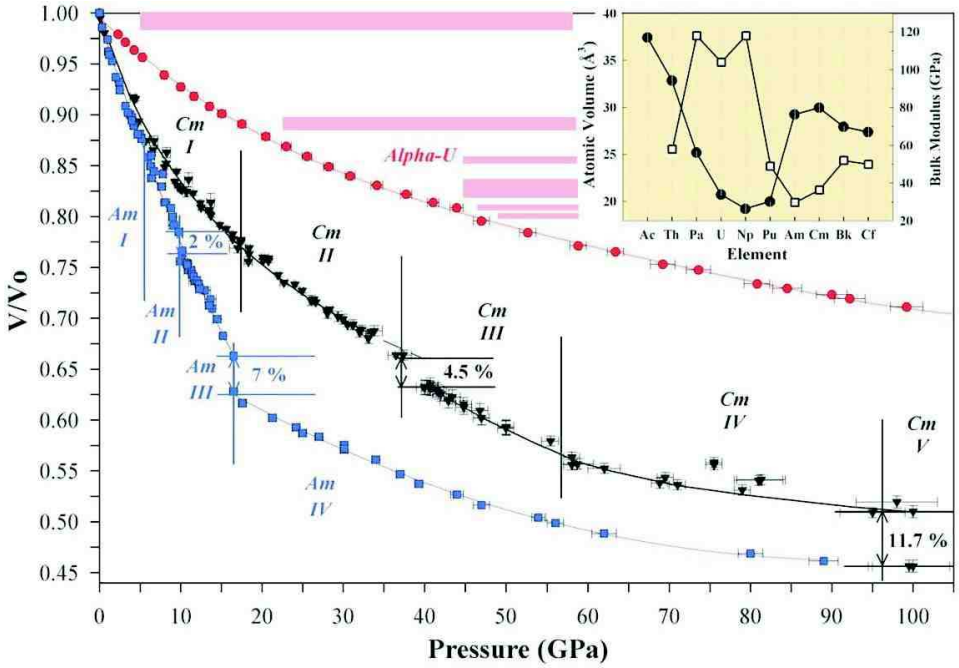

Figure 4.1: Relative volume V/V_0 as a function of pressure for α-uranium [9], Am [10, 11] and Cm [12]. Vertical lines separate the pressure ranges for each Am and Cm (crystallographic) phase. Percentage values indicate the collapses in atomic volume. Unfortunately, I was not able to find the same phase diagram for Pu. The pink strips indicates volumes observed for different crystallographic modifications of Pu (from bottom to top): α-phase, β-phase, γ-phase, ϵ-phase, δ'-phase and, finally, δ-phase. **(Inset)** Ambient pressure atomic volumes and (solid circles, left-hand side) and bulk moduli (open squares, right-hand side) across the actinide series. The plot is copied from [12].

transition, understanding what role the electronic delocalization transition may play in the volume collapse transition has been and continues to be an active area of study [74, 75].

Plutonium is considered to be dividing line of actinide series, with the α- and δ- phases associated with light and heavy behavior, respectively. This dual nature of Pu, along with an enormous 25% volume collapse for the $\delta \rightarrow \alpha$ transition, made Pu the most interesting element among $5f$ compounds for basic theoretical research over the past 50 years [76, 77].

The actinides are among the most complicated classes of materials in terms of understanding electronic correlations given the presence of s, p, d, and f electrons near the Fermi surface and the unusual behavior observed in experiment. Broad

discussion in the literature was devoted to the following questions: abrupt change in volume and bulk modulus [78]; unique crystal structures[73]; partial localization of f-electrons [79], Mott transition [80, 81]; paramagnetism in light actinides and formation of magnetic moments in heavier actinides (starting from Cm) [77].

4.1.2 Earlier reported in literature calculations

Numerous *Ab Initio* electronic structure calculations have been performed for the actinides. Standard DFT based LDA [82, 83] and GGA [84, 85] calculations for experimentally observed paramagnetic ground state gave good results for equilibrium volumes of earlier actinides from Th till Np. However, already for α-phase of Pu there is an underestimation of the theoretical volume comparing with the experimental one [86, 87] and for the δ-phase the disagreement is rather large (more than 20%). Recently it was found that combination of GGA and spin-polarization taken into account results in drastic improvement of the DFT results on equilibrium volume values of Pu phases [75]. However, any improvement in the DFT description inevitably lead to a magnetic ground state of Pu, contrary to experiment [77].

The problem of "first principles" calculations of electronic structure and ground state properties of plutonium is associated with the question how to describe $5f$-electrons localization [88]. A. Svane et al. in [89] accounted for partial localization of $5f$-orbitals using SIC-LSD approximation (SIC for self-interaction correction) which postulates a manifold of coexisting localized and delocalized f-electrons. Authors were able to predict non-magnetic/magnetic ground states for U, Np, Cm and Bk in agreement with experiment. Still, the ground state for Am and Pu were predicted to be magnetic.

The physical origin of localization are correlation effects due to Coulomb interaction between $5f$-electrons. Therefore, such methods as LDA+U and LDA+DMFT

should provide better results in the description of actinides. Indeed, LDA+U calculations for δ-Pu [90, 91] gave a significant increase in the equilibrium volume in good agreement with experiment, but preserved the strong spin-orbit polarization with large values of magnetic moments. Recently, it was found that LDA+U equations can give a non-magnetic solutions [92, 93] for Pu with $5f$-shell in ground state with $S = L = J = 0$ and calculated equilibrium volume is in good agreement with the experimental value. Analogical calculations for Am were carried out in [94]. While LDA+U method was able to solve the problem of $5f$-localization without developing magnetism it fails to predict experimentally observed photoemission spectra missing the quasi–particle peak near the Fermi energy.

Most earlier implementations of the LDA+DMFT approach for plutonium were done by S. Savrasov et. al. in [74]. To solve the impurity problem authors used an interpolative approach with a simple analytical form for self-energy. Another attempt was done in [95, 96] where the authors had started from non-magnetic LDA+U solution and included fluctuation via "spin-orbit T-matrix FLEX approach" based on the perturbation theory in Coulomb interaction parameter U. Recently, both QMC and Hubbard I approaches were used in [97] to solve the impurity problem. All listed calculations provide qualitatively closer description of experimental photoemission spectrum than LDA+U. The recent LDA+DMFT study of Curium has been done in Ref. [98].

4.1.3 Actinide Hamiltonian

We consider the following model Hamiltonian for the actinides:

$$H = \sum_{ija\beta} V_{ija\beta}(c^{\dagger}_{ai} f_{\beta j} + c.c.) + \sum_{ij\alpha\beta} t^{f}_{ij\alpha\beta} f^{\dagger}_{\alpha i} f_{\beta j} + \sum_{\mathbf{k}ab} t^{spd}_{ab}(\mathbf{k}) c^{\dagger}_{\mathbf{k}a} c_{\mathbf{k}b} + \sum_{i\alpha\beta\gamma\delta} U_{\alpha\beta\gamma\delta} f^{\dagger}_{\alpha i} f^{\dagger}_{\beta i} f_{\gamma i} f_{\delta i} \tag{4.1.1}$$

where $f_{\alpha i}$ is the annihilation operator for $5f$-electron in state $\alpha = |j, j_z\rangle$ at site i, and c_{ai} is annihilation operator for conduction electrons in the state $a = |n, j', j'_s\rangle$.

This model can be understood as a periodic Anderson model in which additional direct hopping is allowed between the correlated states. Equivalently, this model can be thought of as a Hubbard model with additional uncorrelated states that hybridize with the correlated states. Therefore, the model for the actinides contains the physics of *both* the periodic Anderson model and the Hubbard model (if the hybridization is set to zero). In the Hubbard model t^f competes with U to determine the degree of localization of the electrons, while in the periodic Anderson model V competes with U. In the model of the actinides t^f and V cooperatively compete with U, and the relative magnitudes of t^f and V will determine the degree of Hubbard-like and Anderson-like contributions to the itineracy of the f-electrons. The main focus of this study is to determine the relative importance of t^f and V across the actinide series. This is the first step towards understanding wether the localization of the f electrons which occurs as one traverses the actinides is an Anderson transition, a Mott transition, or some combination thereof. The *spd* hopping term t^{spd} may be pertinent to the low energy physics of the actinides given that the *spd* electrons may be present at the Fermi energy even if the f electrons are completely localized.

In general, the parameters V and t^f depend on the choice of basis set and therefore are not unique. The secondary objective of this study is to determine the best basis for parameterizing the actinide model. The earlier attempts to construct tight-binding parametrization for actinides resulted in two limited models. The first provided parametrization of f-bands only with spin-orbit coupling incorporated trough intra-atomic matrix elements [99]. The other considered hybridization of f-orbitals with *spd*-orbitals but ignored spin-orbit coupling [100]. We provide details on tight-binding parametrization and comparison to earlier work reported in literature in the next chapter.

4.1.4 Further Motivation

The idea of a Mott transition in the actinides was brought forward by Johansson [101] based on empirical comparison of canonical $5f$-bandwidth with the estimates of the Coulomb interaction in the form of a Hubbard U. Later elaboration of these ideas in the context of the α-δ transition in Pu took place in [102, 103].

The important role of $d-f$ hybridization in actinide metals and alloys was stressed in the early work of R. Jullien et al. [104, 105] who considered a model similar to 4.1.1, including $f-f$ hopping and Coulomb repulsion U. The magnetic solutions of the model were investigated as function of the position of $5f$-band and using reasonable estimates for the rest of the parameters.

In this study, we reconsider the issue of the description of the Mott transition in the actinide series, from a perspective which is motivated by recent DMFT and LDA+DMFT works [98, 96]. These works, have provided further demonstration of the hypothesis that a localization-delocalization transition takes place across the actinide series. However, within the DMFT framework, there are two different roads to localization in a multiorbital model. One possibility is to argue that the bands near the Fermi level have large f character, and form a Hubbard model out of them. This leads to a multiorbital Hubbard model where the Hubbard U is applied to the f bands near the Fermi level. This approach is very successful in the description of transition metals, for which the multiorbital Hubbard model successfully describes the photoemission and the magnetic properties, and the Friedel model describes the bonding properties.

An alternative approach is to retain both f and *spd* bands, and their hybridization term. While the U is still applied to the f states, the localization-delocalization transition which takes place in the f states are driven by the changes in the hybridization. Since the *spd* bands are very broad and always remain metallic, the Mott transition takes place in the f band only, namely this is a realization of the orbitally selective Mott transition, where only a subset of

orbitals go from itinerant to localized. The "metallic" side of the transition is characterized by a Fermi surface containing both f and *spd* electrons, while in the "insulating" or localized side of the transition, the Fermi surface contains only *spd* electrons. In this picture the transition can be driven by either changes in the hybridization or the direct $f - f$ hopping.

While some aspects of localization-delocalization in the Anderson model and the Hubbard model treated by DMFT are very similar at intermediate temperatures [106] (for example they both exhibit a line of first order phase transitions ending at a second order point), there are significant differences at very low temperatures when hybridization becomes a relevant perturbation suppressing Mott transition [28]. Furthermore, the behavior at large U and high temperatures should be quite different in the two models, due to the presence of the broad metallic band in the Anderson model.

To address these issues we study whether the delocalization is driven mainly by changes in the hybridization term, or by changes in the hopping among the f orbitals. This question of course, depends on the definition of what one means by "f electron orbital". In the context of the Hamiltonian (4.1.1) viewed as a truncation of the full many body problem, the f electron orbital is defined by the fact that only the Coulomb interaction on that orbital is retain. More generally, the LDA+U method, and the LDA+DMFT method, require the definition of a set of correlated orbitals.

4.2 Orbitals and basis

4.2.1 Basis set dependence issue

While the issue of representing the Kohn-Sham Hamiltonian in different basis sets has been a subject of numerous studies, the dependence of the results of correlated electronic structure methods such as LDA+DMFT on the choice of

Table 4.3: Choice of basis.

Bare LMTO Löwdin transform	**Screened LMTO** Löwdin transform
Bare LMTO projective basis	**Screened LMTO** projective basis

correlated orbitals is only beginning to be explored [107].

In this study, we investigate the role of the choice of the correlated f orbital. We first take the f electron orbital as the f element of the LMTO basis, both in the bare and screened representations [108, 109]. The LMTO basis is non-orthogonal and therefore must be orthogonalized in order to avoid the complications of solving the many-body problem in a non-orthogonal basis. As we will show in this study, the method of orthogonalization has a large influence on the results. We utilize both the Löwdin orthogonalization [110] and the projective orthogonalization [111, 98] that was used in earlier implementations of LDA+DMFT. This effectively results in four different constructions of f orbitals, listed in Table 4.3.

4.2.2 Bare and Screened LMTO within ASA scheme

The basis set of linear muffin-tin orbitals (LMTOs) has been extensively used in electronic structure calculations [108, 112]. Within the atomic sphere approximation (ASA), LMTO is a minimal and efficient basis set with one basis function per site I and quantum pair $L = (l, m)$. Although, the LMTO method is physically transparent the constructed basis is non-orthogonal.

Below we sketch the derivation of the bare and screened LMTO basis set within the ASA. The construction of the bare LMTOs $\chi_{IL}(\mathbf{r})$ starts with so called envelope function [112], which is a decaying solution of the Laplace equation centered at the site I:

$$K_L(\mathbf{r}_I) = K_l(r_I)Y_L(\hat{\mathbf{r}}_I) = \left(\frac{w}{r_I}\right)^{l+1} Y_L(\hat{\mathbf{r}}_I), \tag{4.2.2}$$

here $\mathbf{r}_I = \mathbf{r} - \mathbf{R}_I$, unit vector $\hat{\mathbf{r}}_I$ indicates the direction of $\mathbf{r}_I$, $Y_L(\hat{\mathbf{r}}_I)$ is a spherical function, and w is scaling parameter associated with the linear size of unit cell.

In any atomic sphere other than I, $K_L(\mathbf{r}_I)$ can be represented as:

$$K_L(\mathbf{r}_I) = -\sum_{L'} S_{IL,I'L'} J_{L'}(\mathbf{r}_{I'}). \tag{4.2.3}$$

The function $J_L(\mathbf{r}_I) = (r_I/w)^l Y_L(\hat{\mathbf{r}}_I)$ stands for the regular solutions of Laplace equation, and $S_{IL,I'L'}$ are structure constants.

Inside each atomic sphere we construct a linear combination of the solution $\phi_{IL}(\mathbf{r}_I)$ of Schrödinger equation and its first derivative with respect to energy $\dot{\phi}_{IL}(\mathbf{r}_I)$ at some fixed energy E_ν.

The final step is to smoothly match the boundary conditions at the surface of sphere I:

$$\Phi_L^H(\mathbf{r}_I) \equiv A_{IL}^K \phi_{IL}(\mathbf{r}_I) + B_{IL}^K \dot{\phi}_{IL}(\mathbf{r}_I) \rightarrow K_L(\mathbf{r}_I) \tag{4.2.4}$$

and at the surface of sphere I' for all $I' \neq I$:

$$\Phi_{L'}^J(\mathbf{r}_{I'}) \equiv A_{I'L'}^J \phi_{I'L'}(\mathbf{r}_{I'}) + B_{I'L'}^J \dot{\phi}_{I'L'}(\mathbf{r}_{I'}) \rightarrow J_{L'}(\mathbf{r}_{I'}). \tag{4.2.5}$$

With the array of constants A and B determined from 4.2.4 - 4.2.5 we conclude the construction of bare LMTO basis function:

$$\chi_{IL}(\mathbf{r}_I) = \begin{cases} \Phi_L^H(\mathbf{r}_I), & \mathbf{r}_I \in S_I, \\ -\sum_{L'} S_{IL,I'L'} \Phi_{L'}^J(\mathbf{r}_{I'}), & \mathbf{r}_{I'} \in S_{I'} (I \neq I'), \\ K_L(\mathbf{r}_I), & \mathbf{r} \in Interstitial. \end{cases} \tag{4.2.6}$$

The Fourier transform of the LMTOs with respect to $\mathbf{R}_I - \mathbf{R}_{I'}$ gives:

$$\chi_{\mathbf{k}L}(\mathbf{r}) = \begin{cases} \Phi_L^H(\mathbf{r}) - \sum_{L'} \Phi_{L'}^J(\mathbf{r}) S_{\mathbf{k}LL'}, & |\mathbf{r}| < R_{MT}, \\ \sum_{\mathbf{k}} e^{i\mathbf{k}\mathbf{R}} K_L(\mathbf{r} - \mathbf{R}), & |\mathbf{r}| > R_{MT}. \end{cases} \tag{4.2.7}$$

The standard LMTO method outlined above yields long-range orbitals. The concept of a screened LMTO was created to overcome the non-locality of the

bare LMTO basis set [109]. The method is based upon the idea of localizing the LMTOs by screening with multipoles added on the neighboring spheres. Namely, to each regular solution of Laplace equation we add $-\alpha_{IL}$ of the irregular solution:

$$J_L^\alpha(\mathbf{r}_I) = J_L(\mathbf{r}_I) - \alpha_{IL} K_L(\mathbf{r}_I). \tag{4.2.8}$$

The condition that the on-site Laplace solution should not change leads to the Dyson-like equation for the screened structure constants:

$$S^\alpha_{a,a'} = S_{a,a''}[\delta_{a''a'} + \alpha_{a''} S^\alpha_{a'',a'}] = S_{a,a''} U_{a'',a'}, \tag{4.2.9}$$

where matrix index a refers to the pair (I, L) and implies summation over repeated indices. The matrices $\alpha_a \equiv \alpha_l$ are diagonal for each l. In our calculations the choice of α's was as follows: $\alpha_s = 5.5166$, $\alpha_p = 0.5242$, $\alpha_d = 0.1382$ and $\alpha_f = 0.0355$.

The screened and bare envelope functions are related by the transformation $U_{a',a}$ introduced in 4.2.9:

$$K_L^\alpha(\mathbf{r}_I) = \sum_{I'L'} K_{L'}(\mathbf{r}_{I'})[\delta_{I'L',IL} + \alpha_{I'L'} S^\alpha_{I'L'IL}], \tag{4.2.10}$$

Or in matrix notations:

$$K^\alpha_a = K_{a'} U_{a',a},$$

where $K_a \equiv K_L(\mathbf{r}_I)$ and $K^\alpha_a \equiv K^\alpha_L(\mathbf{r}_I)$.

With the definitions 4.2.8, 4.2.9 and 4.2.10 the construction of screened LMTOs proceeds exactly in the same way as in the case of the bare LMTOs. Namely, we construct new linear combinations

$$\Phi^{H\alpha}_L(\mathbf{r}_I) \equiv A^{K\alpha}_{IL} \phi_{IL}(\mathbf{r}_I) + B^{K\alpha}_{IL} \dot{\phi}_{IL}(\mathbf{r}_I)$$

inside the sphere I by matching smoothly $K^\alpha_L(\mathbf{r}_I)$ on its surface. Also, we construct new linear combination

$$\Phi^{J\alpha}_{L'}(\mathbf{r}_{I'}) \equiv A^{J\alpha}_{I'L'} \phi_{I'L'}(\mathbf{r}_{I'}) + B^{J\alpha}_{I'L'} \dot{\phi}_{I'L'}(\mathbf{r}_{I'})$$

inside sphere I' by matching smoothly $J^{\alpha}_{L'}(\mathbf{r}_{I'})$ on its surface for each $I' \neq I$. Thus, we arrive to the definition of screened LMTO:

$$\chi^{\alpha}_{IL}(\mathbf{r}_I) = \begin{cases} \Phi^{H\alpha}_L(\mathbf{r}_I), & \mathbf{r}_I \in S_I, \\ -\sum_{L'} S^{\alpha}_{IL,I'L'} \Phi^{J\alpha}_{L'}(\mathbf{r}_{I'}), & \mathbf{r}_{I'} \in S_{I'} (I \neq I'), \\ K^{\alpha}_L(\mathbf{r}_I), & \mathbf{r} \in Interstitial. \end{cases} \tag{4.2.11}$$

The Fourier transform of screened LMTOs with respect to $\mathbf{R}_I - \mathbf{R}_{I'}$ gives:

$$\chi^{\alpha}_{\mathbf{k}L}(\mathbf{r}) = \begin{cases} \Phi^{H\alpha}_L(\mathbf{r}) - \sum_{L'} \Phi^{J\alpha}_{L'}(\mathbf{r}) S^{\alpha}_{\mathbf{k}LL'}, & |\mathbf{r}| < R_{MT}, \\ \sum_{\mathbf{k}} e^{i\mathbf{k}\mathbf{R}} K^{\alpha}_L(\mathbf{r} - \mathbf{R}), & |\mathbf{r}| > R_{MT}. \end{cases} \tag{4.2.12}$$

The Hamiltonian and overlap matrices in screened and bare LMTO representations (O , H, and O^{α}, H^{α} respectively) are related through the transformation U introduced in 4.2.9:

$$H^{\alpha} = U^{\dagger} H U \tag{4.2.13}$$

$$O^{\alpha} = U^{\dagger} O U. \tag{4.2.14}$$

Have constructed the basis, one has to solve the generalized eigenvalue problem:

$$(H(\mathbf{k}) - \epsilon_i(\mathbf{k}) O(\mathbf{k})) \psi_i(\mathbf{k}) = 0. \tag{4.2.15}$$

As described above, it is necessary to transform to an orthogonal basis when performing many-body calculations, such as DMFT, in order to avoid the difficulties associated with a non-orthogonal basis.

4.2.3 Löwdin orthogonalization

Löwdin orthogonalization [110] is a straightforward orthogonalization of the Hamiltonian which uses no information from the basis set:

$$\tilde{\mathcal{H}}(\mathbf{k}) = \frac{1}{\sqrt{O^{\dagger}(\mathbf{k})}} \mathcal{H}(\mathbf{k}) \frac{1}{\sqrt{O(\mathbf{k})}}. \tag{4.2.16}$$

As will be shown below, this orthogonalization procedure may lead to a further mixing of L characters among the LMTOs and hence unphysical results.

4.2.4 Projective orthogonalization

A physically guided, orthogonalization procedure is to find a basis where each function contains the maximum amount of a particular L character. This approach proposed by K. Haule was used in earlier LDA+DMFT studies of cerium and plutonium [111]. This basis has an important advantage. The "f electron" in this basis has mostly f character. Mathematically, the non-interacting spectral function of f electron Green's function in this basis agrees with the LDA f density of states. This allowed us to identify the f occupation in this basis set with the occupation numbers inferred from EELS and X-Ray absorption which are sensitive to angular momentum selection rules [113, 114, 115].

Here we follow [111]. It is straightforward using 4.2.7 and 4.2.14 to show that overlapping matrix within MT-sphere can be represented as [116]:

$$O_{\mathbf{k}L_1L_2} = \delta_{L_1L_2} o_{l_1}^{(HH)} - S^{\dagger}_{\mathbf{k}L_1L_2} o_{l_2}^{(JH)} - o_{l_1}^{(HJ)} S_{\mathbf{k}L_1L_2} + S^{\dagger}_{\mathbf{k}L_1L'} o_{l'}^{(JJ)} S_{\mathbf{k}L'L_2}. \tag{4.2.17}$$

The quantities o_l^{HH}, o_l^{JH}, o_l^{HJ} and o_l^{JJ} are numbers in each l-subspace. For A and B representing H or J:

$$o_{l_1}^{AB} = \langle \Phi_{L_1}^{A} | \Phi_{L_2}^{B} \rangle \delta_{L_1L_2}, \tag{4.2.18}$$

In each L-subspace the overlapping matrix is:

$$O_{\mathbf{k}} = o^{(HH)} - S^{\dagger}_{\mathbf{k}} o^{(JH)} - o^{(HJ)} S_{\mathbf{k}} + S^{\dagger}_{\mathbf{k}} o^{(JJ)} S_{\mathbf{k}}. \tag{4.2.19}$$

In order to find the transform to the orthonormal base we must represent $O(\mathbf{k})$ as the square of a matrix. As we show below, the most intelligent choice would be:

$$O(\mathbf{k}) \approx (\mathcal{H} - \mathcal{J} S_{\mathbf{k}})^{\dagger} (\mathcal{H} - \mathcal{J} S_{\mathbf{k}}) \tag{4.2.20}$$

for each L-subspace. Here $\mathcal{H}$ and $\mathcal{J}$ are diagonal matrixes proportional to unity in each subspace of definite L just like the overlaps $o^{(HH)}$ defined above.

The above equation cannot be made exact, because overlap numbers are obtained by integration over the radial part of wave functions. However, in most cases the overlap numbers can become very close to their approximations:

$$\begin{aligned} o_l^{(HH)} &\approx \mathcal{H}_l^* \mathcal{H}_l, \\ o_l^{(JH)} &\approx \mathcal{J}_l^* \mathcal{H}_l, \\ o_l^{(HJ)} &\approx \mathcal{H}_l^* \mathcal{J}_l, \\ o_l^{(JJ)} &\approx \mathcal{J}_l^* \mathcal{J}_l. \end{aligned} \tag{4.2.21}$$

For each L we have three independent equations for two unknowns. An approximate solution can be found by minimizing the following function:

$$\begin{aligned} |o_l^{(HH)} - \mathcal{H}_l^* \mathcal{H}_l|^2 + |o_l^{(JH)} - \mathcal{J}_l^* \mathcal{H}_l|^2 \\ + |o_l^{(HJ)} - \mathcal{H}_l^* \mathcal{J}_l|^2 + |o_l^{(JJ)} - \mathcal{J}_l^* \mathcal{J}_l|^2 = min. \end{aligned} \tag{4.2.22}$$

The desired transformation to the new base is:

$$T_{\mathbf{k}} = (\mathcal{H} - \mathcal{J} S_{\mathbf{k}})^{-1}. \tag{4.2.23}$$

Finally:

$$\begin{aligned} O_{\mathbf{k}}^{new} &= T_{\mathbf{k}}^{\dagger} O_{\mathbf{k}} T_{\mathbf{k}} \approx 1, \\ H_{\mathbf{k}}^{new} &= T_{\mathbf{k}}^{\dagger} H_{\mathbf{k}} T_{\mathbf{k}}. \end{aligned} \tag{4.2.24}$$

4.2.5 Slicing

In order to determine the optimum basis, we need to define a criteria to judge the different bases. When performing DMFT calculations, one accounts only for a subset of local electronic correlations (those on the f orbital). Therefore, from the perspective of DMFT it is best to have f orbitals with the largest on-site Coulomb repulsion U [117, 118]. A simpler criteria, in the same spirit, is to

search for the smallest value of t^f. The different terms in Hamiltonian 4.1.1 can be easily identified at each **k**-point of the Brillouin zone:

$$H(\mathbf{k}) = \begin{pmatrix} H_{spd}(\mathbf{k}) & V_{\mathbf{k}} \\ V_{\mathbf{k}}^{\dagger} & H_f(\mathbf{k}) \end{pmatrix} \tag{4.2.25}$$

The hybridization V in the Hamiltonian (4.1.1) may be set to zero. What remains are the two blocks H_f and H_{spd} of (4.2.25) which are now completely decoupled. The Hamiltonian may now be diagonalized resulting in distinct *spd* and f bands, and any dispersion of the f bands is due to t^f.

4.2.6 Technical note

The procedure of extraction of Hamiltonian in the representation of four basis sets listed in Table 4.3 is schematically shown in Figure 4.2. The starting point of the analysis, namely Hamiltonian and overlap matrix in either bare or screened LMTO basis are printed to files *ham.dat* and *olp.dat* by the exporting version of LMTART code. The detailed description of LMTART code's input, output files and run modes can be found in [37] and as online material of review [20]. The switch "Bare/Screened" LMTO is set in <CNTRLS> section of INI-file.

The Löwdin orthogonalization was implemented through python script which takes as input files with Hamiltonian, overlap matrix and list of **k**-points of Brillouin zone.

The projective orthogonalization is implemented by K. Haule in KSUM code. The detailed description of input files and run modes can be found in online material for [20]. To perform only projective transformation zero self-energy stored in file sig.inp has been used. Also all orbitals in *cix.dat* file must be identified as correlated in order to have transformation to be applied to all orbitals.

After orthogonalization of the Hamiltonian we proceed with slicing procedure described in previous subsection and comparison of band structure of H_f and

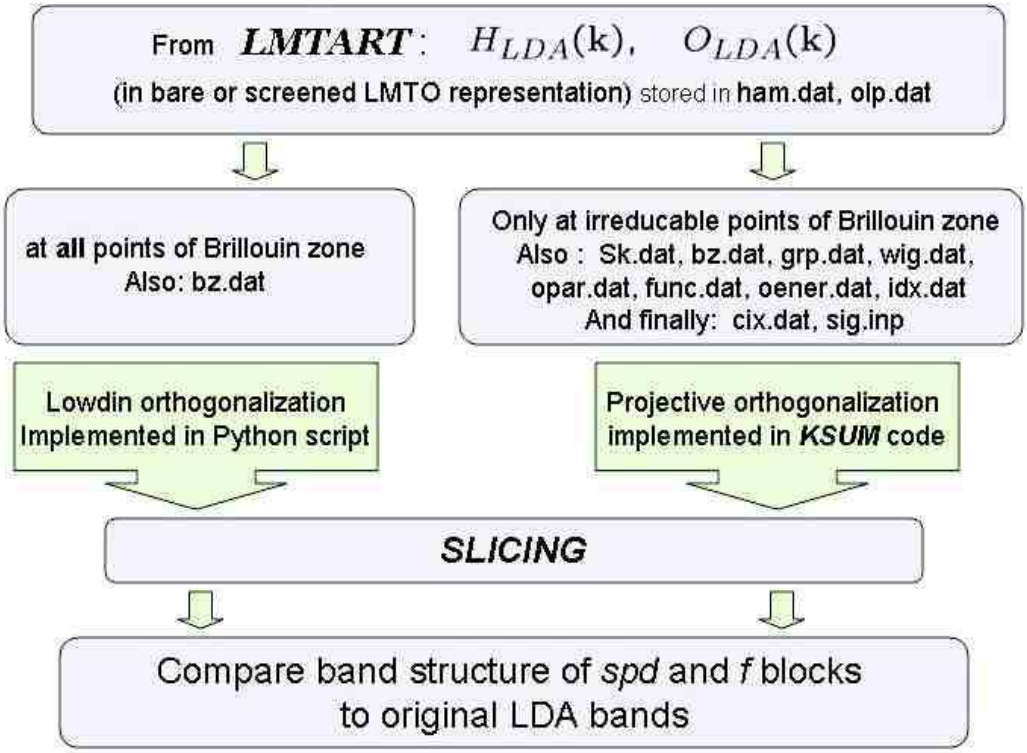

Figure 4.2: Procedure.

H_{spd} with original spd bands.

4.3 Results

4.3.1 Starting point: self-consistent LDA calculations.

We performed relativistic, spin-restricted LDA calculations within the ASA scheme. $7s$, $6p$, $6d$ and $5f$-orbitals were chosen to represent valent states, and 10^3 **k**-points were used for the integration over first Brillouin zone. The same type of calculations were carried out for 4 different materials, picked to evenly represent actinide series: U, α-Pu, δ-Pu and Cm II (fcc phase of curium). For simplicity, we used the fcc crystal structure for each element. The lattice parameters listed in Table 4.4 were chosen to match the experimentally measured volumes

for corresponding phases in case of Pu and Cm II. For U we use the equilibrium volume predicted within GGA calculations. The Brillouin zone of fcc structure with major high symmetry directions is shown in Figure 4.3.

Table 4.4: Lattice parameters (in angstroms).

α-U	4.3378
α-Pu	4.3074
δ-Pu	4.6400
Cm II	4.9726

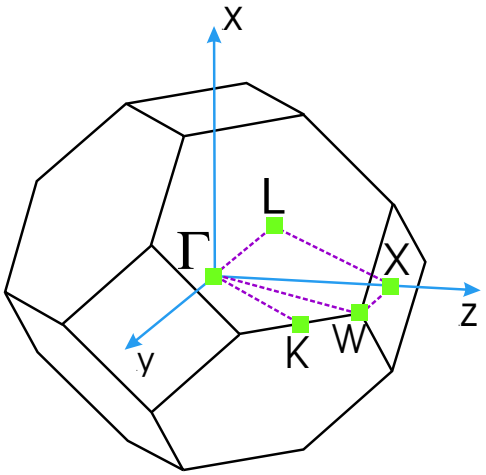

Figure 4.3: Brillouin zone of fcc structure with indicated high symmetry directions.

In Figure 4.4 we present LDA band structure of Cm II with indicated contributions of $5f$- and $6d$- characters. The overwhelming domination of f characters within 1eV window around Fermi level forces the conclusion that the low-energy physics of actinides is completely controlled by $f-f$ bonding. As we show below this intuitive interpretation turns out to be mistaken and Hubbard model alone can not be considered as ground state Hamiltonian for actinides. One has to account for presence of spd-characters at the Fermi level trough the hybridization. Moreover, the hybridization energy scale in actinides turns out to be larger than the average $f-f$ hopping.

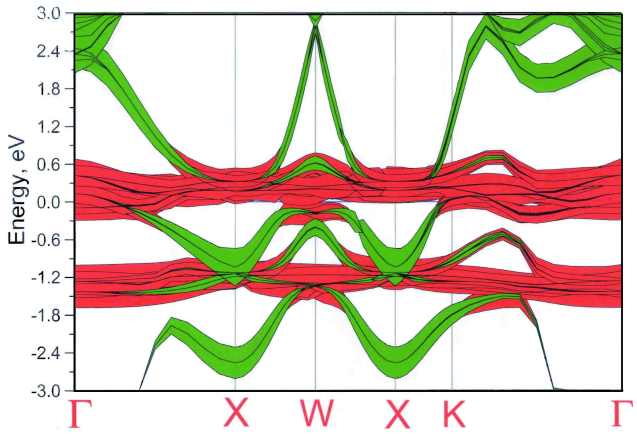

Figure 4.4: Band structure of Cm with indicated contribution of $5f$ (red) and $6d$ (green) characters. The layout is chosen to show d-contributions over f-contribution.

4.3.2 Determining a robust basis for the actinides

We begin by analyzing the bare LMTOs orthogonalized with the Löwdin procedure (see top left panel Figure 4.5). Some f bands have a dispersion greater than 1.5 eV which is unfavorable. Using the bare LMTOs orthogonalized with the projective procedure, the f bands are far more narrow with a width of less than 0.4 eV (see left bottom panel of Figure 4.5). In this case the two sets of bands can be identified as $S = \frac{7}{2}$ and $S = \frac{5}{2}$. The Löwdin orthogonalization mixes the *spd* states into the f states which causes a larger dispersion and a mixing of f bands between the $S = \frac{7}{2}$ and $S = \frac{5}{2}$ states. Alternatively, the projective orthogonalization minimizes the amount of *spd* character in the f states which results in weakly dispersing f states.

The same exercise can be performed using the screened LMTOs (see right top and bottom panels of Figure 4.5). In this case, both the Löwdin and the projective orthogonalization produce nearly identical results to the projective orthogonalization of the bare LMTOs. The screened LMTOs are insensitive to the method of orthogonalization due to the fact that orbitals are already well localized with a well-defined character. In conclusion, one may use bare LMTOs

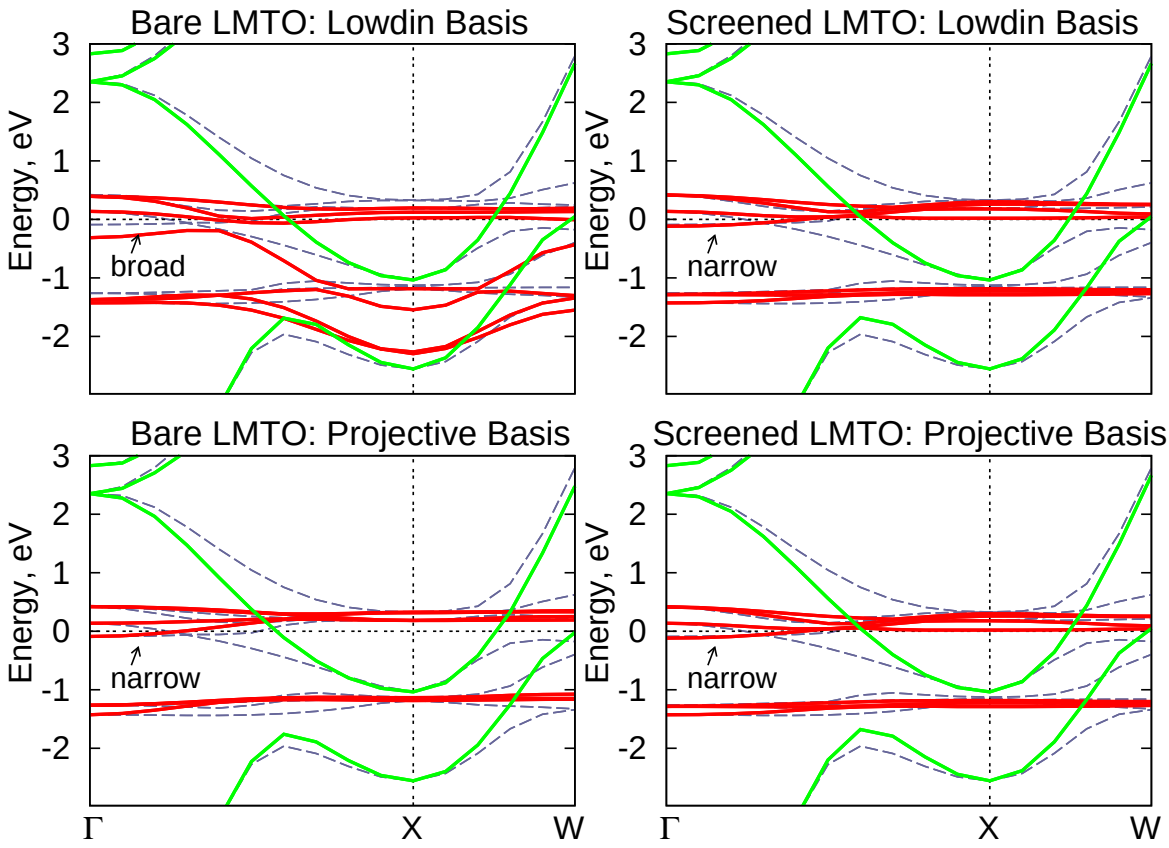

Figure 4.5: Basis difference for fcc Curium. In all panels dashed grey line represent band structure produced by whole hamiltonian, solid green line - by *spd* block, and solid red line - by f block. Both Löwdin and projective orthogonalization result in the same band structure while applied to Hamiltonian in screened LMTO representation. In the case of bare LMTOs the major difference between Löwdin and projective orthogonalization occurs within f bands (solid red lines). Finally, it should be noticed that projective orthogonalization is basis independent and provides the same band structure for Hamiltonian in both bare and screened LMTO representations.

orthogonalized with the projective procedure or screened LMTOs orthogonalized in an arbitrary manner as a robust basis for the actinides.

The major contribution among *spd*-orbital to mixing with and expanding f bands comes from s-characters. Indeed, Löwdin and projective orthogonalization differ by terms containing containing structure constants, which are in turn proportional to o^{JJ}, o^{JH} and o^{HJ}. In case of Cm the overlap numbers are shown in Table 4.5.

In case of bare LMTO, s-orbitals are very long-range and have $o^{JJ} \approx 115$.

Table 4.5: Overlap numbers for Cm II.

	s	p	d	f
Bare LMTO				
o^{HH}	(2.27124,0.000)	(9.16427,0.000)	(35.40434,0.000)	(907.78568,0.000)
o^{HJ}	(15.85822,0.000)	(7.91339,0.000)	(6.97400,0.000)	(-41.06287,0.000)
o^{JH}	(15.85822,0.000)	(7.91339,0.000)	(6.97400,0.000)	(-41.06287,0.000)
o^{JJ}	(115.09151,0.000)	(7.64477,0.000)	(2.18279,0.000)	(3.04675,0.000)
Screened LMTO				
o^{HH}	(2.26435,0.000)	(171.31688,0.000)	(34.70583,0.000)	(836.94498,0.000)
o^{HJ}	(3.31761,0.000)	(-4.83644,0.000)	(2.15627,0.000)	(-70.61786,0.000)
o^{JH}	(3.31761,0.000)	(-4.83644,0.000)	(2.15627,0.000)	(-70.61786,0.000)
o^{JJ}	(9.23412,0.000)	(2.36841,0.000)	(0.92777,0.000)	(7.17800,0.000)

While in the projective orthogonalization these fat tails of s-orbitals are accurately subtracted in Löwdin transformation they are mix in f-characters. To justify this point we performed projective orthogonalization with o^{JJ}, o^{JH} and o^{HJ} forced to be zeros. This condition makes transformation 4.2.23 to be $T = \mathcal{H}$ and formally concise with Löwdin transformation. The band structure resulted from this calculation is compared to band structure resulted from Löwdin transformation in Figure 4.6. The shape of $5f$-bands are almost identical confirming that without subtraction of tails of s-orbital wave function these characters mix into $5f$ orbitals resulting in artificial broadening of later.

4.3.3 Decomposition of the actinide band structures

Having established a sensible basis for the actinides we choose to proceed with projective orthogonalization of bare LMTOs. It is instructive to zero the hybridization V of the Hamiltonian for U, α-Pu, δ-Pu, and Cm, and to compare the full band structure with the *spd* and f bands (see Figures 4.7 and 4.8). The same generic behavior can be seen in all four systems. The *spd* bands have a strong dispersion and cross the Fermi energy in all cases, and the f bands are relatively

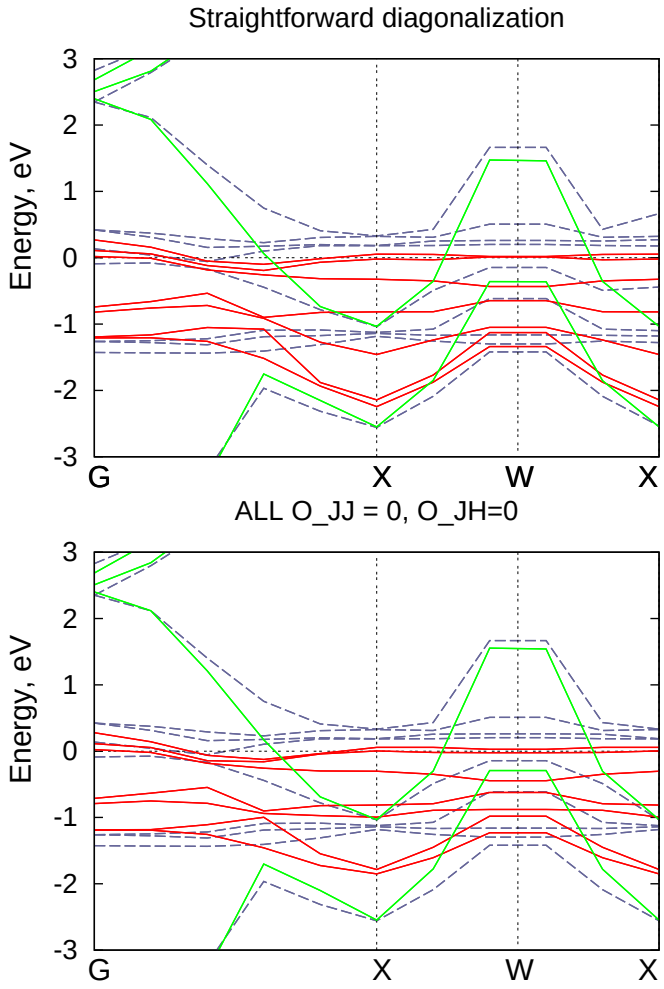

Figure 4.6: Sliced band structures obtained trough Löwdin transformation is compared to band structures obtained through projective orthogonalization when in later all terms proportional to structure constants are forced to be zeros.

narrow. The fact that the *spd* bands cross the Fermi energy in all cases is a critical point which indicates that there will be *spd* states at the Fermi energy even if the f states become completely localized. When the hybridization V is switched on, the f and *spd* bands interact via V and mix. Therefore the strength of V can qualitatively be seen as the difference between the full DFT bands and the f+*spd* bands. The *spd* bands change relatively little across the actinides, with the values at the Γ point being nearly independent of atomic number. Alternatively, the f bands are relatively wide for uranium and become increasingly narrow as curium is approached. The relative values of V and t^f will be quantified below.

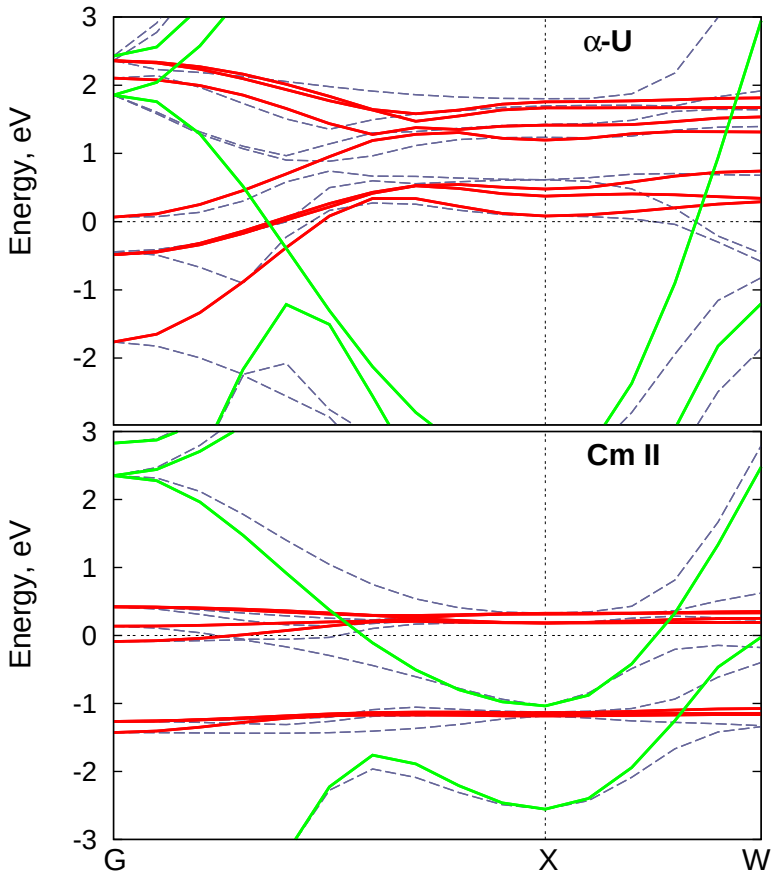

Figure 4.7: Band structure of α-U (top) and Cm II (bottom). Grey dashed lines represent LDA bands, green lines represent bands of H_{spd}, and red lines represent bands of H_f

4.3.4 Quantitative analysis of V and t^f.

In order to quantify V and t^f for the different actinides, we introduce an average V and t^f so each actinide may be characterized by two numbers.

First, we remind that the Hamiltonian 4.1.1 is consist of four blocks:

$$H(\mathbf{k}) = \begin{pmatrix} H^{spd}(\mathbf{k}) & V_{\mathbf{k}} \\ V_{\mathbf{k}}^{\dagger} & H^{f}(\mathbf{k}) \end{pmatrix} \tag{4.3.26}$$

Then the average strength of hybridization per band is defined as follows:

$$\overline{V} = \frac{1}{N_f}[\frac{1}{2} Tr\langle \tilde{H}(\mathbf{k})\tilde{H}(\mathbf{k})\rangle]^{1/2}, \tag{4.3.27}$$

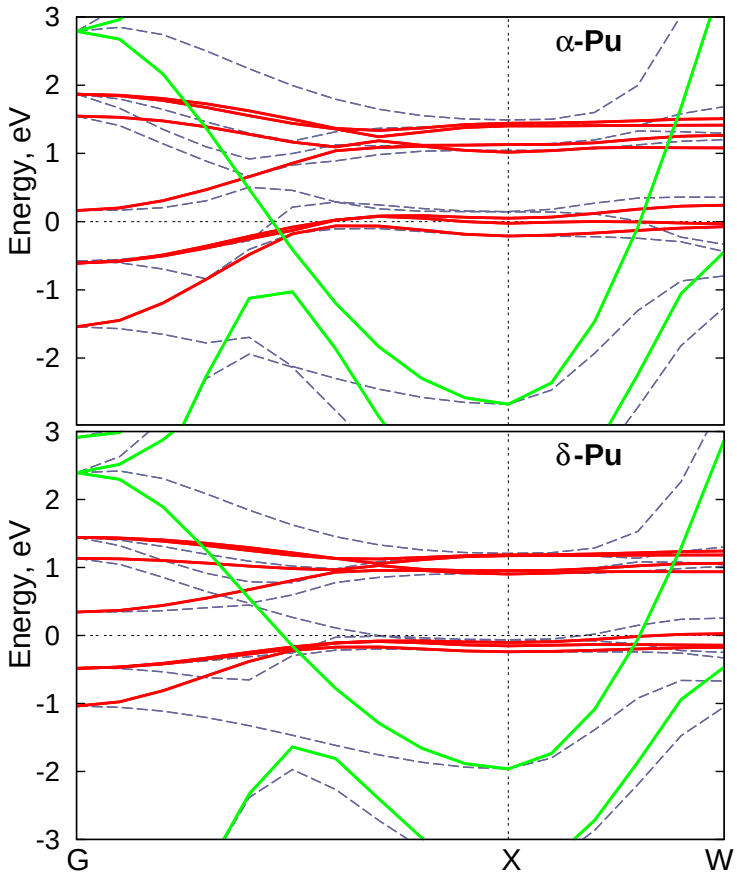

Figure 4.8: Band structure of α-Pu (top) and δ-Pu(bottom). Grey dashed lines represent LDA bands, green lines represent bands of H_{spd}, and red lines represent bands of H_f

where $\tilde{H}(\mathbf{k})$ stands for hamiltonian 4.3.26 with $H_{spd}(\mathbf{k}) = H_f(\mathbf{k}) = 0$ and $N_f = 14$ stands for number of f-bands. The definition 4.3.27 was chosen to match hybridization V of standard Anderson model in two-band limit.

The average value of t^f is defined as follows:

$$\overline{t^f} = \frac{1}{N_f}[Tr(\langle H_f(\mathbf{k})^2\rangle - \langle H_f(\mathbf{k})\rangle^2)]^{1/2}, \tag{4.3.28}$$

and matches t^f of canonical Hubbard model in the limit of one-band model. In the above expressions 4.3.27 and 4.3.28 the brackets mean the following: $\langle \ldots \rangle = \frac{1}{N_\mathbf{k}} \sum_\mathbf{k} \ldots$

Table 4.6: Quantitative characteristics for actinide series (in eV).

	$\overline{V}$	$\overline{t^f}$	$\overline{V}/\overline{t^f}$	$\epsilon_{5/2}-\mu$	$\epsilon_{7/2}-\mu$
Bare LMTO					
α-U	0.483	0.188	2.569	0.442	1.353
α-Pu	0.423	0.146	2.897	-0.180	0.971
δ-Pu	0.305	0.099	3.081	-0.129	1.008
Cm II	0.189	0.050	3.780	-1.152	0.238
Screened LMTO					
α-U	0.490	0.188	2.606	0.444	1.355
α-Pu	0.429	0.146	2.938	-0.178	0.973
δ-Pu	0.309	0.098	3.153	-0.128	1.009
Cm II	0.192	0.050	3.840	-1.151	0.238

Table 4.6 lists calculated values of the average hybridization $\overline{V}$ and $\overline{t^f}$ and the average energy level for $j = 5/2$ and $j = 7/2$ of f manifold relative to the Fermi energy. The $\overline{t^f}$ are generally the same for bare and screened LMTOs, with the exception of the average hybridization being slightly larger in the case of screened LMTOs.

These results are displayed graphically in Figure 5.7. The blue bars represent average hybridization, while red bars represent average strength of $f-f$ hoppings. In all cases, $\overline{V}$ is significantly greater than $\overline{t^f}$. As one moves along actinides series from U to Cm $\overline{t^f}$ decreases as much as four times. The average value of hybridization $\overline{V}$ also decreases but at a slower rate, as indicated by the inset plot of the ratio of $\overline{V}$ and $\overline{t^f}$. The strong decrease in $\overline{V}$ and $\overline{t^f}$ will both contribute to the localization of the f states. In order to determine if the localization could be predominantly assigned to either Mott or Anderson character, explicit many-body calculations such as DMFT would need to be performed.

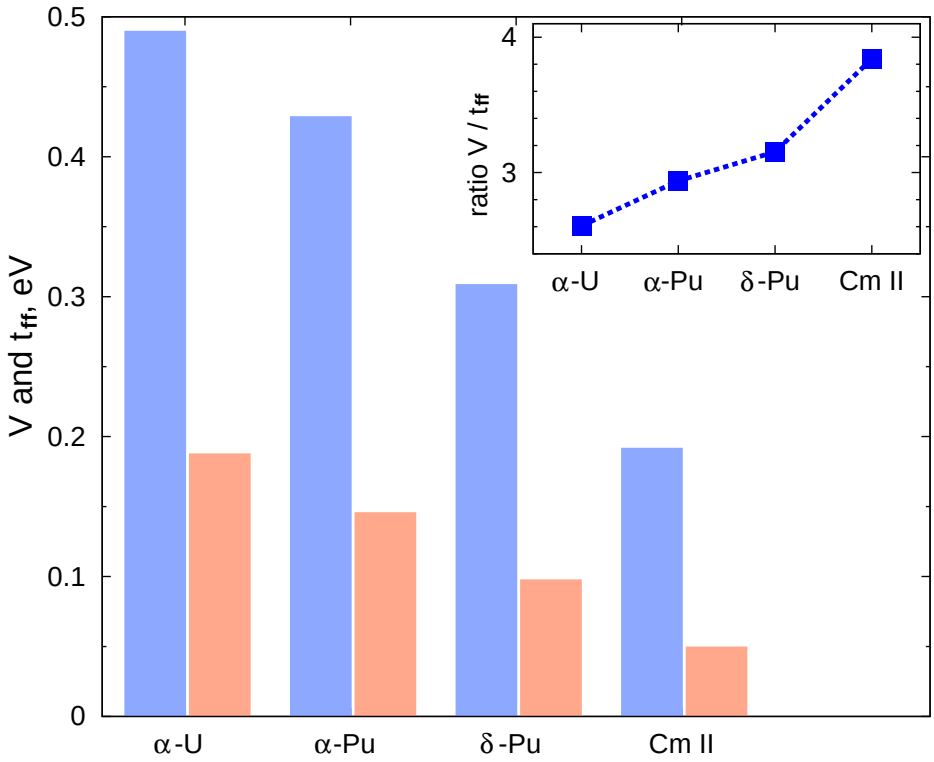

Figure 4.9: Histogram represents average hybridization (blue bars) and average $f-f$ hopping (red bars) as functions of atomic number along actinide series. In inset: the ratio $\overline{V}/\overline{t^f}$ (squares) as function of atomic number.

4.4 Conclusion

In summary, a one-electron analysis of band structure of the actinides was presented. We demonstrated that bare LMTOs orthogonalized with the projective method and screened LMTOs are robust bases, in the sense that they give rise to f orbitals with minimal hopping. Analysis of the Hamiltonian in these bases yielded a number of interesting results. When switching off the hybridization V, it was shown that the *spd* states cross the Fermi energy and hence will be present at the Fermi energy even if the f electrons become localized.

Evaluation of the average hybridization $\overline{V}$ and average $f-f$ hopping $\overline{t^f}$ as a function of the actinides showed that both quantities decrease strongly. The quantity $\overline{t^f}$ decreased faster than $\overline{V}$ and $\overline{V}$ was larger in all actinides. Hence, the Anderson model of the localization-delocalization transition, rather than a

multiorbital Hubbard model is needed to describe the physics of the actinides once explicit many-body calculations are added. This is the point of view taken in recent DMFT work [98], and no further reduction to a model containing only f bands seems possible.

Chapter 5
Real space analysis for actinides

In this chapter we report a detailed real space analysis for actinides. After an introduction and motivation in Section 5.1, we develop and describe tools to probe the locality of $5f$-orbitals in these materials in Section 5.2. Then in Section 5.3 the results of real space analysis are reported. We demonstrate that $5f$ orbitals are very local and only first nearest neighbors are required to reproduce band structure within f-block. Also, we provide a tight-binding (TB) parametrization of the low-energy Hamiltonian, and finally compare parametrization to the earlier reported in literature in Section 5.4.

5.1 Introduction and motivations

The tight-binding (TB) formulation plays an important role in electronic structure. Of all methods, perhaps tight-binding provides the simplest understanding of the fundamental features of electronic bands. Particularly, an empirical tight-binding parametrization can provide accurate, useful descriptions of electronic bands and total energies. In this approach, given few tight-binding parameters one assumes a form for the Hamiltonian and overlap matrix elements without actually specifying anything about the orbitals except their symmetry [16]. The values of the matrix elements may be derived approximately or maybe fitted to the experiment or other theory. Here we derive tight-binding parameters for actinides from LSDA-calculations given in the previous chapter.

The earlier attempts to construct tight-binding parametrization for actinides

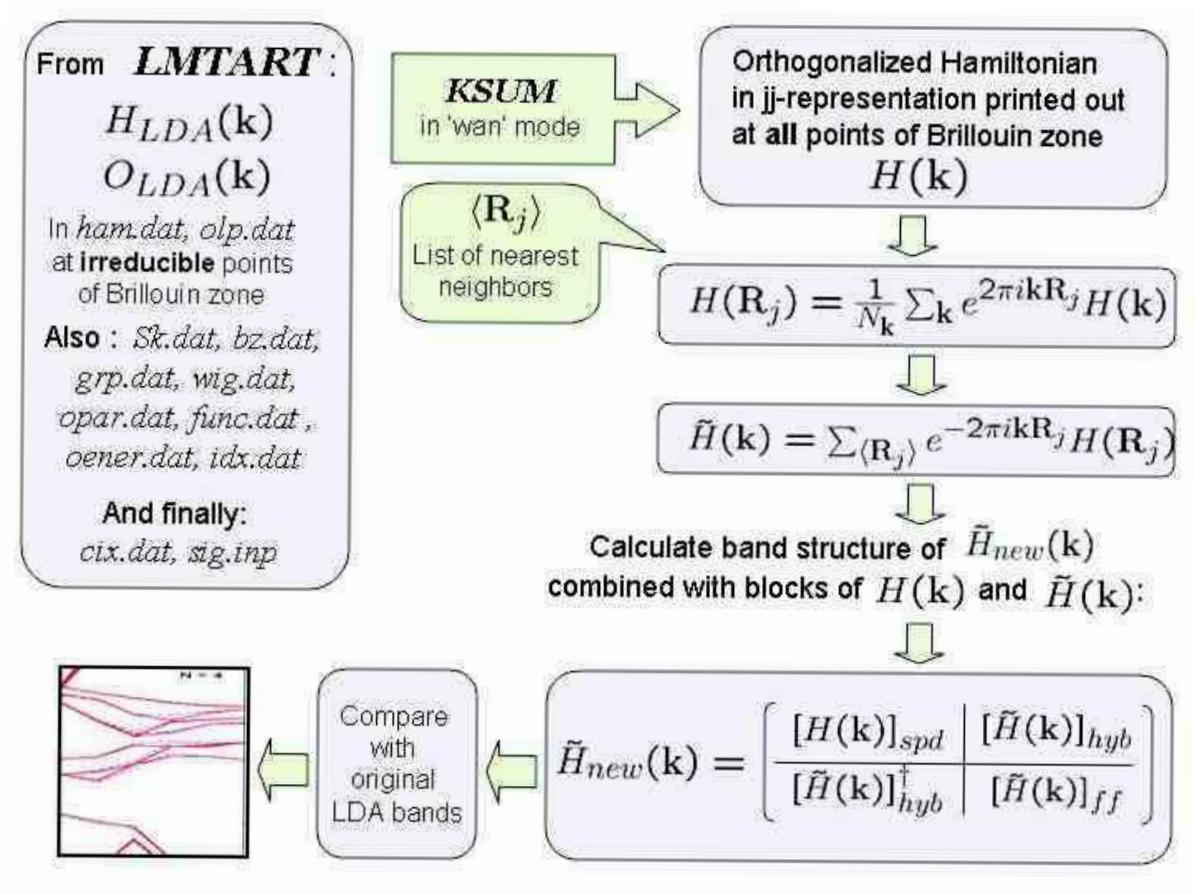

Figure 5.1: Diagram shows the sequence of steps completed in tight-binding analysis.

resulted in two limited models. The first provided parametrization of f-bands only with spin-orbit coupling incorporated trough intra-atomic matrix elements [99]. The other considered hybridization of f-orbitals with *spd*-orbitals but ignored spin-orbit coupling [100].

5.2 The tools of analysis

The idea of reported analysis is to probe the locality of $5f$ orbitals observing how well bands constructed with specified number of nearest neighbors fit the original LSDA bands.

In the Figure 5.1 we show sequence of steps that were performed. The main

two steps are:

$$H_{LSDA}(\mathbf{k}) \longrightarrow H(\langle \mathbf{R}_i \rangle) \longrightarrow \tilde{H}(\mathbf{k}). \tag{5.2.1}$$

Here $\langle \mathbf{R}_i \rangle$ indicate nearest neighbors. First, we Fourier transform $H_{LSDA}(\mathbf{k})$ to real space using a given number of nearest neighbors, and then transform back to **k**-space and observe changes in the band structure. If one would use all atoms of the sample for the discrete Fourier transform then LSDA band structure must be reproduced perfectly. On the other side if we include a list of first nearest neighbors the obtained band structure might differ significantly from the original LSDA bands if $5f$-orbitals are not localized enough.

The starting point of the performed tight-binding analysis as shown in Figure 5.2 is the output of LMTART code in the basis of screened LMTO. Namely, files with the Hamiltonian, overlapping matrix and information about Brillouin zone are required (the details were given in the previous chapter). Files *ham.dat* and *olp.dat* contain the Hamiltonian and overlapping matrix only at irreducible points of Brillouin zone.

In order to print out orthogonalized Hamiltonian at all **k**-points in jj-representation we run KSUM code in the mode:

./ksum -mod wan+j -sig sig.inp -pn Cm -mu 6.9

where one has to use correct value for chemical potential. In the input file *cix.dat* all orbitals must be indicated as correlated, then all of them will be transformed into the jj-base. The *sig.inp* file contains zero self-energy.

Once the orthogonalized Hamiltonian is available we proceed by forming a list of given order N of nearest neighbors and their coordinates. Thus list of order $N = 0$ will consist of site itself only. The list of order $N = 1$ will consist of site itself and 12 first nearest neighbors in fcc structure. In Figure 5.2 up to fourth nearest neighbors are indicated in different colors.

To construct a tight-binding Hamiltonian we perform a Fourier transform to the real space and back. Since we know that *spd*-orbitals are itinerant we use

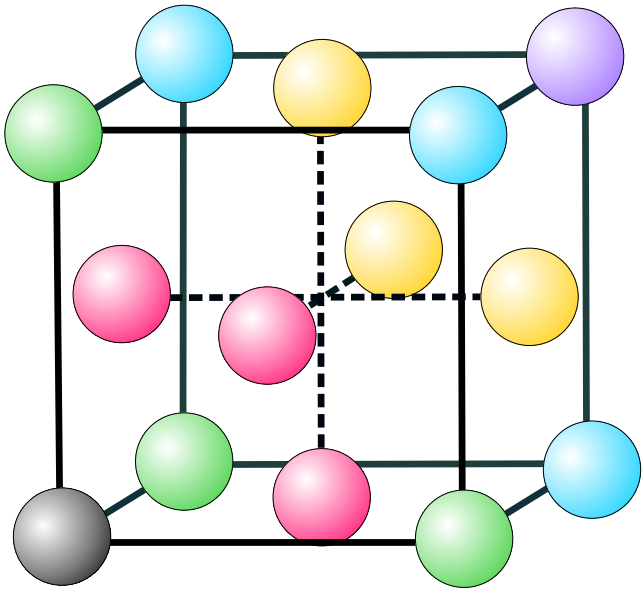

Figure 5.2: The nearest neighbors in fcc structure. The center atom (grey) is located in the origin. First nearest neighbors are filled with red, second – with green, third – with yellow, and fourth – with blue.

spd-block of H_{LSDA} instead of *spd*-block of $H(\mathbf{k})$. The final step is to compare the band structure of new constructed Hamiltonian to the original LDA bands.

5.3 Results

The result of real space analysis procedure described in Section 5.2 for Cm is shown in Figure 5.3. Here we compare three cases: on-site for $5f$-electrons band structure ($N = 0$), when only nearest neighbors are included ($N = 1$), and four nearest neighbors are included($N = 4$). The red solid lines represent bands of Fourier transformed Hamiltonian, while dashed grey lines are original LSDA bands. When one accounts only for on-site $5f$-orbitals, the band structure consist of flat lines representing on-site energies of $5f$-electrons and bands of *spd*-block. Strictly speaking, since the projective orthogonalization is only approximate there are non-zero off-diagonal elements in the Hamiltonian's hybridization block, but we checked that they are irrelevant and do not change band structure in any noticeable way. The LDA band structure is already reproduced almost perfectly

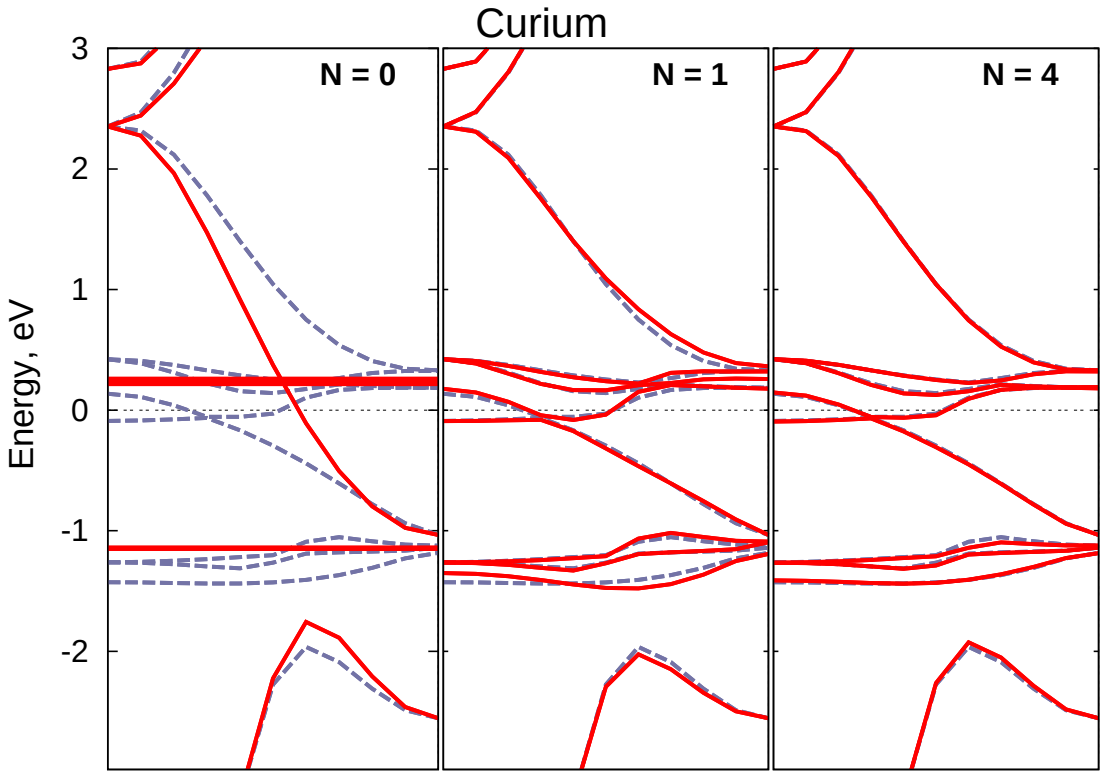

Figure 5.3: Band structure of Curium when N nearest neighbors are taken into account for f-orbitals (red solid line) is compared to original LDA bands (dashed grey line). The band structures are plotted for Γ-X direction.

when one takes into consideration the nearest neighbors. This confirms that $5f$-orbitals are very local and extended barely enough to form the bands. Bands of transformed Hamiltonian match LDA band structure exactly when four nearest neighbors are included. The only noticeable discrepancy is located approximately 1.0 eV below the Fermi energy. This long-range feature exists due to the long broad tails of the s-orbitals.

The corresponding tight-binding parametrization including only first nearest neighbors for Cm in jj-representation is given in Tables 5.1 and 5.2 in meV. This parametrization is obtained for the central atom to be at the origin and the nearest neighbor to be at position (1/2,0,1/2) in Cartesian coordinates. The

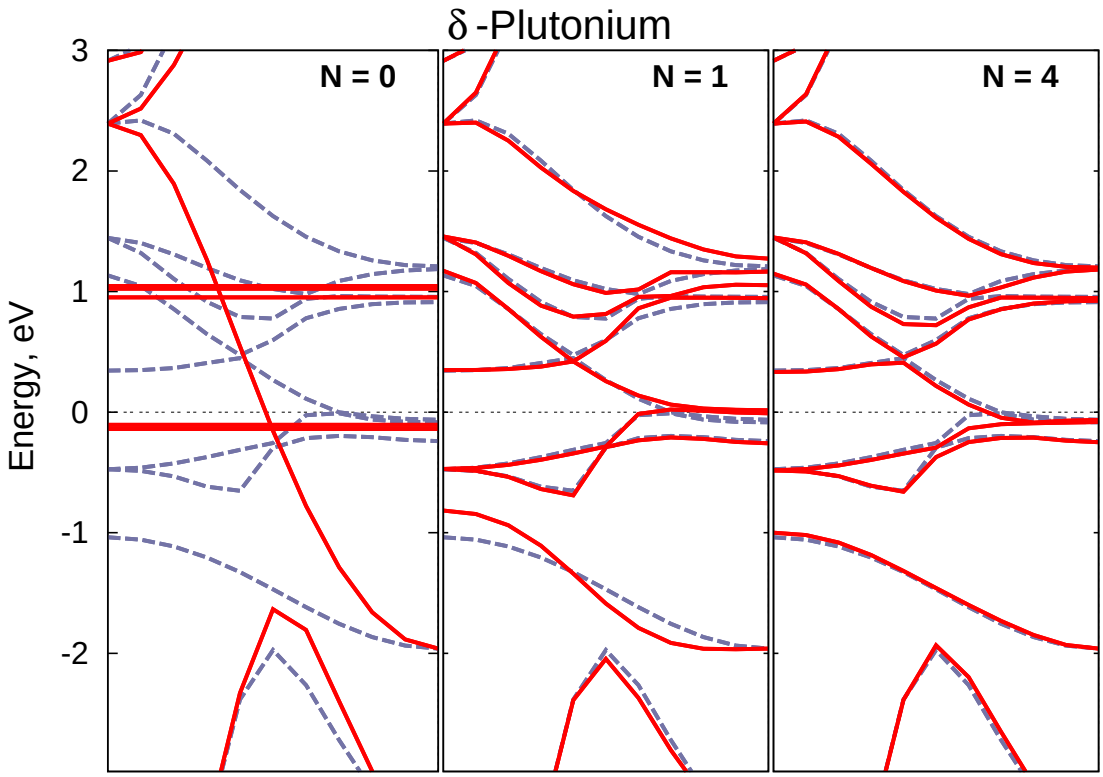

Figure 5.4: Band structure of δ-Pu when N nearest neighbors are taken into account for f-orbitals (red solid line) is compared to original LDA bands (dashed grey line). The band structures are plotted for Γ-X direction.

parametrization for the other nearest neighbors can be obtained by transformation $O^T HO$, where H is given in Tables 5.1 and 5.2 matrix, and O is matrix describing transformation of $5f$ orbitals under given spatial rotation. The energy scale of $\sim$1 eV of spin-orbit coupling in actinides means the jj-base is the only one acceptable for work. Unfortunately, in this representation there are no obvious way to reduce the number of matrix elements to few significant ones. One can see that all hoppings, i.e. $f-f$, $f-s$, $f-p$, and $f-d$, have the same order of magnitude and none of them can be ignored.

Table 5.1: Tight-binding Parametrization for Cm II(in meV). $5f$ shell with $j = 5/2$

$5f$ ::	$\lvert\frac{5}{2},-\frac{5}{2}\rangle$	$\lvert\frac{5}{2},-\frac{3}{2}\rangle$	$\lvert\frac{5}{2},-\frac{1}{2}\rangle$	$\lvert\frac{5}{2},\frac{1}{2}\rangle$	$\lvert\frac{5}{2},\frac{3}{2}\rangle$	$\lvert\frac{5}{2},\frac{5}{2}\rangle$
$7s :: \lvert\frac{1}{2},-\frac{1}{2}\rangle$	-0.000	39.518	0.000	56.250	-0.000	-44.203
$7s :: \lvert\frac{1}{2},\frac{1}{2}\rangle$	44.203	0.000	-56.250	-0.000	-39.518	0.000
$6p :: \lvert\frac{1}{2},-\frac{1}{2}\rangle$	-3.191	-0.035	-2.018	-0.045	-1.427	-0.086
$6p :: \lvert\frac{1}{2},\frac{1}{2}\rangle$	0.086	-1.427	0.045	-2.018	0.035	-3.191
$6p :: \lvert\frac{3}{2},-\frac{3}{2}\rangle$	0.047	-17.637	-0.068	34.668	0.150	16.319
$6p :: \lvert\frac{3}{2},-\frac{1}{2}\rangle$	-15.552	0.082	32.334	-0.162	-50.143	-0.301
$6p :: \lvert\frac{3}{2},\frac{1}{2}\rangle$	-0.301	50.143	-0.162	-32.334	0.082	15.552
$6p :: \lvert\frac{3}{2},\frac{3}{2}\rangle$	-16.319	0.150	-34.668	-0.068	17.637	0.047
$6d :: \lvert\frac{3}{2},-\frac{3}{2}\rangle$	10.666	0.000	12.990	-0.000	-8.107	0.000
$6d :: \lvert\frac{3}{2},-\frac{1}{2}\rangle$	-0.000	-3.092	0.000	3.915	0.000	3.197
$6d :: \lvert\frac{3}{2},\frac{1}{2}\rangle$	3.197	0.000	3.915	0.000	-3.092	-0.000
$6d :: \lvert\frac{3}{2},\frac{3}{2}\rangle$	0.000	-8.107	-0.000	12.990	0.000	10.666
$6d :: \lvert\frac{5}{2},-\frac{5}{2}\rangle$	0.000	18.338	-0.000	56.954	0.000	-29.337
$6d :: \lvert\frac{5}{2},-\frac{3}{2}\rangle$	-17.279	0.000	-30.519	0.000	-107.268	0.000
$6d :: \lvert\frac{5}{2},-\frac{1}{2}\rangle$	0.000	32.228	-0.000	38.520	0.000	74.782
$6d :: \lvert\frac{5}{2},\frac{1}{2}\rangle$	-74.782	-0.000	-38.520	0.000	-32.228	-0.000
$6d :: \lvert\frac{5}{2},\frac{3}{2}\rangle$	-0.000	107.268	-0.000	30.519	-0.000	17.279
$6d :: \lvert\frac{5}{2},\frac{5}{2}\rangle$	29.337	-0.000	-56.954	0.000	-18.338	-0.000
$5f :: \lvert\frac{5}{2},-\frac{5}{2}\rangle$	-4.491	-0.061	3.559	0.040	1.522	0.000
$5f :: \lvert\frac{5}{2},-\frac{3}{2}\rangle$	-0.061	-2.711	-0.015	-1.592	0.000	1.522
$5f :: \lvert\frac{5}{2},-\frac{1}{2}\rangle$	3.559	-0.015	-6.060	0.000	-1.592	-0.040
$5f :: \lvert\frac{5}{2},\frac{1}{2}\rangle$	0.040	-1.592	0.000	-6.060	0.015	3.559
$5f :: \lvert\frac{5}{2},\frac{3}{2}\rangle$	1.522	0.000	-1.592	0.015	-2.711	0.061
$5f :: \lvert\frac{5}{2},\frac{5}{2}\rangle$	0.000	1.522	-0.040	3.559	0.061	-4.491
$5f :: \lvert\frac{7}{2},-\frac{7}{2}\rangle$	-0.021	2.815	-0.020	-17.130	-0.086	-7.192
$5f :: \lvert\frac{7}{2},-\frac{5}{2}\rangle$	-0.332	-0.031	-0.332	0.163	36.628	0.098
$5f :: \lvert\frac{7}{2},-\frac{3}{2}\rangle$	-0.002	4.375	0.113	-5.483	-0.218	-25.923
$5f :: \lvert\frac{7}{2},-\frac{1}{2}\rangle$	-2.531	0.109	-12.234	-0.133	3.966	0.075
$5f :: \lvert\frac{7}{2},\frac{1}{2}\rangle$	0.075	-3.966	-0.133	12.234	0.109	2.531
$5f :: \lvert\frac{7}{2},\frac{3}{2}\rangle$	25.923	-0.218	5.483	0.113	-4.375	-0.002
$5f :: \lvert\frac{7}{2},\frac{5}{2}\rangle$	0.098	-36.628	0.163	0.332	-0.031	0.332
$5f :: \lvert\frac{7}{2},\frac{7}{2}\rangle$	7.192	-0.086	17.130	-0.020	-2.815	-0.021

Table 5.2: Tight-binding Parametrization for Cm II(in meV). $5f$ shell with $j = 7/2$

$5f$ ::	$\|\frac{7}{2},-\frac{7}{2}\rangle$	$\|\frac{7}{2},-\frac{5}{2}\rangle$	$\|\frac{7}{2},-\frac{3}{2}\rangle$	$\|\frac{7}{2},-\frac{1}{2}\rangle$	$5\|\frac{7}{2},\frac{1}{2}\rangle$	$\|\frac{7}{2},\frac{3}{2}\rangle$	$\|\frac{7}{2},\frac{5}{2}\rangle$	$\|\frac{7}{2},\frac{7}{2}\rangle$
$7s :: \|\frac{1}{2},-\frac{1}{2}\rangle$	-53.977	0.000	70.717	-0.000	54.438	-0.000	-19.822	-0.000
$7s :: \|\frac{1}{2},\frac{1}{2}\rangle$	-0.000	-19.822	-0.000	54.438	-0.000	70.717	0.000	-53.977
$6p :: \|\frac{1}{2},-\frac{1}{2}\rangle$	0.087	-8.278	0.085	7.728	-0.030	-14.338	-0.014	-5.984
$6p :: \|\frac{1}{2},\frac{1}{2}\rangle$	5.984	-0.014	14.338	-0.030	-7.728	0.085	8.278	0.087
$6p :: \|\frac{3}{2},-\frac{3}{2}\rangle$	-0.674	0.135	-30.176	-0.091	32.368	0.108	7.124	0.006
$6p :: \|\frac{3}{2},-\frac{1}{2}\rangle$	0.313	-42.590	0.288	9.322	-0.246	-0.131	-0.010	10.693
$6p :: \|\frac{3}{2},\frac{1}{2}\rangle$	10.693	0.010	-0.131	0.246	9.322	-0.288	-42.590	-0.313
$6p :: \|\frac{3}{2},\frac{3}{2}\rangle$	-0.006	7.124	-0.108	32.368	0.091	-30.176	-0.135	-0.674
$6d :: \|\frac{3}{2},-\frac{3}{2}\rangle$	-0.000	-19.453	-0.000	-33.390	-0.000	-92.480	-0.000	30.603
$6d :: \|\frac{3}{2},-\frac{1}{2}\rangle$	44.632	-0.000	36.527	0.000	39.317	0.000	109.004	0.000
$6d :: \|\frac{3}{2},\frac{1}{2}\rangle$	-0.000	-109.004	-0.000	-39.317	-0.000	-36.527	0.000	-44.632
$6d :: \|\frac{3}{2},\frac{3}{2}\rangle$	-30.603	0.000	92.480	0.000	33.390	0.000	19.453	0.000
$6d :: \|\frac{5}{2},-\frac{5}{2}\rangle$	22.425	-0.000	32.428	0.000	54.791	-0.000	-13.797	0.000
$6d :: \|\frac{5}{2},-\frac{3}{2}\rangle$	-0.000	-20.729	0.000	-13.821	0.000	-32.339	-0.000	-15.796
$6d :: \|\frac{5}{2},-\frac{1}{2}\rangle$	57.247	0.000	21.865	-0.000	6.218	0.000	-56.385	0.000
$6d :: \|\frac{5}{2},\frac{1}{2}\rangle$	0.000	-56.385	0.000	6.218	-0.000	21.865	0.000	57.247
$6d :: \|\frac{5}{2},\frac{3}{2}\rangle$	-15.796	-0.000	-32.339	0.000	-13.821	0.000	-20.729	-0.000
$6d :: \|\frac{5}{2},\frac{5}{2}\rangle$	0.000	-13.797	-0.000	54.791	0.000	32.428	-0.000	22.425
$5f :: \|\frac{5}{2},-\frac{5}{2}\rangle$	-0.021	-0.332	-0.002	-2.531	0.075	25.923	0.098	7.192
$5f :: \|\frac{5}{2},-\frac{3}{2}\rangle$	2.815	-0.031	4.375	0.109	-3.966	-0.218	-36.628	-0.086
$5f :: \|\frac{5}{2},-\frac{1}{2}\rangle$	-0.020	-0.332	0.113	-12.234	-0.133	5.483	0.163	17.130
$5f :: \|\frac{5}{2},\frac{1}{2}\rangle$	-17.130	0.163	-5.483	-0.133	12.234	0.113	0.332	-0.020
$5f :: \|\frac{5}{2},\frac{3}{2}\rangle$	-0.086	36.628	-0.218	3.966	0.109	-4.375	-0.031	-2.815
$5f :: \|\frac{5}{2},\frac{5}{2}\rangle$	-7.192	0.098	-25.923	0.075	2.531	-0.002	0.332	-0.021
$5f :: \|\frac{7}{2},-\frac{7}{2}\rangle$	-5.887	-0.063	4.795	-0.028	-16.488	-0.057	-3.447	0.000
$5f :: \|\frac{7}{2},-\frac{5}{2}\rangle$	-0.063	-7.110	-0.098	3.071	0.139	14.737	0.000	-3.447
$5f :: \|\frac{7}{2},-\frac{3}{2}\rangle$	4.795	-0.098	0.510	0.054	-3.779	0.000	14.737	0.057
$5f :: \|\frac{7}{2},-\frac{1}{2}\rangle$	-0.028	3.071	0.054	-11.743	0.000	-3.779	-0.139	-16.488
$5f :: \|\frac{7}{2},\frac{1}{2}\rangle$	-16.488	0.139	-3.779	0.000	-11.743	-0.054	3.071	0.028
$5f :: \|\frac{7}{2},\frac{3}{2}\rangle$	-0.057	14.737	0.000	-3.779	-0.054	0.510	0.098	4.795
$5f :: \|\frac{7}{2},\frac{5}{2}\rangle$	-3.447	0.000	14.737	-0.139	3.071	0.098	-7.110	0.063
$5f :: \|\frac{7}{2},\frac{7}{2}\rangle$	0.000	-3.447	0.057	-16.488	0.028	4.795	0.063	-5.887

Table 5.3: Tight-binding Parametrization for δ-Pu(in meV). $5f$ shell with $j = 5/2$

$5f ::$	$\|\frac{5}{2}, -\frac{5}{2}\rangle$	$\|\frac{5}{2}, -\frac{3}{2}\rangle$	$\|\frac{5}{2}, -\frac{1}{2}\rangle$	$\|\frac{5}{2}, \frac{1}{2}\rangle$	$\|\frac{5}{2}, \frac{3}{2}\rangle$	$\|\frac{5}{2}, \frac{5}{2}\rangle$
$7s :: \|\frac{1}{2}, -\frac{1}{2}\rangle$	-0.000	65.442	-0.000	93.187	0.000	-75.761
$7s :: \|\frac{1}{2}, \frac{1}{2}\rangle$	75.761	-0.000	-93.187	0.000	-65.442	0.000
$6p :: \|\frac{1}{2}, -\frac{1}{2}\rangle$	-11.462	0.031	-7.249	-0.185	-5.126	-0.245
$6p :: \|\frac{1}{2}, \frac{1}{2}\rangle$	0.245	-5.126	0.185	-7.249	-0.031	-11.462
$6p :: \|\frac{3}{2}, -\frac{3}{2}\rangle$	0.085	-34.700	-0.128	67.359	0.278	31.121
$6p :: \|\frac{3}{2}, -\frac{1}{2}\rangle$	-30.108	0.225	63.537	-0.401	-97.673	-0.691
$6p :: \|\frac{3}{2}, \frac{1}{2}\rangle$	-0.691	97.673	-0.401	-63.537	0.225	30.108
$6p :: \|\frac{3}{2}, \frac{3}{2}\rangle$	-31.121	0.278	-67.359	-0.128	34.700	0.085
$6d :: \|\frac{3}{2}, -\frac{3}{2}\rangle$	20.495	-0.000	23.139	-0.000	-15.188	-0.000
$6d :: \|\frac{3}{2}, -\frac{1}{2}\rangle$	-0.000	-4.984	0.000	6.167	0.000	6.429
$6d :: \|\frac{3}{2}, \frac{1}{2}\rangle$	6.429	0.000	6.167	0.000	-4.984	-0.000
$6d :: \|\frac{3}{2}, \frac{3}{2}\rangle$	-0.000	-15.188	-0.000	23.139	-0.000	20.495
$6d :: \|\frac{5}{2}, -\frac{5}{2}\rangle$	0.000	31.255	-0.000	88.606	0.000	-48.892
$6d :: \|\frac{5}{2}, -\frac{3}{2}\rangle$	-29.423	-0.000	-50.447	0.000	-172.109	-0.000
$6d :: \|\frac{5}{2}, -\frac{1}{2}\rangle$	-0.000	51.845	0.000	62.223	-0.000	122.310
$6d :: \|\frac{5}{2}, \frac{1}{2}\rangle$	-122.310	0.000	-62.223	-0.000	-51.845	0.000
$6d :: \|\frac{5}{2}, \frac{3}{2}\rangle$	0.000	172.109	-0.000	50.447	0.000	29.423
$6d :: \|\frac{5}{2}, \frac{5}{2}\rangle$	48.892	-0.000	-88.606	0.000	-31.255	-0.000
$5f :: \|\frac{5}{2}, -\frac{5}{2}\rangle$	-11.028	-0.121	7.980	0.095	3.633	0.000
$5f :: \|\frac{5}{2}, -\frac{3}{2}\rangle$	-0.121	-7.136	-0.037	-3.779	-0.000	3.633
$5f :: \|\frac{5}{2}, -\frac{1}{2}\rangle$	7.980	-0.037	-14.302	-0.000	-3.779	-0.095
$5f :: \|\frac{5}{2}, \frac{1}{2}\rangle$	0.095	-3.779	-0.000	-14.302	0.037	7.980
$5f :: \|\frac{5}{2}, \frac{3}{2}\rangle$	3.633	-0.000	-3.779	0.037	-7.136	0.121
$5f :: \|\frac{5}{2}, \frac{5}{2}\rangle$	0.000	3.633	-0.095	7.980	0.121	-11.028
$5f :: \|\frac{7}{2}, -\frac{7}{2}\rangle$	-0.039	6.137	-0.028	-32.926	-0.172	-14.453
$5f :: \|\frac{7}{2}, -\frac{5}{2}\rangle$	-0.435	-0.074	-1.048	0.337	71.869	0.195
$5f :: \|\frac{7}{2}, -\frac{3}{2}\rangle$	-0.014	8.162	0.246	-11.428	-0.457	-50.190
$5f :: \|\frac{7}{2}, -\frac{1}{2}\rangle$	-5.679	0.240	-23.693	-0.287	8.109	0.142
$5f :: \|\frac{7}{2}, \frac{1}{2}\rangle$	0.142	-8.109	-0.287	23.693	0.240	5.679
$5f :: \|\frac{7}{2}, \frac{3}{2}\rangle$	50.190	-0.457	11.428	0.246	-8.162	-0.014
$5f :: \|\frac{7}{2}, \frac{5}{2}\rangle$	0.195	-71.869	0.337	1.048	-0.074	0.435
$5f :: \|\frac{7}{2}, \frac{7}{2}\rangle$	14.453	-0.172	32.926	-0.028	-6.137	-0.039

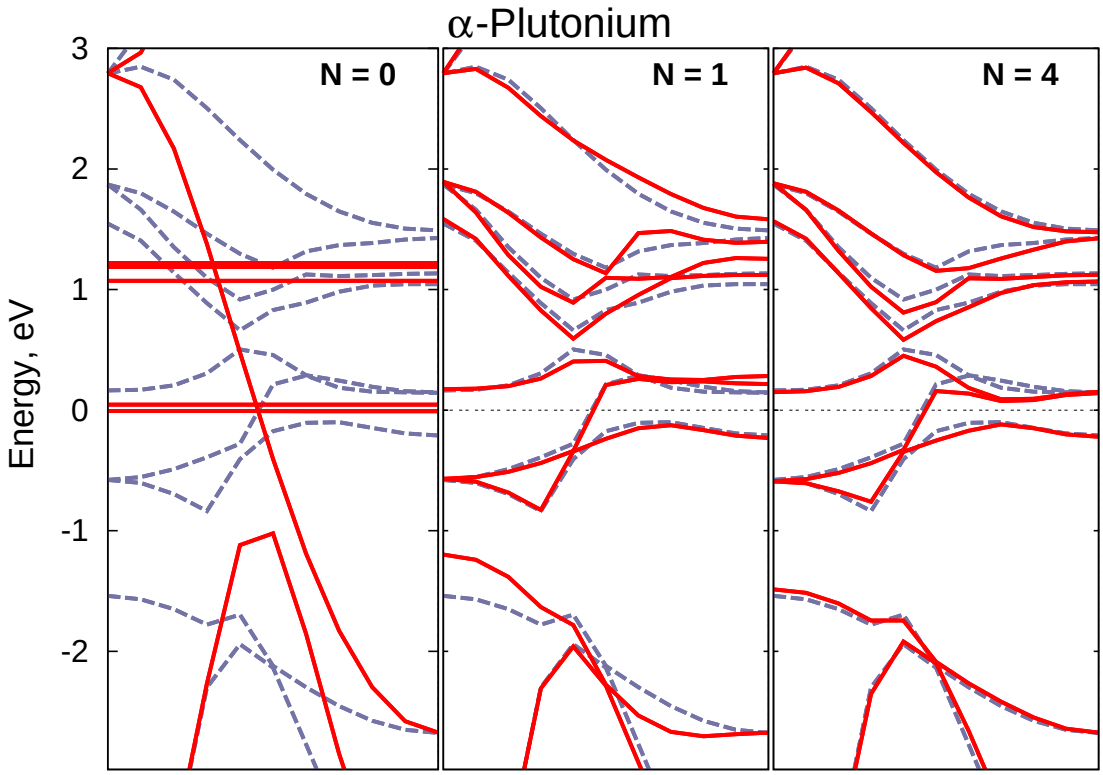

Figure 5.5: Band structure of α-Pu when N nearest neighbors are taken into account for f-orbitals (red solid line) is compared to original LDA bands (dashed grey line). The band structures are plotted for Γ-X direction.

The result of the same real space analysis for δ-Pu is shown in Figure 5.4. At most left panel one can see the on-site energy levels of $5f$ electrons in δ-Pu. As discussed earlier the $5f$-orbitals of δ-Pu are slightly more itinerant than ones of Cm. At the second panel of Figure 5.4 one can see when nearest neighbors are included there small discrepancies among bands of real space Hamiltonian and original LSDA bands even within $5f$ block. Around Γ-point the coincidence of two is amazing, but in the vicinity of X-point inconsistency is more noticeable than in the case of Cm. However, the range of extension $5f$ orbitals is the same: hoppings to the nearest neighbors very

Table 5.4: Tight-binding Parametrization for δ-Pu(in meV). $5f$ shell with $j = 7/2$

$5f ::$	$\lvert\frac{7}{2},-\frac{7}{2}\rangle$	$\lvert\frac{7}{2},-\frac{5}{2}\rangle$	$\lvert\frac{7}{2},-\frac{3}{2}\rangle$	$\lvert\frac{7}{2},-\frac{1}{2}\rangle$	$\lvert\frac{7}{2},\frac{1}{2}\rangle$	$\lvert\frac{7}{2},\frac{3}{2}\rangle$	$\lvert\frac{7}{2},\frac{5}{2}\rangle$	$\lvert\frac{7}{2},\frac{7}{2}\rangle$
$7s :: \lvert\frac{1}{2},-\frac{1}{2}\rangle$	-89.263	0.000	113.127	0.000	87.147	-0.000	-32.822	-0.000
$7s :: \lvert\frac{1}{2},\frac{1}{2}\rangle$	-0.000	-32.822	-0.000	87.147	0.000	113.127	0.000	-89.263
$6p :: \lvert\frac{1}{2},-\frac{1}{2}\rangle$	0.283	-27.776	0.241	29.408	-0.121	-48.109	-0.128	-17.139
$6p :: \lvert\frac{1}{2},\frac{1}{2}\rangle$	17.139	-0.128	48.109	-0.121	-29.408	0.241	27.776	0.283
$6p :: \lvert\frac{3}{2},-\frac{3}{2}\rangle$	-1.793	0.247	-58.670	-0.179	62.045	0.200	13.409	0.016
$6p :: \lvert\frac{3}{2},-\frac{1}{2}\rangle$	0.736	-82.131	0.647	17.984	-0.554	-0.408	-0.077	20.071
$6p :: \lvert\frac{3}{2},\frac{1}{2}\rangle$	20.071	0.077	-0.408	0.554	17.984	-0.647	-82.131	-0.736
$6p :: \lvert\frac{3}{2},\frac{3}{2}\rangle$	-0.016	13.409	-0.200	62.045	0.179	-58.670	-0.247	-1.793
$6d :: \lvert\frac{3}{2},-\frac{3}{2}\rangle$	-0.000	-31.813	-0.000	-54.565	-0.000	-142.988	0.000	49.849
$6d :: \lvert\frac{3}{2},-\frac{1}{2}\rangle$	71.902	-0.000	57.510	-0.000	62.129	0.000	172.802	0.000
$6d :: \lvert\frac{3}{2},\frac{1}{2}\rangle$	-0.000	-172.802	-0.000	-62.129	0.000	-57.510	0.000	-71.902
$6d :: \lvert\frac{3}{2},\frac{3}{2}\rangle$	-49.849	-0.000	142.988	0.000	54.565	0.000	31.813	0.000
$6d :: \lvert\frac{5}{2},-\frac{5}{2}\rangle$	39.319	-0.000	53.729	0.000	83.179	-0.000	-22.347	-0.000
$6d :: \lvert\frac{5}{2},-\frac{3}{2}\rangle$	0.000	-31.147	0.000	-20.918	0.000	-52.706	0.000	-25.616
$6d :: \lvert\frac{5}{2},-\frac{1}{2}\rangle$	91.791	0.000	34.975	-0.000	9.811	-0.000	-88.055	0.000
$6d :: \lvert\frac{5}{2},\frac{1}{2}\rangle$	0.000	-88.055	-0.000	9.811	-0.000	34.975	0.000	91.791
$6d :: \lvert\frac{5}{2},\frac{3}{2}\rangle$	-25.616	0.000	-52.706	0.000	-20.918	0.000	-31.147	0.000
$6d :: \lvert\frac{5}{2},\frac{5}{2}\rangle$	-0.000	-22.347	-0.000	83.179	0.000	53.729	-0.000	39.319
$5f :: \lvert\frac{5}{2},-\frac{5}{2}\rangle$	-0.039	-0.435	-0.014	-5.679	0.142	50.190	0.195	14.453
$5f :: \lvert\frac{5}{2},-\frac{3}{2}\rangle$	6.137	-0.074	8.162	0.240	-8.109	-0.457	-71.869	-0.172
$5f :: \lvert\frac{5}{2},-\frac{1}{2}\rangle$	-0.028	-1.048	0.246	-23.693	-0.287	11.428	0.337	32.926
$5f :: \lvert\frac{5}{2},\frac{1}{2}\rangle$	-32.926	0.337	-11.428	-0.287	23.693	0.246	1.048	-0.028
$5f :: \lvert\frac{5}{2},\frac{3}{2}\rangle$	-0.172	71.869	-0.457	8.109	0.240	-8.162	-0.074	-6.137
$5f :: \lvert\frac{5}{2},\frac{5}{2}\rangle$	-14.453	0.195	-50.190	0.142	5.679	-0.014	0.435	-0.039
$5f :: \lvert\frac{7}{2},-\frac{7}{2}\rangle$	-13.323	-0.124	10.089	-0.038	-30.984	-0.110	-6.749	-0.000
$5f :: \lvert\frac{7}{2},-\frac{5}{2}\rangle$	-0.124	-15.187	-0.210	6.104	0.295	28.591	0.000	-6.749
$5f :: \lvert\frac{7}{2},-\frac{3}{2}\rangle$	10.089	-0.210	-1.182	0.109	-7.834	-0.000	28.591	0.110
$5f :: \lvert\frac{7}{2},-\frac{1}{2}\rangle$	-0.038	6.104	0.109	-24.513	-0.000	-7.834	-0.295	-30.984
$5f :: \lvert\frac{7}{2},\frac{1}{2}\rangle$	-30.984	0.295	-7.834	-0.000	-24.513	-0.109	6.104	0.038
$5f :: \lvert\frac{7}{2},\frac{3}{2}\rangle$	-0.110	28.591	-0.000	-7.834	-0.109	-1.182	0.210	10.089
$5f :: \lvert\frac{7}{2},\frac{5}{2}\rangle$	-6.749	0.000	28.591	-0.295	6.104	0.210	-15.187	0.124
$5f :: \lvert\frac{7}{2},\frac{7}{2}\rangle$	-0.000	-6.749	0.110	-30.984	0.038	10.089	0.124	-13.323

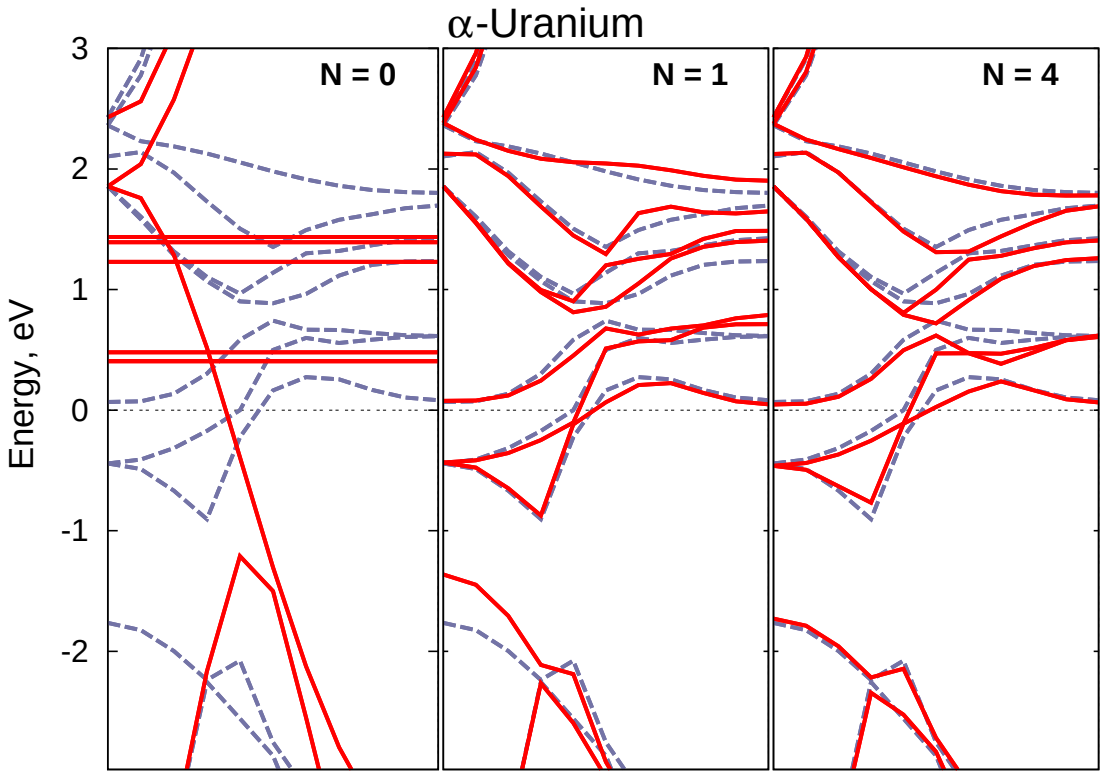

Figure 5.6: Band structure of α-U when N nearest neighbors are taken into account for f-orbitals (red solid line) is compared to original LDA bands (dashed grey line). The band structures are plotted for Γ-X direction.

well reproduce LSDA bands. Again, inclusion of four nearest neighbors make two band structures look even closer (see right panel of Figure 5.4). The corresponding tight-binding parametrization is provided in Tables 5.3 and 5.2. The parametrization is given for (1/2,0,1/2) spatial direction.

Finally, the analogous plot for α-Pu and α-U are presented in Figures 5.5 and 5.6 correspondingly. The first nearest neighbors still reproduce qualitatively the LSDA band structure. One can see that some discrepancies between bands of real space Hamiltonian and LSDA bands remain even when four nearest neighbors are taken into account. This suggests that $5f$-orbitals in light actinides tend to long-range behavior. Tables 5.5, 5.6, 5.7 and 5.8 list corresponding tight-binding parametrizations in jj base for (1/2, 0, 1/2) spatial direction.

Table 5.5: Tight-binding Parametrization for α-Pu(in meV). $5f$ shell with $j = 5/2$

$5f ::$	$\|\frac{5}{2}, -\frac{5}{2}\rangle$	$\|\frac{5}{2}, -\frac{3}{2}\rangle$	$\|\frac{5}{2}, -\frac{1}{2}\rangle$	$\|\frac{5}{2}, \frac{1}{2}\rangle$	$\|\frac{5}{2}, \frac{3}{2}\rangle$	$\|\frac{5}{2}, \frac{5}{2}\rangle$
$7s :: \|\frac{1}{2}, -\frac{1}{2}\rangle$	-0.000	87.896	-0.000	125.415	0.000	-105.125
$7s :: \|\frac{1}{2}, \frac{1}{2}\rangle$	105.125	-0.000	-125.415	0.000	-87.896	0.000
$6p :: \|\frac{1}{2}, -\frac{1}{2}\rangle$	-19.838	0.108	-12.546	-0.295	-8.872	-0.365
$6p :: \|\frac{1}{2}, \frac{1}{2}\rangle$	0.365	-8.872	0.295	-12.546	-0.108	-19.838
$6p :: \|\frac{3}{2}, -\frac{3}{2}\rangle$	0.142	-53.691	-0.190	103.499	0.447	47.263
$6p :: \|\frac{3}{2}, -\frac{1}{2}\rangle$	-46.180	0.317	98.284	-0.598	-150.257	-1.066
$6p :: \|\frac{3}{2}, \frac{1}{2}\rangle$	-1.066	150.257	-0.598	-98.284	0.317	46.180
$6p :: \|\frac{3}{2}, \frac{3}{2}\rangle$	-47.263	0.447	-103.499	-0.190	53.691	0.142
$6d :: \|\frac{3}{2}, -\frac{3}{2}\rangle$	28.073	0.000	32.132	0.000	-21.135	0.000
$6d :: \|\frac{3}{2}, -\frac{1}{2}\rangle$	0.000	-8.044	0.000	8.447	-0.000	9.456
$6d :: \|\frac{3}{2}, \frac{1}{2}\rangle$	9.456	-0.000	8.447	0.000	-8.044	0.000
$6d :: \|\frac{3}{2}, \frac{3}{2}\rangle$	0.000	-21.135	0.000	32.132	0.000	28.073
$6d :: \|\frac{5}{2}, -\frac{5}{2}\rangle$	-0.000	43.250	0.000	122.549	-0.000	-66.892
$6d :: \|\frac{5}{2}, -\frac{3}{2}\rangle$	-41.255	0.000	-69.648	-0.000	-238.129	-0.000
$6d :: \|\frac{5}{2}, -\frac{1}{2}\rangle$	0.000	72.515	-0.000	85.797	0.000	169.800
$6d :: \|\frac{5}{2}, \frac{1}{2}\rangle$	-169.800	-0.000	-85.797	0.000	-72.515	-0.000
$6d :: \|\frac{5}{2}, \frac{3}{2}\rangle$	0.000	238.129	0.000	69.648	-0.000	41.255
$6d :: \|\frac{5}{2}, \frac{5}{2}\rangle$	66.892	0.000	-122.549	-0.000	-43.250	0.000
$5f :: \|\frac{5}{2}, -\frac{5}{2}\rangle$	-17.520	-0.160	12.278	0.133	5.594	0.000
$5f :: \|\frac{5}{2}, -\frac{3}{2}\rangle$	-0.160	-11.288	-0.046	-5.992	0.000	5.594
$5f :: \|\frac{5}{2}, -\frac{1}{2}\rangle$	12.278	-0.046	-22.429	0.000	-5.992	-0.133
$5f :: \|\frac{5}{2}, \frac{1}{2}\rangle$	0.133	-5.992	0.000	-22.429	0.046	12.278
$5f :: \|\frac{5}{2}, \frac{3}{2}\rangle$	5.594	0.000	-5.992	0.046	-11.288	0.160
$5f :: \|\frac{5}{2}, \frac{5}{2}\rangle$	0.000	5.594	-0.133	12.278	0.160	-17.520
$5f :: \|\frac{7}{2}, -\frac{7}{2}\rangle$	-0.048	9.420	-0.046	-48.720	-0.248	-20.785
$5f :: \|\frac{7}{2}, -\frac{5}{2}\rangle$	-0.447	-0.110	-1.969	0.498	106.485	0.276
$5f :: \|\frac{7}{2}, -\frac{3}{2}\rangle$	-0.026	12.049	0.359	-16.888	-0.672	-74.259
$5f :: \|\frac{7}{2}, -\frac{1}{2}\rangle$	-8.845	0.350	-35.659	-0.427	11.862	0.214
$5f :: \|\frac{7}{2}, \frac{1}{2}\rangle$	0.214	-11.862	-0.427	35.659	0.350	8.845
$5f :: \|\frac{7}{2}, \frac{3}{2}\rangle$	74.259	-0.672	16.888	0.359	-12.049	-0.026
$5f :: \|\frac{7}{2}, \frac{5}{2}\rangle$	0.276	-106.485	0.498	1.969	-0.110	0.447
$5f :: \|\frac{7}{2}, \frac{7}{2}\rangle$	20.785	-0.248	48.720	-0.046	-9.420	-0.048

Table 5.6: Tight-binding Parametrization for α-Pu(in meV). $5f$ shell with $j = 7/2$

$5f ::$	$\|\frac{7}{2}, -\frac{7}{2}\rangle$	$\|\frac{7}{2}, -\frac{5}{2}\rangle$	$\|\frac{7}{2}, -\frac{3}{2}\rangle$	$\|\frac{7}{2}, -\frac{1}{2}\rangle$	$\|\frac{7}{2}, \frac{1}{2}\rangle$	$\|\frac{7}{2}, \frac{3}{2}\rangle$	$\|\frac{7}{2}, \frac{5}{2}\rangle$	$\|\frac{7}{2}, \frac{7}{2}\rangle$
$7s :: \|\frac{1}{2}, -\frac{1}{2}\rangle$	-122.919	0.000	151.060	0.000	116.231	-0.000	-44.967	0.000
$7s :: \|\frac{1}{2}, \frac{1}{2}\rangle$	0.000	-44.967	-0.000	116.231	0.000	151.060	0.000	-122.919
$6p :: \|\frac{1}{2}, -\frac{1}{2}\rangle$	0.449	-48.186	0.348	52.432	-0.191	-83.461	-0.258	-28.537
$6p :: \|\frac{1}{2}, \frac{1}{2}\rangle$	28.537	-0.258	83.461	-0.191	-52.432	0.348	48.186	0.449
$6p :: \|\frac{3}{2}, -\frac{3}{2}\rangle$	-2.935	0.403	-90.168	-0.274	94.637	0.318	20.245	0.031
$6p :: \|\frac{3}{2}, -\frac{1}{2}\rangle$	1.142	-125.590	0.971	27.706	-0.832	-0.617	-0.110	30.174
$6p :: \|\frac{3}{2}, \frac{1}{2}\rangle$	30.174	0.110	-0.617	0.832	27.706	-0.971	-125.590	-1.142
$6p :: \|\frac{3}{2}, \frac{3}{2}\rangle$	-0.031	20.245	-0.318	94.637	0.274	-90.168	-0.403	-2.935
$6d :: \|\frac{3}{2}, -\frac{3}{2}\rangle$	-0.000	-44.187	-0.000	-74.619	0.000	-196.634	-0.000	67.630
$6d :: \|\frac{3}{2}, -\frac{1}{2}\rangle$	99.207	-0.000	79.410	0.000	84.880	-0.000	237.550	0.000
$6d :: \|\frac{3}{2}, \frac{1}{2}\rangle$	-0.000	-237.550	0.000	-84.880	-0.000	-79.410	0.000	-99.207
$6d :: \|\frac{3}{2}, \frac{3}{2}\rangle$	-67.630	0.000	196.634	-0.000	74.619	0.000	44.187	0.000
$6d :: \|\frac{5}{2}, -\frac{5}{2}\rangle$	53.526	0.000	73.530	-0.000	113.928	0.000	-30.343	0.000
$6d :: \|\frac{5}{2}, -\frac{3}{2}\rangle$	0.000	-43.648	-0.000	-28.405	-0.000	-72.400	-0.000	-34.609
$6d :: \|\frac{5}{2}, -\frac{1}{2}\rangle$	126.327	0.000	47.734	-0.000	13.558	0.000	-120.456	0.000
$6d :: \|\frac{5}{2}, \frac{1}{2}\rangle$	0.000	-120.456	0.000	13.558	-0.000	47.734	0.000	126.327
$6d :: \|\frac{5}{2}, \frac{3}{2}\rangle$	-34.609	-0.000	-72.400	-0.000	-28.405	-0.000	-43.648	0.000
$6d :: \|\frac{5}{2}, \frac{5}{2}\rangle$	0.000	-30.343	0.000	113.928	-0.000	73.530	0.000	53.526
$5f :: \|\frac{5}{2}, -\frac{5}{2}\rangle$	-0.048	-0.447	-0.026	-8.845	0.214	74.259	0.276	20.785
$5f :: \|\frac{5}{2}, -\frac{3}{2}\rangle$	9.420	-0.110	12.049	0.350	-11.862	-0.672	-106.485	-0.248
$5f :: \|\frac{5}{2}, -\frac{1}{2}\rangle$	-0.046	-1.969	0.359	-35.659	-0.427	16.888	0.498	48.720
$5f :: \|\frac{5}{2}, \frac{1}{2}\rangle$	-48.720	0.498	-16.888	-0.427	35.659	0.359	1.969	-0.046
$5f :: \|\frac{5}{2}, \frac{3}{2}\rangle$	-0.248	106.485	-0.672	11.862	0.350	-12.049	-0.110	-9.420
$5f :: \|\frac{5}{2}, \frac{5}{2}\rangle$	-20.785	0.276	-74.259	0.214	8.845	-0.026	0.447	-0.048
$5f :: \|\frac{7}{2}, -\frac{7}{2}\rangle$	-20.464	-0.168	15.154	-0.059	-45.538	-0.155	-9.709	0.000
$5f :: \|\frac{7}{2}, -\frac{5}{2}\rangle$	-0.168	-22.743	-0.293	8.901	0.432	41.939	0.000	-9.709
$5f :: \|\frac{7}{2}, -\frac{3}{2}\rangle$	15.154	-0.293	-2.221	0.167	-11.603	0.000	41.939	0.155
$5f :: \|\frac{7}{2}, -\frac{1}{2}\rangle$	-0.059	8.901	0.167	-37.103	0.000	-11.603	-0.432	-45.538
$5f :: \|\frac{7}{2}, \frac{1}{2}\rangle$	-45.538	0.432	-11.603	0.000	-37.103	-0.167	8.901	0.059
$5f :: \|\frac{7}{2}, \frac{3}{2}\rangle$	-0.155	41.939	0.000	-11.603	-0.167	-2.221	0.293	15.154
$5f :: \|\frac{7}{2}, \frac{5}{2}\rangle$	-9.709	0.000	41.939	-0.432	8.901	0.293	-22.743	0.168
$5f :: \|\frac{7}{2}, \frac{7}{2}\rangle$	0.000	-9.709	0.155	-45.538	0.059	15.154	0.168	-20.464

Table 5.7: Tight-binding Parametrization for α-U(in meV). $5f$ shell with $j = 5/2$

$5f ::$	$\|\frac{5}{2}, -\frac{5}{2}\rangle$	$\|\frac{5}{2}, -\frac{3}{2}\rangle$	$\|\frac{5}{2}, -\frac{1}{2}\rangle$	$\|\frac{5}{2}, \frac{1}{2}\rangle$	$5f :: \|\frac{5}{2}, \frac{3}{2}\rangle$	$5f :: \|\frac{5}{2}, \frac{5}{2}\rangle$
$7s :: \|\frac{1}{2}, -\frac{1}{2}\rangle$	-0.000	99.202	-0.000	141.540	0.000	-120.642
$7s :: \|\frac{1}{2}, \frac{1}{2}\rangle$	120.642	-0.000	-141.540	0.000	-99.202	0.000
$6p :: \|\frac{1}{2}, -\frac{1}{2}\rangle$	-25.446	0.164	-16.093	-0.388	-11.380	-0.469
$6p :: \|\frac{1}{2}, \frac{1}{2}\rangle$	0.469	-11.380	0.388	-16.093	-0.164	-25.446
$6p :: \|\frac{3}{2}, -\frac{3}{2}\rangle$	0.157	-63.190	-0.218	121.859	0.510	55.603
$6p :: \|\frac{3}{2}, -\frac{1}{2}\rangle$	-54.401	0.383	115.750	-0.703	-176.848	-1.270
$6p :: \|\frac{3}{2}, \frac{1}{2}\rangle$	-1.270	176.848	-0.703	-115.750	0.383	54.401
$6p :: \|\frac{3}{2}, \frac{3}{2}\rangle$	-55.603	0.510	-121.859	-0.218	63.190	0.157
$6d :: \|\frac{3}{2}, -\frac{3}{2}\rangle$	32.681	0.000	37.292	0.000	-24.242	0.000
$6d :: \|\frac{3}{2}, -\frac{1}{2}\rangle$	0.000	-9.142	0.000	10.328	-0.000	11.334
$6d :: \|\frac{3}{2}, \frac{1}{2}\rangle$	11.334	-0.000	10.328	0.000	-9.142	0.000
$6d :: \|\frac{3}{2}, \frac{3}{2}\rangle$	0.000	-24.242	0.000	37.292	0.000	32.681
$6d :: \|\frac{5}{2}, -\frac{5}{2}\rangle$	-0.000	49.843	0.000	141.073	-0.000	-76.691
$6d :: \|\frac{5}{2}, -\frac{3}{2}\rangle$	-47.682	0.000	-79.937	-0.000	-273.878	-0.000
$6d :: \|\frac{5}{2}, -\frac{1}{2}\rangle$	0.000	83.817	-0.000	98.978	0.000	195.822
$6d :: \|\frac{5}{2}, \frac{1}{2}\rangle$	-195.822	-0.000	-98.978	0.000	-83.817	-0.000
$6d :: \|\frac{5}{2}, \frac{3}{2}\rangle$	0.000	273.878	0.000	79.937	-0.000	47.682
$6d :: \|\frac{5}{2}, \frac{5}{2}\rangle$	76.691	0.000	-141.073	-0.000	-49.843	0.000
$5f :: \|\frac{5}{2}, -\frac{5}{2}\rangle$	-23.985	-0.201	16.003	0.167	7.211	0.000
$5f :: \|\frac{5}{2}, -\frac{3}{2}\rangle$	-0.201	-16.301	-0.052	-7.398	0.000	7.211
$5f :: \|\frac{5}{2}, -\frac{1}{2}\rangle$	16.003	-0.052	-30.711	0.000	-7.398	-0.167
$5f :: \|\frac{5}{2}, \frac{1}{2}\rangle$	0.167	-7.398	0.000	-30.711	0.052	16.003
$5f :: \|\frac{5}{2}, \frac{3}{2}\rangle$	7.211	0.000	-7.398	0.052	-16.301	0.201
$5f :: \|\frac{5}{2}, \frac{5}{2}\rangle$	0.000	7.211	-0.167	16.003	0.201	-23.985
$5f :: \|\frac{7}{2}, -\frac{7}{2}\rangle$	-0.059	12.016	-0.066	-62.628	-0.318	-26.474
$5f :: \|\frac{7}{2}, -\frac{5}{2}\rangle$	-0.747	-0.139	-2.294	0.643	136.499	0.353
$5f :: \|\frac{7}{2}, -\frac{3}{2}\rangle$	-0.035	15.523	0.462	-21.324	-0.864	-95.380
$5f :: \|\frac{7}{2}, -\frac{1}{2}\rangle$	-11.203	0.448	-45.864	-0.558	15.152	0.283
$5f :: \|\frac{7}{2}, \frac{1}{2}\rangle$	0.283	-15.152	-0.558	45.864	0.448	11.203
$5f :: \|\frac{7}{2}, \frac{3}{2}\rangle$	95.380	-0.864	21.324	0.462	-15.523	-0.035
$5f :: \|\frac{7}{2}, \frac{5}{2}\rangle$	0.353	-136.499	0.643	2.294	-0.139	0.747
$5f :: \|\frac{7}{2}, \frac{7}{2}\rangle$	26.474	-0.318	62.628	-0.066	-12.016	-0.059

Table 5.8: Tight-binding Parametrization for α-U(in meV). $5f$ shell with $j = 7/2$

$5f ::$	$\lvert\frac{7}{2},-\frac{7}{2}\rangle$	$\lvert\frac{7}{2},-\frac{5}{2}\rangle$	$\lvert\frac{7}{2},-\frac{3}{2}\rangle$	$\lvert\frac{7}{2},-\frac{1}{2}\rangle$	$\lvert\frac{7}{2},\frac{1}{2}\rangle$	$\lvert\frac{7}{2},\frac{3}{2}\rangle$	$\lvert\frac{7}{2},\frac{5}{2}\rangle$	$\lvert\frac{7}{2},\frac{7}{2}\rangle$
$7s :: \lvert\frac{1}{2},-\frac{1}{2}\rangle$	-139.181	0.000	168.320	0.000	129.529	-0.000	-50.964	0.000
$7s :: \lvert\frac{1}{2},\frac{1}{2}\rangle$	0.000	-50.964	-0.000	129.529	0.000	168.320	0.000	-139.18
$6p :: \lvert\frac{1}{2},-\frac{1}{2}\rangle$	0.575	-61.031	0.427	67.026	-0.232	-105.709	-0.338	-35.623
$6p :: \lvert\frac{1}{2},\frac{1}{2}\rangle$	35.623	-0.338	105.709	-0.232	-67.026	0.427	61.031	0.575
$6p :: \lvert\frac{3}{2},-\frac{3}{2}\rangle$	-3.391	0.439	-105.074	-0.313	110.331	0.358	23.602	0.037
$6p :: \lvert\frac{3}{2},-\frac{1}{2}\rangle$	1.354	-146.370	1.115	32.300	-0.961	-0.720	-0.150	35.194
$6p :: \lvert\frac{3}{2},\frac{1}{2}\rangle$	35.194	0.150	-0.720	0.961	32.300	-1.115	-146.370	-1.354
$6p :: \lvert\frac{3}{2},\frac{3}{2}\rangle$	-0.037	23.602	-0.358	110.331	0.313	-105.074	-0.439	-3.391
$6d :: \lvert\frac{3}{2},-\frac{3}{2}\rangle$	0.000	-50.320	-0.000	-84.623	0.000	-223.397	0.000	76.527
$6d :: \lvert\frac{3}{2},-\frac{1}{2}\rangle$	113.004	-0.000	90.736	0.000	96.447	-0.000	269.637	-0.000
$6d :: \lvert\frac{3}{2},\frac{1}{2}\rangle$	0.000	-269.637	0.000	-96.447	-0.000	-90.736	0.000	-113.00
$6d :: \lvert\frac{3}{2},\frac{3}{2}\rangle$	-76.527	-0.000	223.397	-0.000	84.623	0.000	50.320	-0.000
$6d :: \lvert\frac{5}{2},-\frac{5}{2}\rangle$	61.062	0.000	83.531	-0.000	129.378	0.000	-34.255	0.000
$6d :: \lvert\frac{5}{2},-\frac{3}{2}\rangle$	-0.000	-49.527	-0.000	-31.773	-0.000	-81.835	-0.000	-39.136
$6d :: \lvert\frac{5}{2},-\frac{1}{2}\rangle$	143.693	0.000	54.677	-0.000	16.180	0.000	-136.254	-0.000
$6d :: \lvert\frac{5}{2},\frac{1}{2}\rangle$	-0.000	-136.254	0.000	16.180	-0.000	54.677	0.000	143.693
$6d :: \lvert\frac{5}{2},\frac{3}{2}\rangle$	-39.136	-0.000	-81.835	-0.000	-31.773	-0.000	-49.527	-0.000
$6d :: \lvert\frac{5}{2},\frac{5}{2}\rangle$	0.000	-34.255	0.000	129.378	-0.000	83.531	0.000	61.062
$5f :: \lvert\frac{5}{2},-\frac{5}{2}\rangle$	-0.059	-0.747	-0.035	-11.203	0.283	95.380	0.353	26.474
$5f :: \lvert\frac{5}{2},-\frac{3}{2}\rangle$	12.016	-0.139	15.523	0.448	-15.152	-0.864	-136.499	-0.318
$5f :: \lvert\frac{5}{2},-\frac{1}{2}\rangle$	-0.066	-2.294	0.462	-45.864	-0.558	21.324	0.643	62.628
$5f :: \lvert\frac{5}{2},\frac{1}{2}\rangle$	-62.628	0.643	-21.324	-0.558	45.864	0.462	2.294	-0.066
$5f :: \lvert\frac{5}{2},\frac{3}{2}\rangle$	-0.318	136.499	-0.864	15.152	0.448	-15.523	-0.139	-12.016
$5f :: \lvert\frac{5}{2},\frac{5}{2}\rangle$	-26.474	0.353	-95.380	0.283	11.203	-0.035	0.747	-0.059
$5f :: \lvert\frac{7}{2},-\frac{7}{2}\rangle$	-26.921	-0.206	19.090	-0.083	-57.824	-0.196	-12.201	0.000
$5f :: \lvert\frac{7}{2},-\frac{5}{2}\rangle$	-0.206	-30.153	-0.364	11.465	0.546	52.900	0.000	-12.201
$5f :: \lvert\frac{7}{2},-\frac{3}{2}\rangle$	19.090	-0.364	-4.178	0.222	-14.136	0.000	52.900	0.196
$5f :: \lvert\frac{7}{2},-\frac{1}{2}\rangle$	-0.083	11.465	0.222	-48.533	0.000	-14.136	-0.546	-57.824
$5f :: \lvert\frac{7}{2},\frac{1}{2}\rangle$	-57.824	0.546	-14.136	0.000	-48.533	-0.222	11.465	0.083
$5f :: \lvert\frac{7}{2},\frac{3}{2}\rangle$	-0.196	52.900	0.000	-14.136	-0.222	-4.178	0.364	19.090
$5f :: \lvert\frac{7}{2},\frac{5}{2}\rangle$	-12.201	0.000	52.900	-0.546	11.465	0.364	-30.153	0.206
$5f :: \lvert\frac{7}{2},\frac{7}{2}\rangle$	0.000	-12.201	0.196	-57.824	0.083	19.090	0.206	-26.921

Table 5.9: Nearest Neighbors contributions to V and t_{ff}.

	V	t_{ff}	V/t_{ff}
α-U	0.371	0.172	2.157
α-Pu	0.324	0.134	2.418
δ-Pu	0.232	0.090	2.578
Cm II	0.143	0.045	3.178

5.3.1 Table for $\bar{t^f}$ and $\bar{V}$

In the previous chapter we calculated static quantitative characteristics of the Hamiltonian average $f-f$ hooping $\bar{t^f}$ and average hybridization $\bar{V}$. Since, as was shown in previous section, f-orbitals are extremely local in actinide and the low energy physics is ruled by nearest neighbor hoppings, it is of particular interest to calculate the contribution of first nearest neighbors to $\bar{t^f}$ and $\bar{V}$. These contributions are listed in Table 5.9 and compared to the integral values in the diagram 5.7.

In the histogram the shadowed bars represent $\bar{V}$ (red) and $\bar{t^f}$ (green) for the original Hamiltonian while the bright bars represent contributions from nearest neighbors. First nearest neighbors contribute $\approx 75\%$ to the hybridization and $\approx 90\%$ to the $f-f$ hoppings. In the inset of Figure 5.7 we plot ratio of $\bar{V}/\bar{t^f}$ for the integral values (blue squares) and partial first nearest neighbors contributions (green circles). The similarity of shapes and slopes of those two curves implies that first nearest neighbors contribution governs the dynamic of V and t_{ff}.

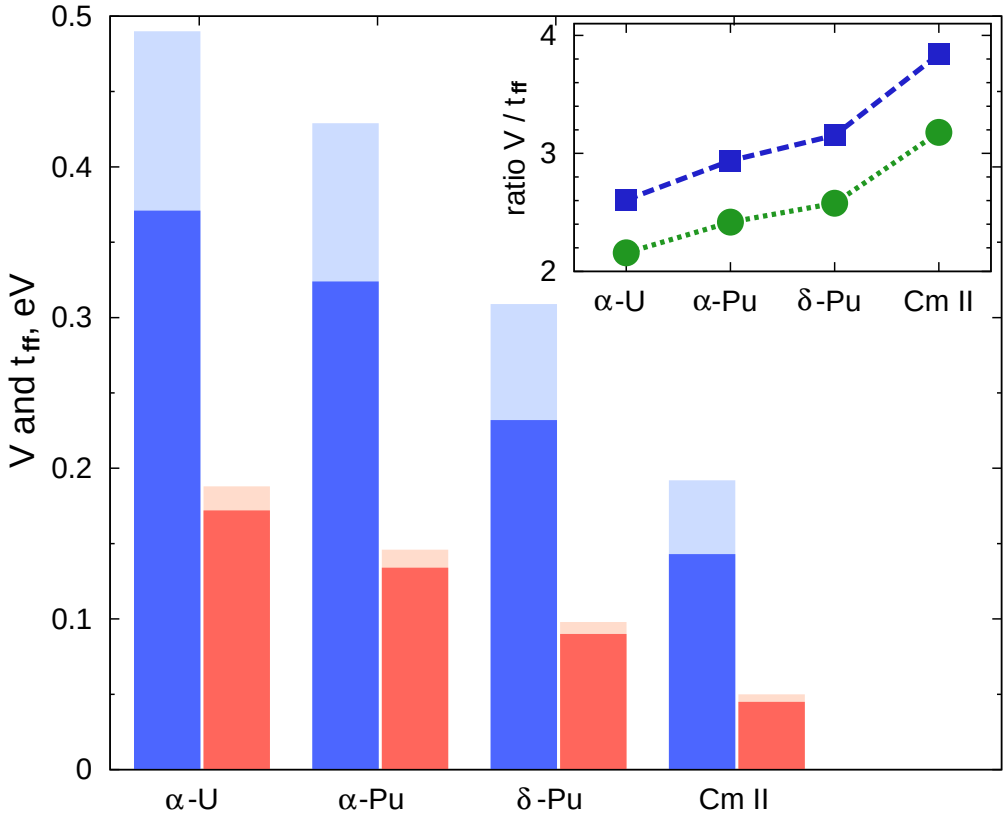

Figure 5.7: Histogram represents average hybridization among f- and spd-blocks(red bars) and $f-f$ hoppings (green bars) as functions of atomic number. The shadow bars show V and $t_f f$ for the original Hamiltonian and bright bars represent values of V and t_{ff} calculated with inclusion of nearest neighbors for $5f$ shell only. In inset: the ratio V/t_{ff} as function of atomic number.

5.4 Comparison with earlier parametrization of W. A. Harrison

In this section we compare our tight-binding parametrization for actinides with earlier reported in literature by W. A. Harrison [99]. The evaluation will be carried out on the example of Cm. The discussion will consist of three parts focusing on hybridization parameters V, $f-f$ hoppings t^f and matrix elements of spin-orbit coupling.

The ultimate idea which W. Harrison has been trying to develop for many d- and f-shell compounds and alloys is a formulation of tight-binding theory with

universal parameters [119]. Indeed, within this theory one could make direct elementary estimates of all the bonding properties without the addition of empirical parameters.

Eventually, the Hamiltonian to be considered:

$$H_{Harrison} = \sum_{\mathbf{k}} \epsilon_{\mathbf{k}} c^{\dagger}_{\mathbf{k}} c_{\mathbf{k}} + \sum_{im} \epsilon_{fm} f^{\dagger}_{im} f_{im} + H_{SO} + \sum_{\mathbf{k},im} (V_{\mathbf{k}im} c^{\dagger}_{\mathbf{k}} f_{im} + c.c.) + \sum_{\langle ij \rangle mm'} t^{f}_{mm'} f^{\dagger}_{im} f_{jm'} \tag{5.4.2}$$

where $c_{\mathbf{k}}$ and f_{im} are annihilation operators for the conduction electron in state $|\mathbf{k}\rangle$ and $5f$-electron with magnetic number m at site i correspondingly. ϵ_{fm} are on-site energies for $5f$-electrons and $\epsilon_{\mathbf{k}}$ is spectrum of conduction electrons. $V_{\mathbf{k}}, im$ stands for the hybridization matrix elements of local $5f$- and conduction electrons.

We will compare parameters $V_{\mathbf{k},im}$, $t^{f}_{mm'}$ and matrix elements of H_{SO} reported by W. Harrison with values calculated in this study in subsequent Sections 5.4.1, 5.4.2 and 5.4.3 correspondingly.

W. Harrison assumes $f - f$ hoppings by magnitude to be much smaller than hybridization parameters and starts with model 5.4.2 where $t^{f}_{mm'} = 0$. Then he calculates $t^{f}_{mm'}$ using second order perturbation theory with respect to hybridization.

5.4.1 Hybridization parameters

The calculation of $t^{f}_{mm'}$ is carried out within second-order perturbation theory:

$$t^{f}_{mm'} = \langle f'_{0m} | H | f_{im'} \rangle = \sum_{\mathbf{k}} \frac{V^{*}_{\mathbf{k},0m} V_{\mathbf{k},jm'}}{\epsilon_f - E_{\mathbf{k}}}, \tag{5.4.3}$$

where site j is first nearest neighbor of central site. The hybridization parameters:

$$V_{\mathbf{k},im} = \langle \mathbf{k} | \Delta | f_{im} \rangle, \tag{5.4.4}$$

where state $|\mathbf{k}\rangle$ is written as orthogonalized plane wave (OPW) (for details of construction see Ref. [119]) and expanded in spherical harmonics and spherical

Bessel functions around the atomic nuclei. The perturbation Δ which couples this OPW to the atomic f state arises from the difference in the potential δV between the metal and what it would be in the free atom. Further, W. Harrison proceeds with atomic sphere approximation taking the potential to be atomic within muffin-tin sphere and ϵ_f outside. Then the difference $\delta V = 0$ inside the muffin-tin sphere and $\epsilon_f - V_{atomic}(\mathbf{r})$ outside.

With the given assumptions, the angular integration in 5.4.4 gives:

$$\langle \mathbf{k}|\Delta|f,m\rangle = \frac{4\pi}{\sqrt{\Omega}} Y_3^m(\theta_k,\varphi_k) \int j_3(kr)\Delta R_{n3} r^2 dr, \tag{5.4.5}$$

where R_{n3} is the radial f-state wave function. The angles (θ_k, φ_k) parameterize the direction of the $\mathbf{k}$-vector in Brillouin zone. The last simplification considers the fact that f-state is strongly localized and then $j_3(kr) \approx (kr)^3$.

The final form of the hybridization:

$$\langle \mathbf{k}|\Delta|f,m\rangle = \left(\frac{4\pi r_f^3}{\sqrt{3\Omega}}\right)^{1/2} \frac{\hbar^2 k^2}{m} k r_f Y_3^m(\theta_k,\varphi_k) \int j_3(kr)\Delta R_{n3} r^2 dr, \tag{5.4.6}$$

where r_f depends only upon the atomic f state.

We argue that formula 5.4.6 does not reflect the actual symmetry of hybridization in actinides. We consider the following expansion:

$$V^L_{\mathbf{k},0m} = \sum_{l'm'} a^L_{ml'm'} Y_{l'}^{m'}(\theta_k,\varphi_k), \tag{5.4.7}$$

where V acquired additional index L to distinguish s, p and d characters of conduction electrons. If Equation 5.4.6 holds then coefficients a with $l' = 3$ will be much bigger than those with $l' \leq 2$.

To extract coefficients $a^L_{ml'm'}$ we multiply 5.4.7 by $[Y_{l''}^{m''}(\theta_k,\varphi_k)]^*$ and sum over Brillouin zone. This gives the following expression for coefficients:

$$a^L_{ml''m''} = \frac{\sum_{\mathbf{k}} V^L_{\mathbf{k},0m}[Y_{l''}^{m''}(\theta_k,\varphi_k)]^*}{\sum_{\mathbf{k}}[Y_{l''}^{m''}(\theta_k,\varphi_k)]^* Y_{l''}^{m''}(\theta_k,\varphi_k)} \tag{5.4.8}$$

In expansion 5.4.7 we included spherical harmonics with $l \leq 3$. The partial contribution of different harmonics to hybridization of $7s$- and $5f$-orbitals are

presented in Figure 5.8. Figure 5.9 represents the partial contribution of different spherical harmonics to the hybridization of $6d$ with $l = -1$ and $5f$ orbitals.

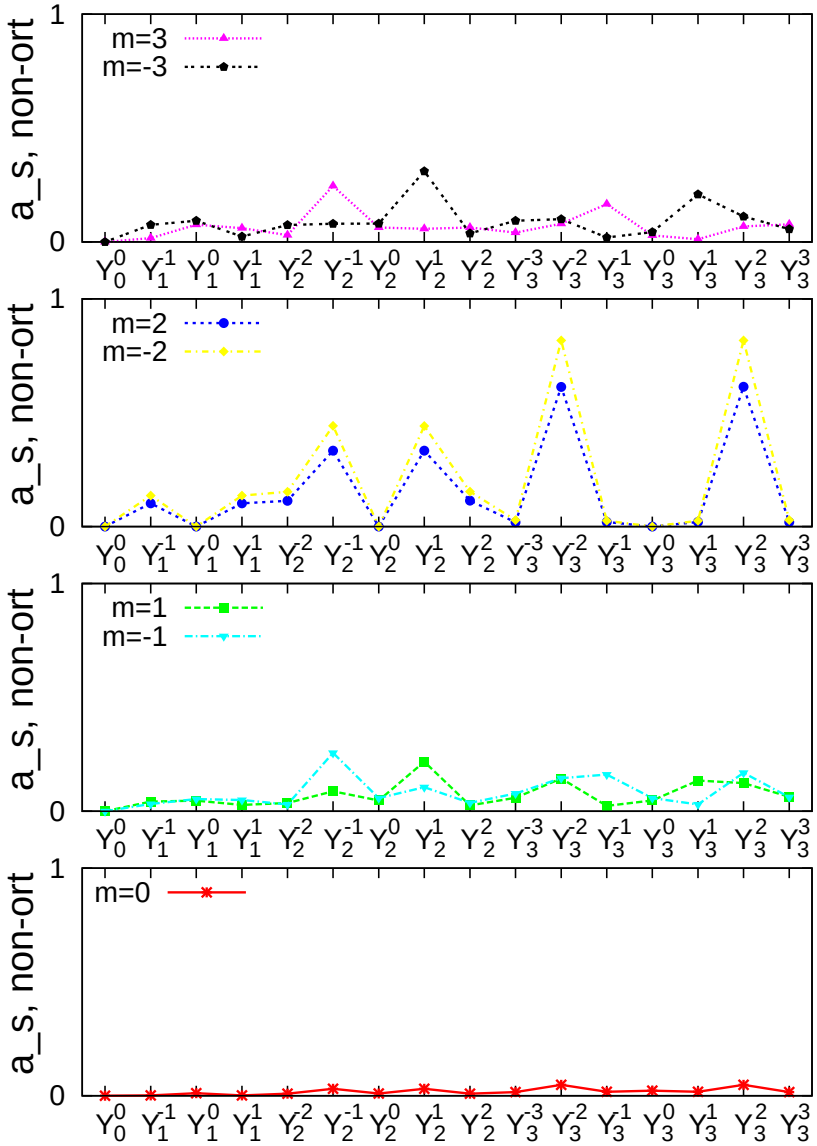

Figure 5.8: Partial contributions of spherical harmonics into s-f hybridization matrix element.

As can be observed independently of the character of $5f$-orbital one of the biggest contributions into s-f hybridization comes from $Y_3^2(\hat{\mathbf{k}})$ and $Y_3^{-2}(\hat{\mathbf{k}})$. We will provide additional qualitative reasons for such behavior in next section.

We conclude that the symmetry of hybridization in our parametrization differs from the one assumed by W. Harrison.

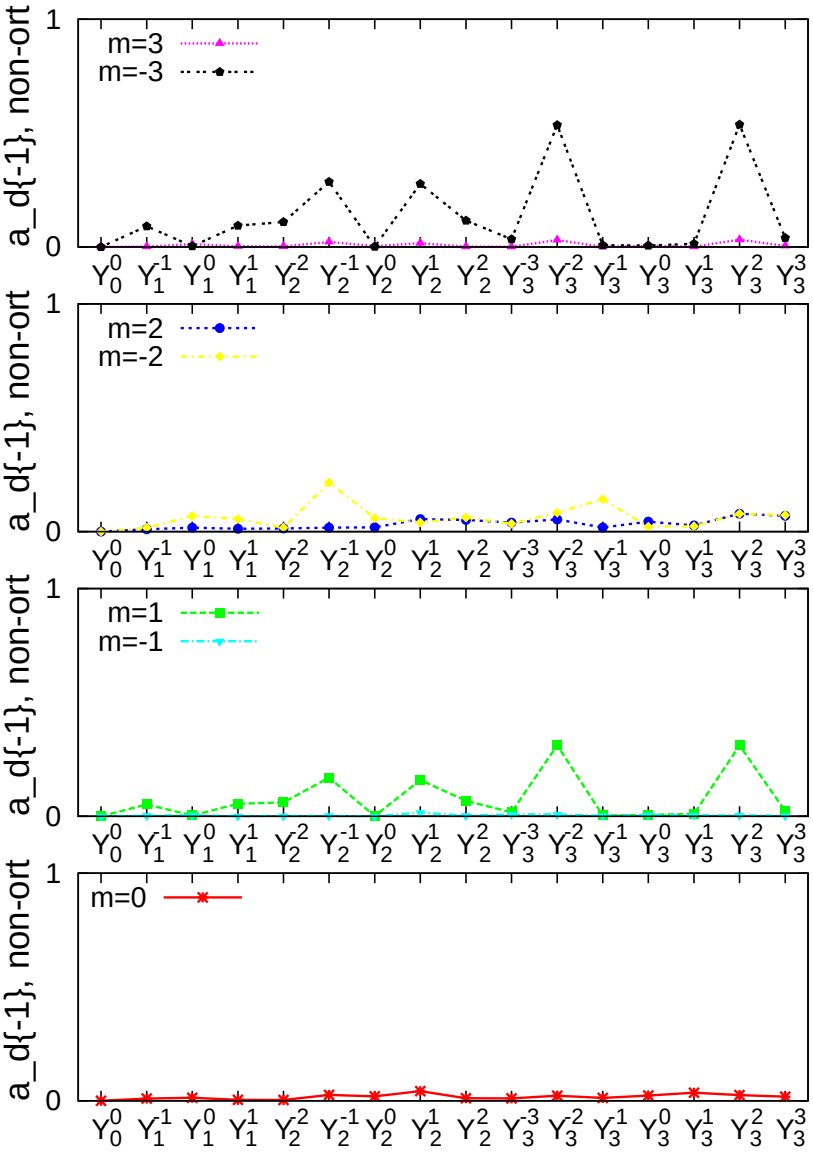

Figure 5.9: Partial contributions of spherical harmonics into $d_{\{l=-1\}}$-f hybridization matrix element.

5.4.2 $f - f$ hoppings

Finally, in the perturbation-theoretical expansion 5.4.3 one assumes the denominator to be equal to $\hbar^2 k^2/(2m)$. After integration, 5.4.3 becomes (for details of integration see [120]):

$$t_m^f = \eta_{ffm}\hbar^2 r_f^5/md^7, \tag{5.4.9}$$

with

$$\eta_{ff\sigma} = 20(525/2\pi), \quad \eta_{ff\delta} = 6(525/2\pi), \tag{5.4.10}$$
$$\eta_{ff\pi} = -15(525/2\pi), \quad \eta_{ff\varphi} = -(525/2\pi).$$

Here d is scaling parameter.

W. Harrison provides generic forms for V_{lfm}:

$$V_{dfm} = \eta_{dfm}\hbar^2(r_d^3 r_f^5)^{1/2}/md^6, \tag{5.4.11}$$
$$V_{s,pfm} = \eta_{s,pfm}\hbar^2 r_f^{5/2}/md^{9/2},$$

but does not give the values for coefficients η_{lfm}.

In order to compare given t_m^f parameters to ours, we rewrote Tables 5.1 and 5.2 in LS-representation in Table 5.10.

We calculate t_m^f for each type of bond as:

$$\tilde{t}_m^f = \frac{1}{2}\sqrt{Tr\,[V_m^T V_m]}, \tag{5.4.12}$$

where V_m is matrix 2×2 consisting of t_m^f parameters with m and $-m$ indexes of Table 5.10 within the block with spin up.

We will comment on the relative importance of σ-, π-, δ- and φ-bonding rather than on absolute value of parameters because of the presence of scaling parameters r_f and d. Calculations of W. Harrison suggest that σ-bonding dominates all other types of bonding, π- is stronger than δ-bond which in turn stronger than φ-bond.

The values at Table 5.11 suggest that the symmetry of $f-f$ hopping reported by W. Harrison is not consistent with one reported in this study. Our calculations show δ-bonding is a dominant type of bonding among $5f$-orbitals. σ-bonds are also favored while π- and φ-bonds give a much smaller contribution.

Also, our calculation show that matrix elements among spherical harmonics with different m are of the same order of magnitude as those with the same m, and

Table 5.10: Nearest neighbors parametrization for Cm II in spherical harmonics in LS-base.

	$5f_{\uparrow}\{-3\}$	$5f_{\uparrow}\{-2\}$	$5f_{\uparrow}\{-1\}$	$5f_{\uparrow}\{0\}$	$5f_{\uparrow}\{1\}$	$5f_{\uparrow}\{2\}$	$5f_{\uparrow}\{3\}$
$7s_{\uparrow}\{0\}$	-51.242	-0.000	82.640	-0.000	84.944	0.000	-55.956
$6p_{\uparrow}\{-1\}$	-1.498	-0.006	-18.657	-0.059	27.507	0.049	11.895
$6p_{\uparrow}\{0\}$	0.367	-42.625	0.364	27.314	-0.368	-45.087	-0.397
$6p_{\uparrow}\{1\}$	18.035	-0.174	48.742	0.115	-36.610	-0.136	-1.346
$6d_{\uparrow}\{-2\}$	21.843	0.000	37.367	-0.000	75.381	0.000	-35.913
$6d_{\uparrow}\{-1\}$	0.000	-26.436	-0.000	-33.916	-0.000	-127.919	0.000
$6d_{\uparrow}\{0\}$	65.768	0.000	43.346	0.000	45.536	-0.000	73.308
$6d_{\uparrow}\{1\}$	-0.000	-121.468	0.000	-34.599	0.000	-28.698	-0.000
$6d_{\uparrow}\{2\}$	-33.769	-0.000	74.849	0.000	40.027	-0.000	25.396
$5f_{\uparrow}\{-3\}$	-5.161	-0.066	5.513	-0.018	-21.509	-0.108	-8.459
$5f_{\uparrow}\{-2\}$	-0.066	-5.841	-0.116	2.053	0.237	41.604	0.112
$5f_{\uparrow}\{-1\}$	5.513	-0.116	2.666	0.147	-8.453	-0.247	-22.987
$5f_{\uparrow}\{0\}$	-0.018	2.053	0.147	-21.432	-0.150	2.114	0.024
$5f_{\uparrow}\{1\}$	-21.509	0.237	-8.453	-0.150	2.584	0.124	6.248
$5f_{\uparrow}\{2\}$	-0.108	41.604	-0.247	2.114	0.124	-7.071	0.076
$5f_{\uparrow}\{3\}$	-8.459	0.112	-22.987	0.024	6.248	0.076	-6.480

Table 5.11: Comparison of t^f_m/t^f_φ.

	$\lvert t^f_\sigma/t^f_\varphi\rvert$	$\lvert t^f_\pi/t^f_\varphi\rvert$	$\lvert t^f_\delta/t^f_\varphi\rvert$
W. Harrison[99]	20.0	15.0	6.0
present study	3.001	3.280	4.092

Table 5.12: Nearest neighbors parametrization for Cm II in cubic harmonics in LS-base.

	x(5x2-3)$_\uparrow$	y(5y2-3)$_\uparrow$	z(5z2-3)$_\uparrow$	y(x2-z2)$_\uparrow$	z(x2-2)$_\uparrow$	x(y2-z2)$_\uparrow$	xyz$_\uparrow$
7s{s}$_\uparrow$	3.633	0.351	-0.000	0.026	0.000	-0.754	4.589
6p{x}$_\uparrow$	27.314	-0.000	-0.124	0.000	0.177	62.021	19.727
6p{y}$_\uparrow$	-0.000	-17.131	-3.502	0.000	39.642	-0.000	-0.047
6p{z}$_\uparrow$	0.110	-3.460	27.314	39.772	-62.021	-0.740	0.000
6d{yz}$_\uparrow$	-2.396	0.000	0.044	0.000	0.149	1.970	4.356
6d{zx}$_\uparrow$	0.000	4.098	0.483	0.412	-2.094	0.000	0.416
6d{xy}$_\uparrow$	0.233	2.903	1.674	-0.903	-3.521	-0.062	0.000
6d{x2-y2}$_\uparrow$	0.421	-0.034	-0.000	-0.093	-0.000	1.693	-0.554
6d{3z2-1}$_\uparrow$	-3.267	-0.313	-0.000	0.453	0.000	4.489	-2.883
5f{x(5x2-3)}$_\uparrow$	-21.432	-0.000	-0.152	0.000	0.079	-2.947	29.600
5f{y(5y2-3)}$_\uparrow$	-0.000	-26.958	41.868	0.000	16.260	-0.000	-0.106
5f{z(5z2-3)}$_\uparrow$	-0.152	41.868	-21.432	16.270	2.947	-0.147	-0.000
5f{y(x2-z2)}$_\uparrow$	0.000	0.000	16.270	6.851	35.540	0.000	-0.073
5f{z(x2-2)}$_\uparrow$	0.079	16.260	2.947	35.540	35.148	0.397	0.000
5f{x(y2-z2)}$_\uparrow$	-2.947	-0.000	-0.147	0.000	0.397	35.148	0.082
5f{xyz}$_\uparrow$	29.600	-0.106	-0.000	-0.073	0.000	0.082	-48.060

so cannot be omitted. These type of matrix elements have not been considered in [99] that also reflects the wrong symmetry of hybridization.

To visualize the domination of δ-bonds we will transform TB-parametrization into cubic harmonics. Let us remind that cubic harmonics which reflect symmetry of the crystal are connected to spherical in the following way [58]:

$$\begin{aligned}
Y_{3,0}(\theta,\varphi) &\rightarrow z(5z^2-3)\\
Y_{3,1}(\theta,\varphi) \pm Y_{3,-1}(\theta,\varphi) &\rightarrow x(5x^2-3),\ \ y(5y^2-3)\\
Y_{3,2}(\theta,\varphi) \pm Y_{3,-2}(\theta,\varphi) &\rightarrow z(x^2-y^2),\ \ xyz\\
Y_{3,3}(\theta,\varphi) \pm Y_{3,-3}(\theta,\varphi) &\rightarrow y(x^2-z^2),\ \ x(y^2-z^2).
\end{aligned}$$

Now we can recalculate nearest neighbors parametrization in LS-base presented in Table 5.10 in the representation of cubic harmonics(see Table 5.12).

In Table 5.12 the biggest matrix element among $5f$-block is one between xyz

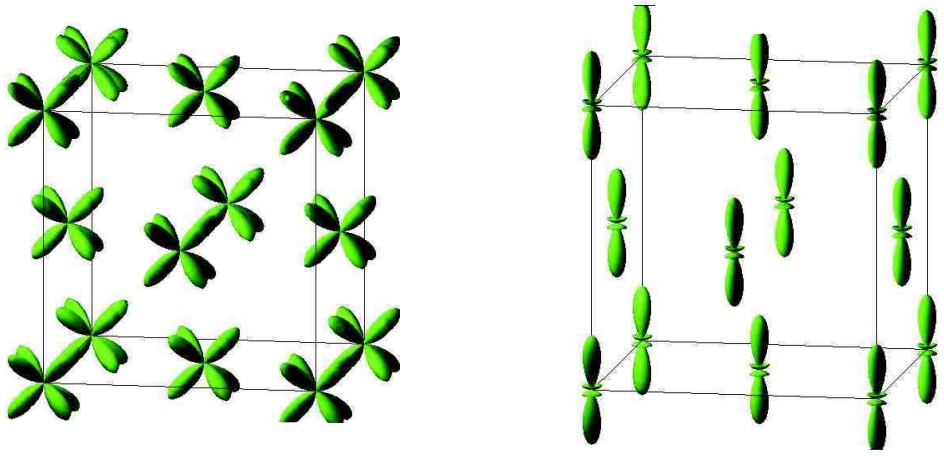

Figure 5.10: The xyz(left) and $z(5z^2-3)$(right) cubic f orbitals in fcc unit cell. The geometry of the unit cell suggests that δ-bonds formed by xyz orbitals dominate over σ-bonds formed by $z(5z^2-3)$ orbitals

orbitals of different sites and correspond to δ-type of bonding. The matrix element corresponding to σ is twice as small. The visual and intuitive demonstration for this observation is shown in Figure 5.10. Indeed, the geometry of unit cell suggests that δ-bonding must be stronger than σ-bonding.

5.4.3 Matrix elements of spin-orbit coupling

The other point considered in [99] was the incorporation of spin-orbit coupling into intra-atomic matrix elements. W. Harrison treats spin-orbit coupling as a one-electron effect:

$$H_{SO} = \frac{1}{2m^2c^2}\frac{1}{r}\frac{\partial V}{\partial r}\vec{l}\cdot\vec{\sigma}, \tag{5.4.13}$$

where $V(r)$ is the spherically symmetric potential seen by the electron, and $\vec{l}$ and $\vec{\sigma}$ are the orbital and spin angular momentum operators. The corresponding matric elements for $\vec{l}\cdot\vec{\sigma}$ can be rewritten in terms of total angular momentum operator $\vec{j}=\vec{l}+\vec{\sigma}$ as:

$$\vec{l}\cdot\vec{\sigma} = (\vec{j}^2 - \vec{l}^2 - \vec{\sigma}^2)/2. \tag{5.4.14}$$

The corresponding one-electron eigenstates for free-atom have eigenvalues:

$$\vec{l}\cdot\vec{\sigma} = \hbar^2[j(j+1) - 3(3+1) - \frac{1}{2}(\frac{1}{2}+1)], \tag{5.4.15}$$

Table 5.13: On-site parametrization for Cm II in jj-base for $j = 5/2$ (in meV).

5f::	$\|\frac{5}{2},-\frac{5}{2}\rangle$	$\|\frac{5}{2},-\frac{3}{2}\rangle$	$\|\frac{5}{2},-\frac{1}{2}\rangle$	$\|\frac{5}{2},\frac{1}{2}\rangle$	$\|\frac{5}{2},\frac{3}{2}\rangle$	$\|\frac{5}{2},\frac{5}{2}\rangle$
$5f :: \|\frac{5}{2},-\frac{5}{2}\rangle$	-1148.744	0.000	-0.000	0.000	-3.759	0.000
$5f :: \|\frac{5}{2},-\frac{3}{2}\rangle$	0.000	-1142.020	0.000	0.000	0.000	-3.759
$5f :: \|\frac{5}{2},-\frac{1}{2}\rangle$	-0.000	0.000	-1150.425	0.000	-0.000	-0.000
$5f :: \|\frac{5}{2},\frac{1}{2}\rangle$	0.000	0.000	0.000	-1150.425	0.000	-0.000
$5f :: \|\frac{5}{2},\frac{3}{2}\rangle$	-3.759	0.000	-0.000	0.000	-1142.020	0.000
$5f :: \|\frac{5}{2},\frac{5}{2}\rangle$	0.000	-3.759	-0.000	-0.000	0.000	-1148.744

Table 5.14: On-site parametrization for Cm II in jj-base for $j = 7/2$(in meV).

5f::	$\|\frac{7}{2},-\frac{7}{2}\rangle$	$\|\frac{7}{2},-\frac{5}{2}\rangle$	$\|\frac{7}{2},-\frac{3}{2}\rangle$	$\|\frac{7}{2},-\frac{1}{2}\rangle$	$\|\frac{7}{2},\frac{1}{2}\rangle$	$\|\frac{7}{2},\frac{3}{2}\rangle$	$\|\frac{7}{2},\frac{5}{2}\rangle$	$\|\frac{7}{2},\frac{7}{2}\rangle$
$5f :: \|\frac{7}{2},-\frac{7}{2}\rangle$	239.472	-0.000	-0.000	0.000	-19.444	0.000	-0.000	0.000
$5f :: \|\frac{7}{2},-\frac{5}{2}\rangle$	-0.000	246.196	0.000	-0.000	0.000	5.606	0.000	-0.000
$5f :: \|\frac{7}{2},-\frac{3}{2}\rangle$	-0.000	0.000	252.669	-0.000	0.000	0.000	5.606	-0.000
$5f :: \|\frac{7}{2},-\frac{1}{2}\rangle$	0.000	-0.000	-0.000	232.899	0.000	-0.000	0.000	-19.444
$5f :: \|\frac{7}{2},\frac{1}{2}\rangle$	-19.444	0.000	0.000	0.000	232.899	0.000	-0.000	-0.000
$5f :: \|\frac{7}{2},\frac{3}{2}\rangle$	0.000	5.606	0.000	-0.000	0.000	252.669	-0.000	0.000
$5f :: \|\frac{7}{2},\frac{5}{2}\rangle$	-0.000	0.000	5.606	0.000	-0.000	-0.000	246.196	0.000
$5f :: \|\frac{7}{2},\frac{7}{2}\rangle$	0.000	-0.000	-0.000	-19.444	-0.000	0.000	0.000	239.472

with $j = 5/2$ and $j = 7/2$, leading to diagonal in jj-representation matrix elements of H_{SO}, $-2V_{SO}$, and $3V_{SO}/2$, respectively. Particularly, for Cm W. Harrison provides $V_{SO} = 0.39$ eV. This fixes matrix elements of H_{SO} to be -780 meV and 585 meV.

The on-site parametrization derived here for the spin-orbit matrix elements is consistent with that suggested by W. Harrison atomic-like picture. Tables 5.13 and 5.14 list the on-site matrix elements for $5f$-block within the jj-representation for $j = 5/2$ and $j = 7/2$ correspondingly. Both tables have a diagonal shape with average diagonal values to be $\approx$ -1150 meV and 250 meV for $j = 5/2$ and $j = 7/2$ correspondingly, giving raise for spin-orbit splitting of 1.4 eV. This number is in good agreement with value of 1.19 eV predicted by W. Harrison.

5.5 Conclusion

In this chapter we performed real space analysis of electronic structure of actinides. We showed that $5f$-orbitals in this class of materials extend just enough to overlap. Hence, the low energy physics of actinides is ruled by nearest neighbor hoppings. We also provide tight-binding parametrization for chosen actinides and compare it to the one reported earlier in literature by W. Harrison. The tight-binding parametrization obtained here agrees with reported by W. Harrison on spin-orbit coupling matrix elements. However, we have shown that the symmetry of both $f - f$ hoppings and hybridization is completely different than assumed by W. Harrison.

Chapter 6

Calculation of magnetic exchange constants and Néel Temperature for Curium metal

Available up-to-date experimental data suggest curium to be the element with the smallest atomic number among actinides to develop a macroscopic magnetic moment. In this chapter we calculate the magnetic coupling parameters for fcc curium by mapping LSDA total energies of different magnetic arrangements onto a Heisenberg model. Within the framework of semiclassical molecular field theory we calculate the Néel temperature for fcc Cm and compare it to the experimental value.

6.1 Review of experimental data on magnetic properties of Curium

The very early magnetic studies of curium are summarized and reported in the review by M. B. Brodsky [13] devoted to magnetic properties of metallic actinides. At that time only two first high-pressure modifications of curium were known, namely dhcp and fcc phases. M. Brodsky presents susceptibility curves reported by different groups at the same year (1976). These curves are shown in Figure 6.1.

The data were collected for stable phases between ~ 2 and 300 K. In both cases Curie-Weiss temperature dependence were found. The first group of Kanellakopulos *et al.* observed antiferromagnetic behavior with Neel temperature around 50 K [121]. The other group of Fujita *et al.* was able measure susceptibility

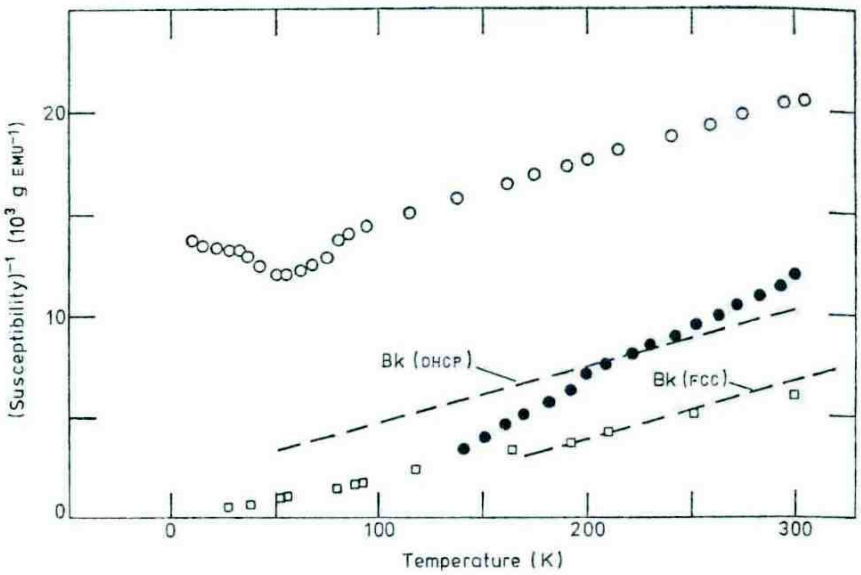

Figure 6.1: Inverse Magnetic susceptibility, the plot is taken from review by M. B. Brodsky [13].

only in paramagnetic region [122]. Also Fujita *et al.* reported the effective moment to be $7.8 \div 8.1\ \mu_B$ [122], which is in fair agreement with Russel-Saunders values of $7.7\ \mu_B$ ($5f^7$). Russel-Saunders numbers are free-ion effective magnetic moment values predicted by L-S coupling and Hunds rule. Thus, it points to the conclusion that J must be a good quantum number for heavy actinides. Fujita concludes that for Cm and Bk (next after Cm in periodic table) the $5f$ electron do not form bands and the magnetic effects will be the same as the heavy rare earths and not the $3d$ transition metals or light actinides.

The deepest investigation of the magnetic properties of curium metal is reported by P. G. Huray *et al.* in [15]. Huray used a SQUID-based micromagnetic susceptometer to determine the magnetic susceptibility of ^{248}Cm metal in the temperature range $4.2 - 340K$ and in the applied magnetic field range of 0.45-1400 G. In the investigation they used samples of two types: with dhcp and fcc structures.

Huray *et al.* report that dhcp samples exhibit an antiferromagnetic transition at $\approx$ 65K. A small second transition in the neighborhood of 200 K is observed and influences the high-temperature Curie-Weiss fit to the data.

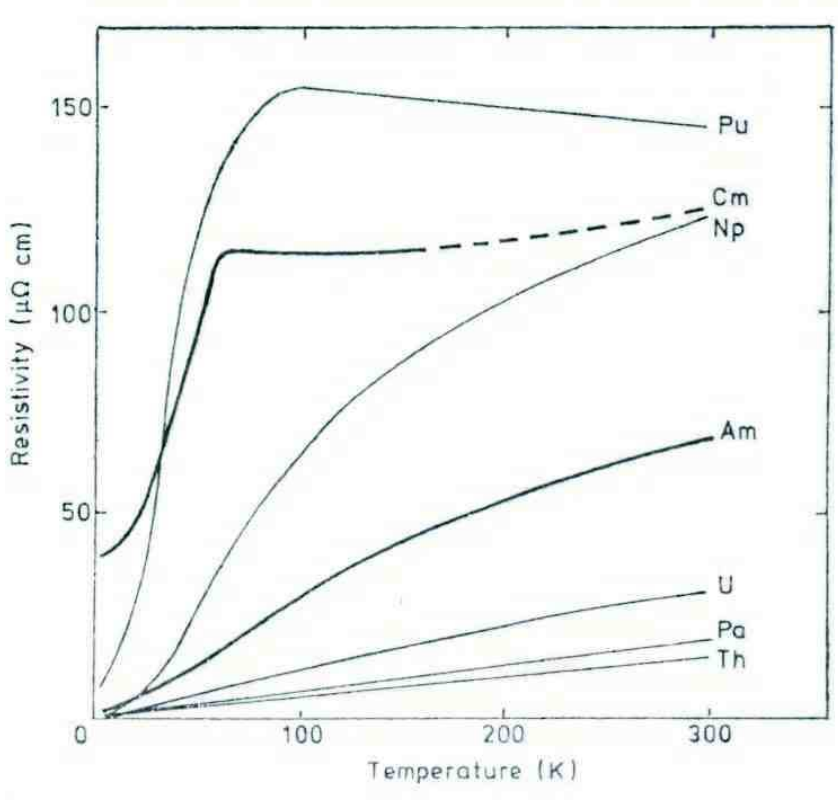

Figure 6.2: Electrical resistivity of pure actinides. Cm data of Schenkel [14].

They showed that the fcc phase exhibits a ferrimagnetic transition in the neighborhood of 200 K and at low temperature has a saturated magnetic moment per atom of 0.4 Bohr magnetons in applied fields above 1200 G. In Figure 6.3 the effective magnetic moment per atom is plotted. Huray *et al.* emphasize that the saturation moment is seen to be field dependent in this region but the changes are becoming smaller at high fields.

In the high temperature regime the susceptibility showed little field dependence, as is seen in Figure 6.4. Here $1/\chi$ is plotted vs. T for several applied fields.

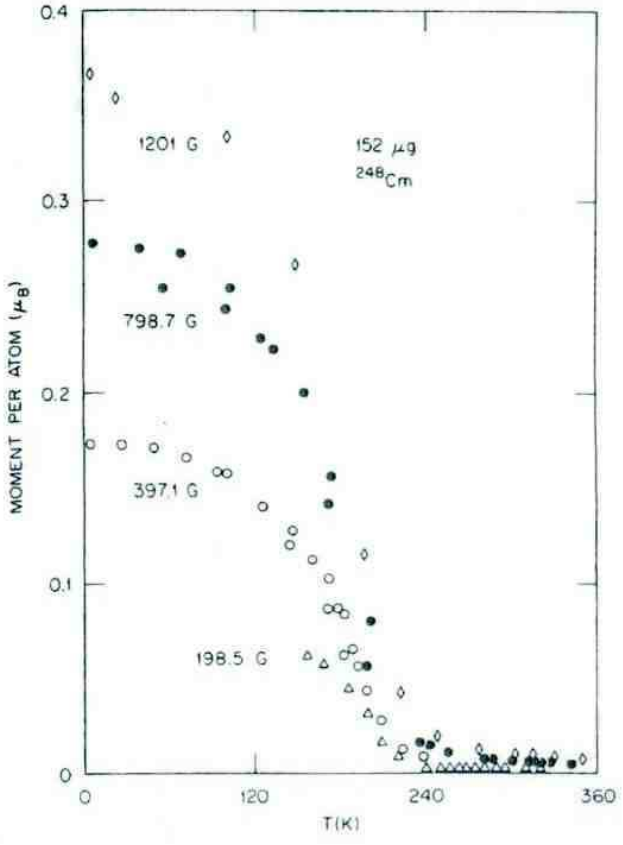

Figure 6.3: Effective magnetic moment per atom vs. temperature for an fcc sample.

Huray *et al.* notice that the curvature of shown data prevents a Curie-Weiss interpretation for all temperatures, so they examined two regions differently:

$$\mu = 6.2\mu_B, \;\; \theta = -202K \;\; for \;\; 200K < T < 300K, \tag{6.1.1}$$
$$\mu = 7.7\mu_B, \;\; \theta = -138K \;\; for \;\; 300K < T < 340K.$$

π

Since the low-temperature data suggest ferrimagnetism, authors also fit the high-temperature variation of $1/\chi$ vs. T with the function of the form:

$$\chi = \frac{(C_1 + C_2)T - 2\lambda C_1 C_2}{T^2 - T_N^2}, \tag{6.1.2}$$

with $C_i = N\mu_i^2/6k$ and μ_i constrained $= \mu \pm 0.4\mu_B$ (for fitting they used results of molecular field model, see Appendix A for details). Here C_i are separate Curie

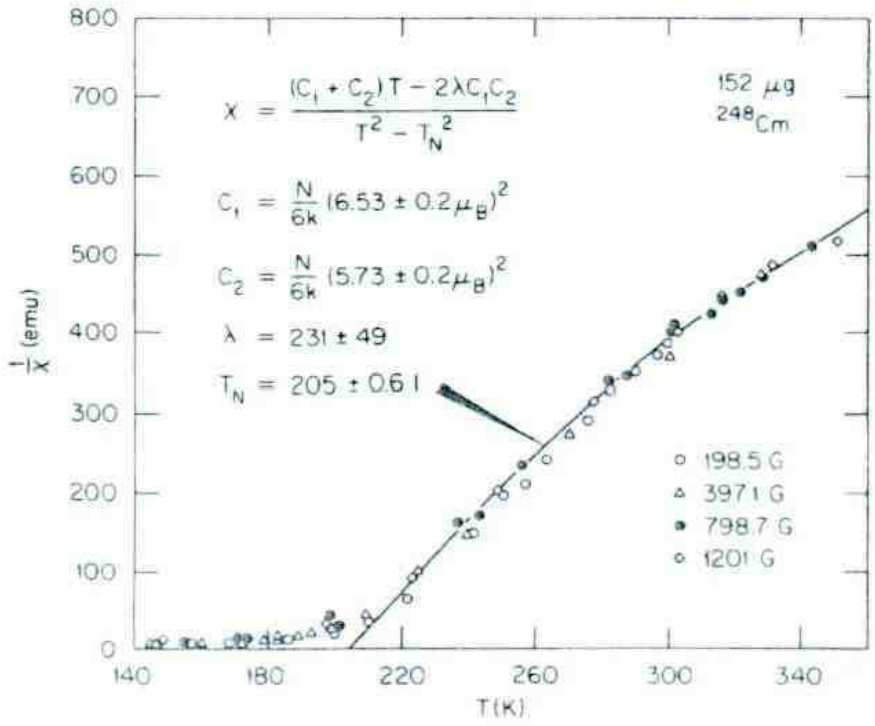

Figure 6.4: The inverse magnetic susceptibility vs. temperature for several applied fields (plot is taken from [15]).

constants for two spin lattices. λ is defined through $H_1 = H - \lambda M_2$, where H is the applied field and M_2 is the magnetization of the second sublattice. T_N is the ferrimagnetic Néel temperature. It should be mentioned that two sites are assumed to have moments different by $0.8\mu_B$ in order that the average moment per atom is $0.4\mu_B$ at $4.2K$. The fit to the data here has the smallest sum of squares and yields:

$$\lambda = 231 \pm 49, \;\; \mu = 6.13 \pm 0.2\mu_B, \;\; T_N = 205 \pm 0.6K. \qquad (6.1.3)$$

6.2 Exchange constants for fcc Curium.

The method we will use for calculation of exchange parameters was reported by J. Kuneš *et al.* [123]. Our objective is to determine the nearest neighbors coupling parameter J_1 and next nearest neighbors coupling parameter J_2 (see Figure 6.5 for the schematic presentation). The idea is to calculate total energies for different magnetic arrangements and map them to the energies corresponding

to the Heisenberg model:

$$H = -\sum_{i,j} J_{ij}\mathbf{S}_i\mathbf{S}_j, \tag{6.2.4}$$

with nearest-neighbor J_1 and next-nearest-neighbor J_2 interactions.

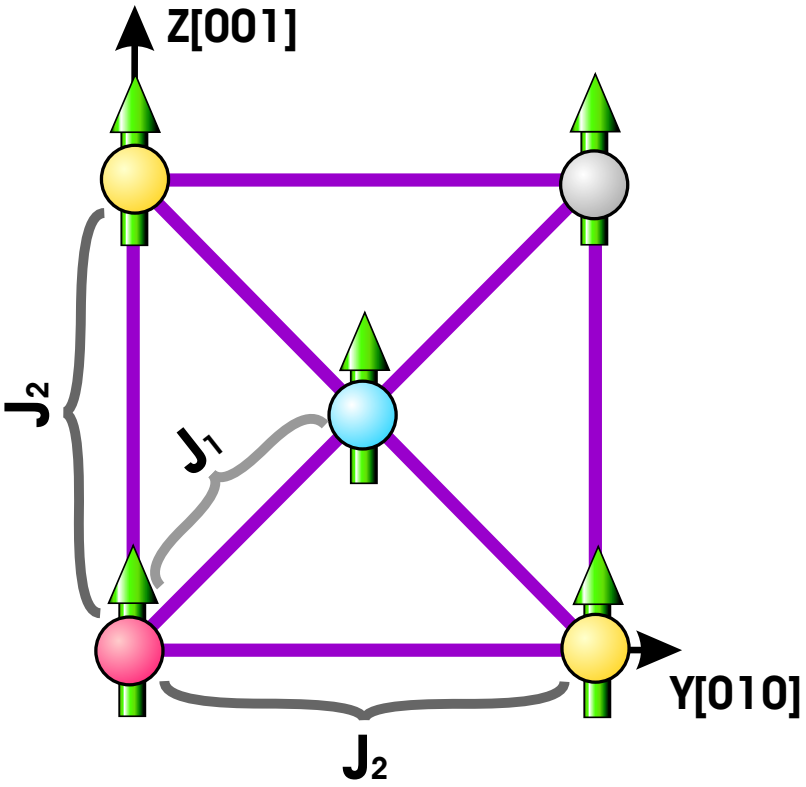

Figure 6.5: The sheme shows that we denoted by J_1 exchange constant between nearest neighbors and by J_2 the exchange constant between next nearest neighbors.

To obtain a system of two equations for unknowns J_1 and J_2 one needs to use at least three different magnetic arrangements, since these are only total energy differences which can enter, not total energies by themselves. We consider following magnetic arrangements:

1. antiferromagnetic with propagation vector $(0,0,\frac{2\pi}{a})$,

2. type II antiferromagnetic.

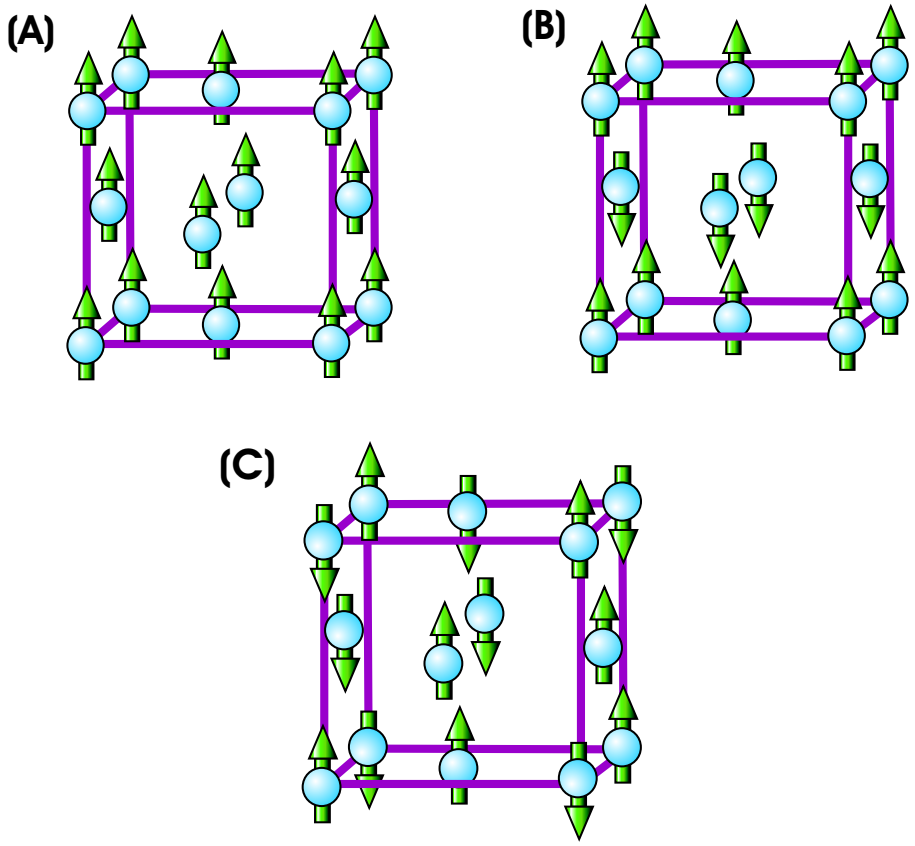

Figure 6.6: Different magnetic arrangements for fcc crystal structure used in calculations: (A) ferromagnetic; (B) antiferromagnetic; (C) type II antiferromagnetic.

3. ferromagnetic corresponding to antiferromagnetic with propagation vector $(0,0,\frac{2\pi}{a})$,

4. ferromagnetic corresponding to type II antiferromagnetic

Here a is lattice parameter. The corresponding magnetic arrangements for fcc crystal structure are shown in Figure 6.6. The classical ground state energies of these magnetic configurations mapped on Heisenberg Hamiltonian corresponding to spin configurations (1)-(4) are:

1. $E_{AF} = (4J_1 - 6J_2)S^2$,

2. $E_{AF}^{II} = 6J_2S^2$,

3. $E_{FERR} = -(12J_1 + 6J_2)S^2$,

4. $E^{II}_{FERR} = -(12J_1 + 6J_2)S^2$,

where classical spin $S = 5/2\hbar$.

Let us introduce

$$\Delta = E_{AF} - E_{FERR},$$
$$\Delta^{II} = E^{II}_{AF} - E^{II}_{FERR}.$$

Linear system of equations for unknowns J_1, J_2 are:

$$\Delta = 16J_1S^2,$$
$$\Delta^{II} = 12(J_1 + J_2)S^2. \tag{6.2.5}$$

The solution of this system is:

$$J_1 = \frac{1}{(2S)^2}\frac{\Delta}{4}, \quad J_2 = \frac{1}{(2S)^2}\left(-\frac{\Delta}{4} + \frac{\Delta^{II}}{3}\right). \tag{6.2.6}$$

For S we use classical vale of spin $S = 5/2\hbar$.

6.3 Total Energy GGA calculations for fcc Curium

The results of total energy calculations within generalized-gradient approximation (GGA) employing ASA scheme are shown in Figure 6.7. We used $6\times6\times6$- mesh in the first Brillouin zone. There are in total 12 curves in this figure. We consider 4 different magnetic arrangements, enumerated above, and we perform calculations using 3 different LMTO basis: with $6p$ electrons treated as valent, $7p$ electrons treated as valent, and both $6p$ and $7p$ included in the basis. The other orbitals in LMTO basis are $7s$, $6d$ and $5f$.

In Figure 6.7 we see that with each LMTO basis the first type antiferromagnetic solution has the lowest total energy. The x-axis corresponds to the ratio of unit cell volume used in calculations to the experimentally measured one. The best predictions for equilibrium volume are done when one treats $7p$ electrons as

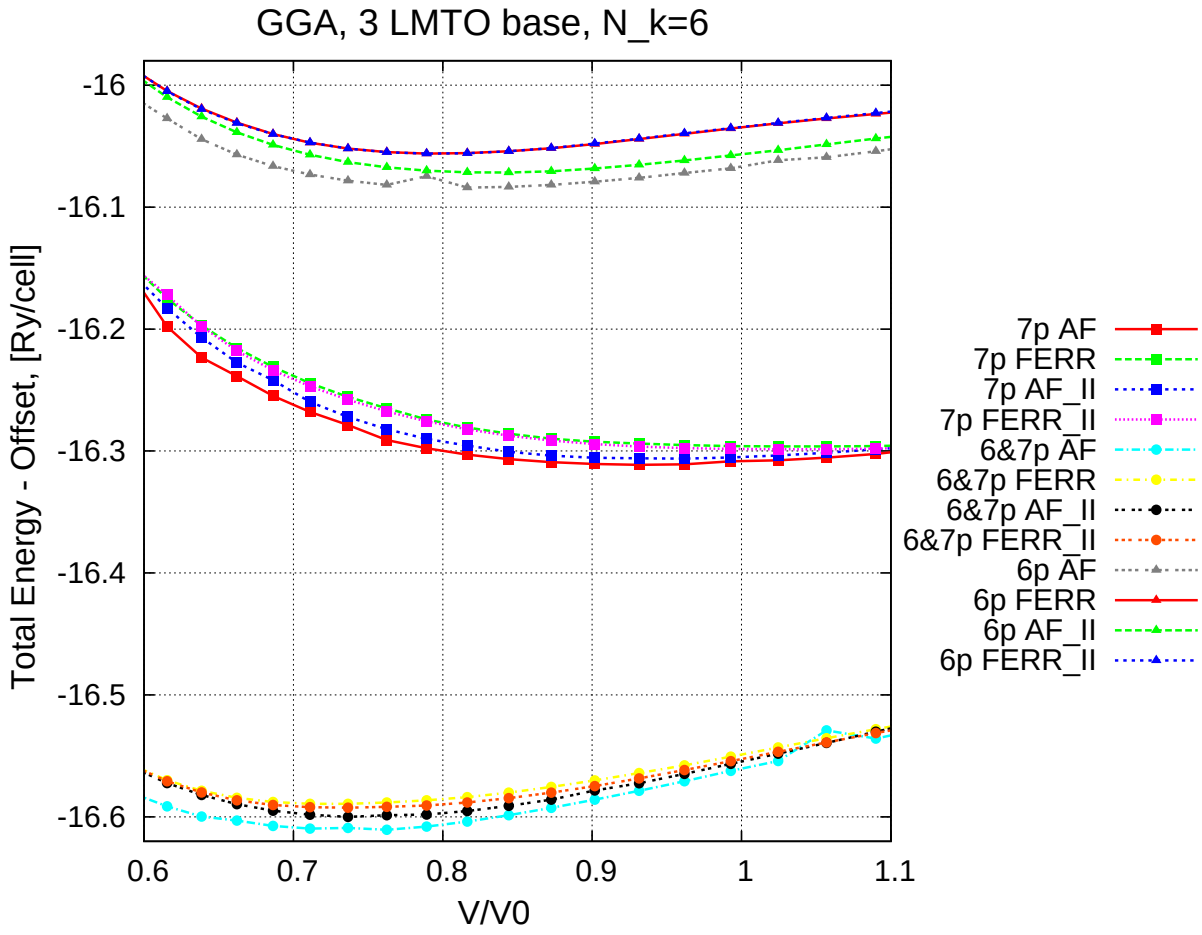

Figure 6.7: Total energy vs ratio of unit cell volume to experimentally measured one for fcc structure of curium. The calculations are performed within GGA scheme using ASA approximation.

valent. However, as will be discussed below, one will fail to predict the experimentally measured value of the Néel temperature. The basis with both $6p$ and $7p$ electrons surprisingly give s a worse predictions ($\approx 25\%$ off). The basis with $6p$ only gives slightly better predictions ($\approx 20\%$ off).

In Figure 6.8 the dependence of J_1 and J_2 parameters on the relative volume is shown obtained from calculated total energy vs relative volume curves and formulas 6.2.6. There are in total 6 curves in this plot again because we used three different LMTO base. In each base J_1 was determined to be negative and

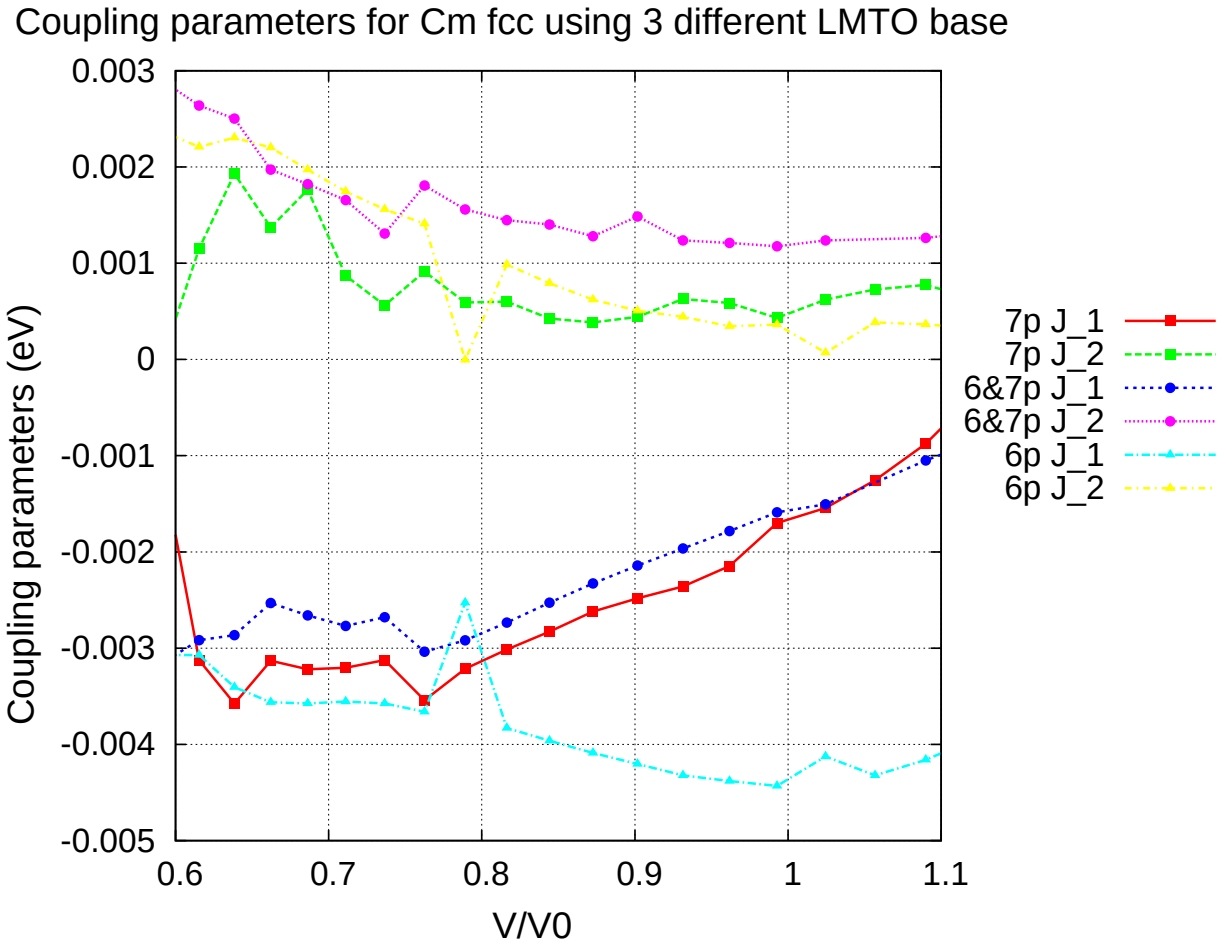

Figure 6.8: Dependence of coupling parameters J_1 and J_2 on relative volume. The same type of calculations performed with 3 different LMTO base: with $6p$ treated as valent, $7p$ treated as valent, and both $6p$ and $7p$ are included.

J_2 to be positive that reinforce the antiferromagnetism. Also J_1 and J_2 have tendency to increase in magnitude as lattice parameter becomes smaller, what also makes perfect sense. The exception is the J_1 parameter calculated within the $7p$ basis.

It is instructive to compare the calculated values of J_1 and J_2 by the order of magnitude to RKKY constants. Indeed, in RKKY model

$$J_{RKKY} \approx V^2/\epsilon_F. \tag{6.3.7}$$

The value of hybridization for fcc Cm can be taken from Table 4.6 and $V \approx$

0.192eV. Fermi energy within LDA calculations $\epsilon_F \approx 7.045$ eV. Thus, $J_{RKKY} \approx$ 0.0052eV which is of the same order of magnitude as our result for J_1 and J_2 for equilibrium volume.

6.4 Molecular Field Theory

6.4.1 Antiferromagnetism

The strong interaction which tends to align the atomic dipoles parallel or anti-parallel in magnetic materials may be considerate as equivalent to some internal magnetic field H_m [124]. Weiss in his phenomenological theory of ferromagnetism assumed that:

$$\mathbf{H}_m = N_W \mathbf{M}, \tag{6.4.8}$$

here N_W is a constant called the molecular field constant. Now, we consider an antiferromagnet with two sublattices A and B and assume that an atom at an A site has nearest neighbors that all lie on B sites and next nearest neighbors that all lie on A sites. Then, analogically, the molecular field $\mathbf{H}_{mA}$ acting on an atom at an A site:

$$\mathbf{H}_{mA} = -N_{AA}\mathbf{M}_A - N_{AB}\mathbf{M}_B, \tag{6.4.9}$$

where $\mathbf{M}_A$ and $\mathbf{M}_B$ are the magnetizations of the A and B sublattices, respectively, N_{AB} is a molecular field constant for the nearest neighbor interaction, and N_{AA} is a molecular field constant for the next nearest neighbor interaction. Similarly, the molecular field $\mathbf{H}_{mB}$ acting on an atom at a B site:

$$\mathbf{H}_{mB} = -N_{BA}\mathbf{M}_A - N_{BB}\mathbf{M}_B. \tag{6.4.10}$$

Since the same type of atoms occupy the A and B lattice sites, $N_{AA} = N_{BB} =$

N_{ii} and $N_{AB} = N_{BA}$. Then, if a field $\mathbf{H}$ is also applied, the fields:

$$\mathbf{H}_A = \mathbf{H} - N_{ii}\mathbf{M}_A - N_{AB}\mathbf{M}_B, \tag{6.4.11}$$
$$\mathbf{H}_B = \mathbf{H} - N_{AB}\mathbf{M}_A - N_{ii}\mathbf{M}_B.$$

At thermal equilibrium the magnetizations of the sublattices are given by:

$$M_{A,B} = \frac{1}{2} N g \mu_B S B_S(x_{A,B}), \tag{6.4.12}$$

where

$$x_{A,B} = \frac{S g \mu_B}{kT} H_{A,B} \tag{6.4.13}$$

and

$$B_S(x_{A,B}) = \frac{2S+1}{2S} \coth \frac{2S+1}{2S} x_{A,B} - \frac{1}{2S} \coth \frac{x_{A,B}}{2S}. \tag{6.4.14}$$

Here N is a total number of atoms with a permanent dipole moment per unit volume.

6.4.2 Behavior above the Néel temperature

Although there is no antiferromagnetic ordering above the Néel temperature, a small magnetization is induced by the applied field. For the usual values of applied field, saturation effects are negligible and Brillouin function $B_S(x)$ can be replaced by the first term of the series expansion in x in (6.4.14):

$$B_S(x) = [(S+1)/3S]x. \tag{6.4.15}$$

Then equation (6.4.12) becomes:

$$M_{A,B} = \frac{N g^2 \mu_B^2 S(S+1)}{6kT} H_{A,B}. \tag{6.4.16}$$

Now

$$H_A = |\mathbf{H} - N_{ii}\mathbf{M}_A - N_{AB}\mathbf{M}_B| = H - N_{ii}M_A - N_{AB}M_B,$$

since H, M_A, and M_B are parallel in the paramagnetic region. Similarly

$$H_A = H - N_{AB}M_A - N_{ii}M_B.$$

Then

$$M = M_A + M_B = \frac{Ng^2\mu_B^2 S(S+1)}{6kT}[2H - (N_{ii} + N_{AB})M].$$

Hence, the susceptibility

$$\chi = M/H = \frac{C}{T+\theta}, \tag{6.4.17}$$

where

$$C = \frac{Ng^2\mu_B^2 S(S+1)}{3k}$$

and

$$\theta = \frac{1}{2}C(N_{ii} + N_{AB}).$$

Since, generally, $N_{AB} > N_{ii}$, θ is positive.

Neel temperature will be given by:

$$T_N = \frac{1}{2}C(N_{AB} - N_i i), \tag{6.4.18}$$

where

$$C = \frac{Ng^2\mu_B^2 S(S+1)}{3k}. \tag{6.4.19}$$

6.5 Results: Calculation of Néel temperature

Figure 6.9 shows Neel temperatures calculated from J_1 and J_2 parameters in frameworks of molecular field theory, using rewritten in different notations formula 6.4.18:

$$T_N = \frac{1}{2}\frac{g^2 S(S+1)}{3k_B}(J_2 - J_1). \tag{6.5.20}$$

The experimental value equals $T_N = 205 \pm 0.6K$. In Figure 6.9 again three curves correspond to three different LMTO base. Neel temperature calculated with $7p$ basis never reach experimental value, however two other curves reach the experimental values approximately around experimental volume.

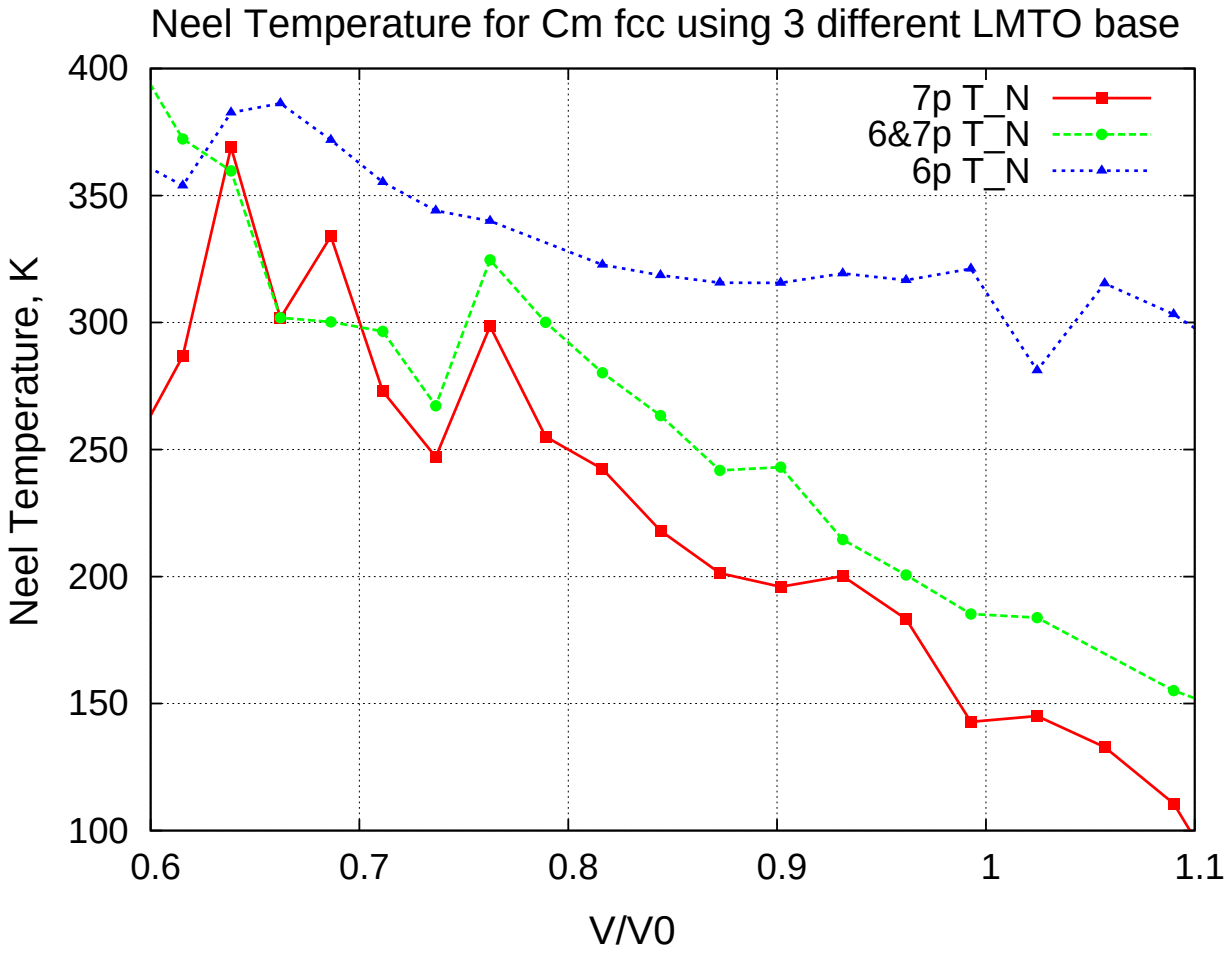

Figure 6.9: Néel temperature vs relative volume, calculated from coupling parameters J_1 and J_2 within frameworks of Molecular Field Theory.

The conclusion can be made that even if the $7p$ basis provides the best estimate for the equilibrium volume, it cannot be used to describe the magnetic properties of Cm. The other two bases ($6p$ and where both $6p$ and $7p$ are included) predict an equilibrium volume approximately 20-25 % off, but provide an excellent description of the magnetic characteristics.

6.6 Outlook: dhcp structure

The attempt has been done to perform analogical calculations of exchange constants and Néel temperature for dhcp structure. Taking into account that most of described in Section 6.1 experimental data were reported for dhcp structure.

The dhcp crystal structure is close-packed, with stacking A-B-A-C-A-B-A-C... [125], as opposed to A-B-A-B... [126] for the hcp (A3) lattice and A-B-C-A-B-C... for the fcc (A1) lattice. The (2a) crystallographic sites (the A's) form a simple hexagonal lattice. The (2c) sites (the B's and C's) form an hcp structure. The corresponding space group number is **194**($P6_3/mmc$).

Reported lattice parameters at atmospheric pressure are a =0.3502(2) nm (6.61887 a.u.) and c =1.132(2) nm (21.395899 a.u.) from [127], and a =0.3500(3) nm (6.61467a.u.) and c =1.134(1) nm (21.43159 a.u.) from [128].

Primitive Vectors:

$$\begin{aligned}
\mathbf{A1} &= \tfrac{1}{2}a\mathbf{X} - \tfrac{1}{2}\sqrt{3}a\mathbf{Y} \\
\mathbf{A2} &= \tfrac{1}{2}a\mathbf{X} + \tfrac{1}{2}\sqrt{3}a\mathbf{Y} \\
\mathbf{A3} &= c\mathbf{Z}
\end{aligned}$$

Basis Vectors:

$$\begin{aligned}
\mathbf{B1} &= 0 && && (2a) \\
\mathbf{B2} &= \tfrac{1}{2}\mathbf{A3} && = \tfrac{1}{4}c\mathbf{Z} && (2a) \\
\mathbf{B3} &= \tfrac{1}{3}\mathbf{A1} + \tfrac{2}{3}\mathbf{A2} + \tfrac{1}{4}\mathbf{A3} && = \tfrac{1}{2}a\mathbf{X} + \tfrac{1}{2}\tfrac{1}{\sqrt{3}}a\mathbf{Y} + \tfrac{1}{4}c\mathbf{Z} && (2c) \\
\mathbf{B4} &= \tfrac{1}{3}\mathbf{A1} + \tfrac{2}{3}\mathbf{A2} + \tfrac{3}{4}\mathbf{A3} && = \tfrac{1}{2}a\mathbf{X} - \tfrac{1}{2}\tfrac{1}{\sqrt{3}}a\mathbf{Y} + \tfrac{3}{4}c\mathbf{Z} && (2c)
\end{aligned}$$

The *dhcp* crystal structure has a feature that nearest neighbors and next nearest neighbors located almost at the same distances. Thus, the nearest neighbors for atom located at the origin would be sited on next z-plane at distance $\approx 0.95a$, where a is a lattice parameter. The next nearest neighbors would be located in the same xy-plane as original atom at distance a.

The different magnetic orderings could be figured out through tracking the transition of magnetic planes from fcc to dhcp structure.

The fact that distances to nearest and next nearest neighbors differs by approximately 5% leads to conclusion that J_1 and J_2 should have the same order of magnitude. Moreover, the mapping to the Heisenberg model will look like:

1. $E_{AF} = (6J_2 - 6J_1)S^2$,
2. $E_{AF}^{II} = 6J_2S^2$,
3. $E_{FERR} = -(6J_1 + 6J_2)S^2$,
4. $E_{FERR}^{II} = -(6J_1 + 6J_2)S^2$,

Then we can form system of two decoupled equations for J_1 and J_2 :

$$E_{AF} - E_{FERR} = 12J_2S^2,$$
$$E_{AF} - E_{AF}^{II} = -6J_1S^2. \tag{6.6.21}$$

The total energy curves for different magnetic orderings are shown in Figure 6.10. The results are too noisy to perform calculations for coupling parameters, especially taking into account the fact that J_1 and J_2 in dhcp structure should have close values.

The alternative way to determine the exchange constants which may be adopted for dhcp curium is reported by X. Wan *et al.* in Ref. [129]. We leave the implementation of this approach for curium for the future work. The method is based on a magnetic force theorem that evaluates linear response due to rotations of magnetic moments. This technique uses a generalized spectral density functional framework allowing one to explore several approximations ranging from local density functional to exact diagonalization based dynamical mean field theory.

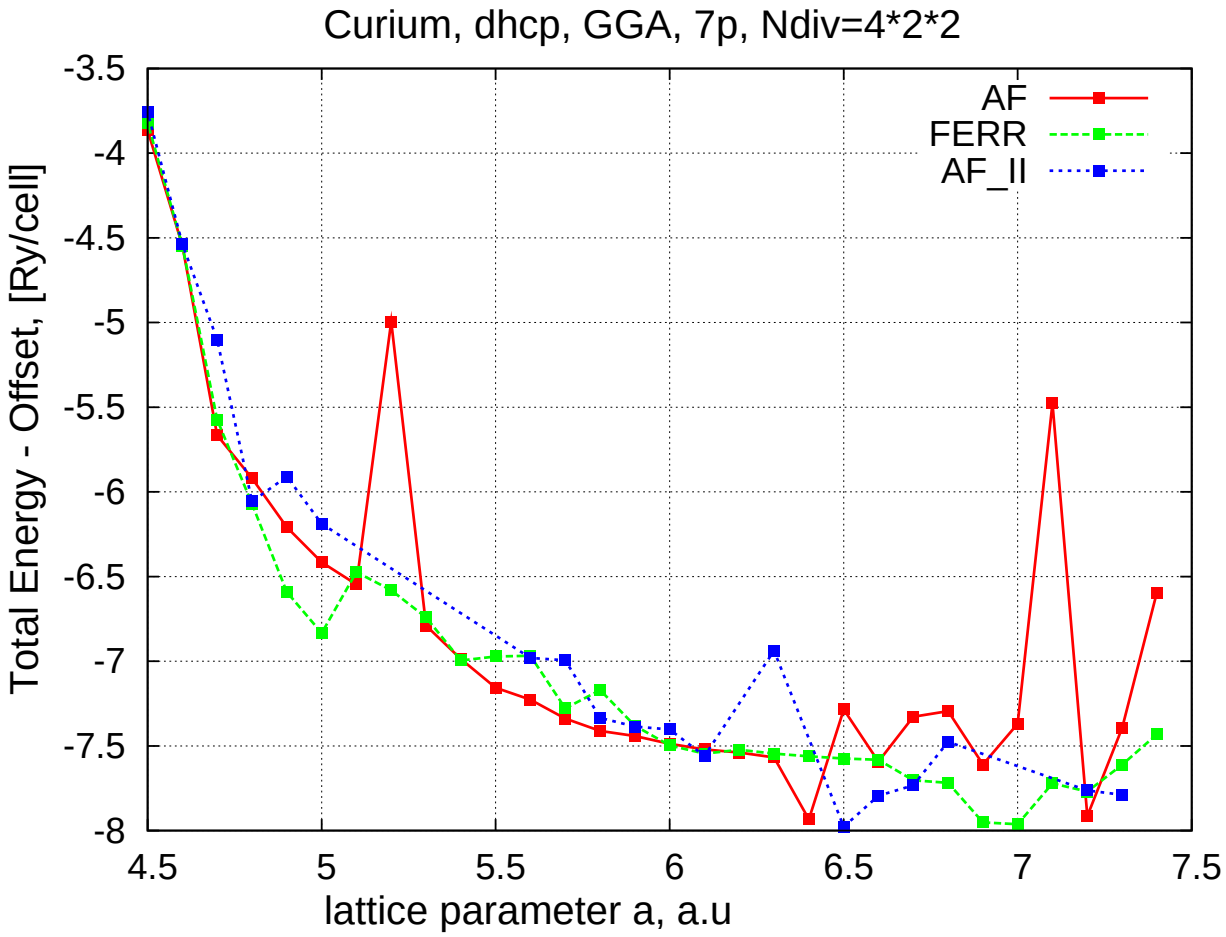

Figure 6.10: Total Energies vs lattice parameter for dhcp structure of Cm. The calculations performed within GGA, using ASA approximation. The LMTO basis with $7p$ electrons treated as valent has been used.

6.7 Conclusion

In this chapter we calculated exchange interactions for fcc curium by mapping total energies of different magnetic arrangements onto the Heisenberg model. Further, within framework of semiclassical molecular field theory we calculated Néel temperature of fcc curium. Our result is in excellent agreement with experiment. We showed that application of the same method to dhcp curium faces difficulties due to noisy total energy curves. The fact that nearest and next nearest neighbors

in dhcp structure located at very similar distances makes the described method unprecise.

Chapter 7
Summary and Conclusions

In this thesis by means of *Ab Initio* methods we studied electronic structure, magnetic and transport properties of two strongly correlated electron systems, chromium dioxide and actinide series. The fact that both systems are on the edge of localization-delocalization transition brought us to the observation that both might be discussed in the aspect of orbital selective Mott transition.

We shown that low-energy physics of CrO_2 is governed by t_{2g} orbitals of Cr atoms. We carried out detailed DMFT study with QMC as an impurity solver of the electronic structure of CrO_2 in paramagnetic case and trace its evolution in the space of two parameters: Coulomb interaction U applied to t_{2g} orbitals and relative position of narrow and broad t_{2g} bands. Keeping the later parameter fixed and increasing U we observed two subsequent localization transitions taking place first for the narrow band and then for the broad band. On the other hand the variation of relative position of narrow and broad bands at fixed value of U indicated that CrO_2 was on the edge of some type of quantum transition, since change of the relative position by as small as 0.5 eV result in completely different electronic structure and though physics.

We also performed detailed analysis of the electronic structure, optical conductivity, and magnetic anisotropy energy for the ordered phase of CrO_2 . Our study revealed that in ordered phase this compound effectively can be described as weakly correlated system due to big exchange splitting in t_{2g} block.

The second considered type of strongly correlated systems are actinide materials. First we discussed the importance of the basis for the DMFT calculations for actinides. We showed that one has to choose either well localized basis or otherwise subtract long-ranged tails of basis functions using projective orthogonalization [31].

With established robust basis set we carried out detailed one-electron band structure analysis of actinides in the example of uranium, plutonium and curium. By turning on and off hybridization between $5f$ and conducting s, p, d electrons we have shown that there is a d band crossing the Fermi level in the band structure of actinides. Hence, uncorrelated states are permanently present at the Fermi energy and both Anderson- and Hubbard-like contributions must be considered in delocalization-localization transition along $5f$ series. The outlook for future work is to provide quantitative estimate for each type of contributions.

By means of real space analysis we demonstrated that the physics of actinides is extremely local and governed by $5f$ nearest neighbor hoppings. Finally, we calculated exchange magnetic interactions and Néel temperature for fcc phase of curium metal.

References

[1] T. Hahn, ed., *International tables for crystallography. Volume A, Space-group symmetry.* D. Reidel Publishing Co., Dordrecht, Boston, 1984.

[2] K. Schwarz, "Cro_2 predicted as a half–metallic ferromagnet," *J. Phys. F: Met. Phys.*, vol. 16, pp. 16 L211–L215, 1986.

[3] M. A. Korotin, V. I. Anisimov, D. I. Khomskii, and G. A. Sawatzky, "Cro_2: A self–doped double exchange ferromagnet," *Phys. Rev. Lett.*, vol. 80, pp. 4305 – 4308, 1998.

[4] I. I. Mazin, D. J. Singh, and C. Ambrosch-Draxl, "Transport, optical, and electronic properties of the half–metal cro_2," *Phys. Rev. B*, vol. 59, pp. 411 – 418, 1999.

[5] J. Kuneš, P. Novák, P. M. Oppeneer, C. König, M. Fraune, U. Rüdiger, G. Güntherodt, and C. Ambrosch-Draxl, "Electronic structure of cro_2 as deduced from its magneto-optical kerr spectra," *Phys. Rev. B*, vol. 65, p. 165105, 2002.

[6] T. Tsujioka, T. Mizokawa, J. Okamoto, A. Fujimori, M. Nohara, H. Takagi, K. Yamaura, and M. Takano, "Hubbard splitting and electron correlation in the ferromagnetic metal cro_2," *Phys. Rev. B*, vol. 56, pp. R15509 – R15512, 1997.

[7] E. Z. Kurmaev, A. Moewes, S. M. Butorin, M. I. Katsnelson, L. D. Finkelstein, J. Nordgren, and P. M. Tedrow, "Half-metallic electronic structure of cro_2 in resonant scattering," *Phys. Rev. B*, vol. 67, p. 155105, 2003.

[8] E. J. Singley, C. P. Weber, D. N. Basov, A. Barry, and J. M. D. Coey, "Charge dynamics in the half-metallic ferromagnet cro_2," *Phys. Rev. B*, vol. 60, p. 4126, 1999.

[9] T. L. Bihan, S. Heathman, M. Idiri, G. H. Lander, J. M. Wills, A. C. Lawson, , and A. Lindbaum, "Structural behavior of α–uranium with pressures to 100 gpa," *Phys. Rev. B*, vol. 67, p. 134102(6 pages), 2003.

[10] S. Heathman, R. G. Haire, T. L. Bihan, A. Lindbaum, K. Litfin, Y. Meresse, and H. Libotte, "Pressure induces major changes in the nature of americium's 5f electrons," *Phys. Rev. Lett.*, vol. 85, p. 29612964, 2000.

[11] A. Lindbaum, S. Heathman, K. Litfin, Y. Meresse, R. G. Haire, T. L. Bihan, and H. Libotte, "High–pressure studies of americium metal: Insights into its position in the actinide series," *Phys. Rev. B*, vol. 63, p. 214101(10 pages), 2001.

[12] S. Heathman, R. G. Haire, T. L. Bihan, A. Lindbaum, M. Idiri, P. Normile, S. Li, R. Ahuja, B. Johansson, and G. H. Lander, "A high–pressure structure in curium linked to magnetism," *Science*, vol. 309, pp. 110–113, 2005.

[13] M. B. Brodsky, "Magnetic properties of the actinide elements and their metallic compounds," *Rep. Prog. Phys.*, vol. 41, pp. 1547–1608, 1978.

[14] R. Schenkel, "The electrical resistivity of ^{244} cm metal," *Solid State Communications*, vol. 23, pp. 389–92, August 1977.

[15] P. G. Huray, S. E. Nave, J.R.Peterson, , and R. G. Haire, "The magnetic susceptibility of ^{248}cm metal," *Physica B*, vol. 102, pp. 217–220, 1980.

[16] R. M. Martin, *Electronic Structure: Basic Theory and Practical Methods*. Cambridge, 2004.

[17] P. Hohenberg and W. Kohn, "Inhomogeneous electron gas," *Phys. Rev.*, vol. 136, pp. B864–B871, 1964.

[18] W. Kohn and L. J. Sham, "Self–consistent equations including exchange and correlation effects," *Phys. Rev.*, vol. 140, pp. A1133 – A1138, 1965.

[19] S. Lundqvist and N. H. March, eds., *Theory of the inhomogeneous electron gas*. New York : Plenum Press, 1983.

[20] G. Kotliar, S. Y. Savrasov, K. Haule, V. S. Oudovenko, O. Parcollet, and C. A. Marianetti, "Electronic structure calculations with dynamical mean-field theory," *Rev. Mod. Phys.*, vol. 78, pp. 865–951, 2006. for supporting materials see: http://dmft.rutgers.edu/.

[21] A. Georges, G. Kotliar, W. Krauth, and M. J. Rozenberg, "Dynamical mean–field theory of strongly correlated fermion systems and the limit of infinite dimensions," *Reviews of Modermn Physics*, vol. 68, no. 1, 1996.

[22] N. F. Mott, *Metal-insulator transitions*. Taylor & Francis, 1990.

[23] F. Gebhard, *The mott metal-insulator transition : models and methods*. New York : Springer, 1997.

[24] G. Moeller, Q. Si, G. Kotliar, M. Rozenberg, and D. Fisher, "Critical behavior near the mott transition in the hubbard model," *Phys. Rev. Lett.*, vol. 74, pp. 2082 – 2085, 1995.

[25] R. Bulla, "Zero temperature metal-insulator transition in the infinite-dimensional hubbard model," *Phys. Rev. Lett.*, vol. 83, pp. 136 – 139, 1999.

[26] R. Arita and K. Held, "Orbital-selective mott-hubbard transition in the two-band hubbard model," *Phys. Rev. B*, vol. 72, pp. 201102 –(4), 2005.

[27] A. Liebsch, "Single mott transition in the multiorbital hubbard model," *Phys. Rev. B*, vol. 70, pp. 165103–(8), 2004.

[28] L. de' Medici, A. Georges, G. Kotliar, and S. Biermann, "Mott transition and kondo screening in f–electron metals," *Phys. Rev. Lett.*, vol. 95, pp. 066402–(4), 2005.

[29] A. Georges, G. Kotliar, and Q. Si, "Strongly correlated systems in infinite dimensions and their zero dimensional counterparts," *Int. J. Mod. Phys. B*, vol. 6, pp. 705 – 730, 1992.

[30] A. Toropova, S. Savrasov, V. Udovenko, and G. Kotliar, "Magnetic anisotropy and electronic structure of cro_2," *Phys. Rev. B*, vol. 71, pp. 172403–(4), 2005.

[31] A. Toropova, C. A. Marianetti, K. Haule, and G. Kotliar, "One-electron physics of the actinides,"

[32] V. Anisimov, I. Nekrasov, D. Kondakov, T. Rice, and M. Sigrist, "Orbital-selective mott-insulator transition in $\mathrm{ca}_{2-x}\mathrm{sr}_x\mathrm{ruo}{-}4$," *Eur. Phys. J. B*, vol. 25, pp. 191–201, 2002.

[33] L. de'Medici, A. Georges, and S. Biermann, "Orbital-selective mott transition in multiband systems: Slave-spin representation and dynamical mean-field theory," *Phys. Rev. B*, vol. 72, pp. 205124–(15), 2005.

[34] J. Attema, L. Chioncel, C. Fang, G. de Wijs, and R. de Groot, *Local-Moment Ferromagnets: Unique Properties for Modern Applications*, vol. 678 of *Lecture Notes in Physics*, pp. 199–216. Springer Berlin, Heidelberg, 2005.

[35] R. Fukuda, M. Komachiya, S. Yokojima, Y. Suzuki, K. Okumura, and T. Inagaki, "Novel use of legendre transformation in field theory and many particle systems," *Prog. Theor. Phys. Suppl.*, vol. 121, p. 1, 1995.

[36] S. H. Vosko, L. Wilk, and M. Nusair, "Accurate spin-dependent electron liquid correlation energies for local spin density calculations: a critical analysis," *Can. J. Phys.*, vol. 58, pp. 1200–1211, 1980.

[37] S. Murthy, *Mott transition in strongly correlated materials : a realistic modeling using LDA+DMFT*. PhD thesis, Rutgers University, 2004.

[38] Y. Savrasov, A. Toropova, M. I. Katsnelson, A. I. Lichtenstein, V. Antropov, and G. Kotliar, "Electronic structure and magnetic properties of solids," *Zeitschrift fuer Kristallography*, vol. 220, pp. 473–488, 2005.

[39] R. Chitra and G. Kotliar, "Dynamical mean-field theory and electronic structure calculations," *Phys. Rev. B*, vol. 62, pp. 12715–12723, 2000.

[40] O. K. Andersen, "Linear methods in band theory," *Phys. Rev. B*, vol. 12, pp. 3060–3083, 1975.

[41] D. D. Koelling and B. N. Harmon, "A technique for relativistic spin-polarised calculations," *J. Phys. C: Solid State Phys.*, pp. 3107–3114, 1977.

[42] L. Nordström and D. J. Singh, "Noncollinear intra-atomic magnetism," *Phys. Rev. Lett.*, vol. 76, pp. 4420–4423.

[43] V. I. Anisimov, F. Aryastiawan, and A. I. Lichtenstein, "First-principles calculations of the electronic structure and spectra of strongly correlated systems: the lda+u method," *J. Phys.: Condens. Matter*, vol. 9, pp. 767–808, 1997.

[44] V. I. Anisimov, *Strong Coulomb Correlations in Electronic Structure Calculations: Beyond the Local Density Approximation*. CRC, 2000.

[45] V. I. Anisimov, J. Zaanen, and O. K. Andersen, "Band theory and mott insulators: Hubbard u instead of stoner i," *Phys. Rev. B*, vol. 44, pp. 943–954, 1991.

[46] K. P. Kämper, W. Schmitt, G. Güntherodt, R. J. Gambino, and R. Ruf, "Cro_2 a new half–metallic ferromagnet?," *Phys. Rev. Lett.*, vol. 59, pp. 2788 – 2791, 1987.

[47] R. J. Soulen, J. M. Byers, M. S. Osofsky, B. Nadgorny, T. Ambrose, S. F. Cheng, P. R. Broussard, C. T. Tanaka, J. Nowak, J. S. Moodera, A. Barry, and J. M. D. Coey, "Measuring the spin polarization of a metal with a superconducting point contact," *Science*, vol. 282, pp. 85 – 88, 1998.

[48] S. P. Lewis, P. B. Allen, and T. Sazaki, "Band structure and transport properties of cro_2," *Phys. Rev. B*, vol. 55, pp. 10253 – 10260, 1997.

[49] M. S. Laad, L. Craco, and E. Müller-Hartmann, "Orbital correlations in the ferromagnetic half-metal cro_2," *Phys. Rev. B*, vol. 64, p. 214421, 2001.

[50] L. Craco, M. S. Laad, and E. Müller-Hartmann, "Orbital kondo effect in cro_2: A combined local–spin–density–approximation dynamical–mean–field–theory study," *Phys. Rev. Lett.*, vol. 90, pp. 237203 – 237206, 2003.

[51] E. J. Singley, C. P. Weber, D. N. Basov, A. Barry, and J. M. D. Coey, "Charge dynamics in the half–metallic ferromagnet cro_2," *Phys. Rev. B*, vol. 60, pp. 4126 – 4130, 1999.

[52] C. B. Stagarescu, X. Su, D. E. Eastman, K. N. Altmann, F. J. Himpsel, and A. Gupta, "Orbital character of $o-2p$ unoccupied states near the fermi level in cro_2," *Phys. Rev. B*, vol. 61, pp. R9233–R9236, 2000.

[53] E. Z. Kurmaev, A. Moewes, S. M. Butorin, M. I. Katsnelson, L. D. Finkelstein, J. Nordgren, and P. M. Tedrow, "Half-metallic electronic structure of cro_2 in resonant scattering," *Phys. Rev. B*, vol. 67, no. 15, p. 155105, 2003.

[54] D. Huang, H.-T. Jeng, C. Chang, G. Guo, J. Chen, W. Wu, S. Chung, S. Shyu, C. Wu, H.-J. Lin, and C. Chen, "Orbital magnetic moments of oxygen and chromium in cro_2," *Phys. Rev. B*, vol. 66, no. 17, p. 174440, 2002.

[55] V. I. Anisimov, F. Aryasetiawan, and A. I. Lichtenstein, "First–principles calculations of the electronic structure and spectra of strongly correlated systems: the lda+ u method," *J. Phys.: Condens. Matter*, vol. 9, no. 1997, pp. 767 – 808, 9.

[56] S. Y. Savrasov, "Linear-response theory and lattice dynamics: A muffin-tin-orbital approach," *Phys. Rev. B*, vol. 54, pp. 16470–16486, 1996.

[57] B. J. Thamer, R. M. Douglass, and E. Staritzky, "The thermal decomposition of aqueous chromic acid and some properties of the resulting solid phases," *J. Am. Chem. Soc.*, vol. 79, pp. 547 – 550, 1957.

[58] D. A. Varshalovich, A. N. Moskalev, and V. K. Kheronskii, *Qunatum Theory of Angular Momentum*. Singapore: World Scientific, 1989.

[59] S.-K. Mo, J. D. Denlinger, H.-D. Kim, J.-H. Park, J. W. Allen, A. Sekiyama, A. Yamasaki, K. Kadono, S. Suga, Y. Saitoh, T. Muro, P. Metcalf, G. Keller, K. Held, V. Eyert, V. I. Anisimov, and D. Vollhardt, "Prominent quasiparticle peak in the photoemission spectrum of the metallic phase of v_2o_3," *Phys. Rev. Lett.*, vol. 90, p. 186403, 2003.

[60] J. Kuneš, P. Novák, P. M. Oppeneer, C. König, M. Fraune, U. Rüdiger, G. Güntherodt, and C. Ambrosch-Draxl, "Electronic structure of cro_2 as deduced from its magneto-optical kerr spectra," *Phys. Rev. B*, vol. 65, p. 165105, 2002.

[61] B. L. Chamberland, "The chemical and physical properties of cro_2 and tetravalent chromium oxide derivatives,"

[62] L. Spinu, H. Srikanth, A. Gupta, X. W. Li, and G. Xiao, "Probing magnetic anisotropy effects in epitaxial cro_2 thin films," *Phys. Rev. B*, vol. 62, pp. 8931 – 8934, 2000.

[63] F. Y. Yang, C. L. Chien, E. F. Ferrari, X. W. Li, G. Xiao, and A. Gupta, "Uniaxial anisotropy and switching behavior in epitaxial cro_2 films," *Appl. Phys. Lett.*, vol. 77, pp. 286–288, 2000.

[64] X. W. Li, A. Gupta, and G. Xiao, "Influence of strain on the magnetic properties of epitaxial (100) chromium dioxide (cro_2) films," *Appl. Phys. Lett.*, vol. 75, pp. 713–715, 1999.

[65] a. S. Y. S. I. Yang and G. Kotliar, "Importance of correlation effects on magnetic anisotropy in fe and ni," *Phys. Rev. Lett.*, vol. 87, p. 216405, 2001.

[66] J. Trygg, B. Johansson, O. Eriksson, and J. M. Wills, "Total energy calculation of the magnetocrystalline anisotropy energy in the ferromagnetic $3d$ metals," *Phys. Rev. Lett.*, vol. 75, pp. 2871–2874, 1995.

[67] S. Froyen, "Brillouin–zone integration by fourier quadrature: Special points for superlattice and supercell calculations," *Phys. Rev. B*, vol. 39, pp. 3168 – 3172, 1989.

[68] M. Methfessel and A. T. Paxton, "High-precision sampling for brillouin-zone integration in metals," *Phys. Rev. B*, vol. 40, pp. 3616–3621, 1989.

[69] L. Chioncel, H. Allmaier, E. Arrigoni, A. Yamasaki, M. Daghofer, M. I. Katsnelson, and A. I. Lichtenstein, "Half-metallic ferromagnetism and spin polarization in cro_2," *Phys. Rev. B*, vol. 75, pp. 140406(R)–(4), 2007.

[70] M. Jarrell and J. E. Gubernatis, "Bayesian inference and the analytic continuation of imaginary-time quantum monte carlo data," *Physics Reports*, vol. 269, pp. 133–195, 1996.

[71] J. Skilling, *Maximum Entropy and Bayesian methods*, p. 45. Kluwer Academic, Dordrecht, 1989.

[72] in *Plutonium Futures – the Science: Topical conference on plutonium and actinides* (K. K. S. Pillay and K. C. Kim, eds.), vol. 1, (Santa Fe, New Mexico, USA), AIP Press, July 10–13 2000.

[73] P. Soderlind, O. Eriksson, B. Johansson, J. M. Wills, and A. M. Boring, "A unified picture of the crystal structures of metals," *Nature (London)*, vol. 374, p. 524, 1995.

[74] S. Y. Savrasov, G. Kotliar, and E. Abrahams, "Correlated electrons in δ–plutonium within a dynamical mean–field picture," *Nature*, vol. 410, pp. 793–795, 2001.

[75] P. Soderlind and B. Sadigh, "Density–functional calculations of α, β, γ, δ, δ', and ϵ plutonium," *Phys. Rev. Lett.*, vol. 92, pp. 185702–(4), 2004.

[76] A. J. Freeman and G. H. Lander, eds., *Handbook on the Physics and Chemistry of the Actinides*. North–Holland, Amsterdam, 1984.

[77] J. C. Lashley, A. Lawson, R. J. McQueeney, and G. H. Lander, "Absence of magnetic moments in plutonium," *Phys. Rev. B*, vol. 72, p. 054416, 2005.

[78] H. L. Skriver, O. K. Andersen, and B. Johansson, "Calculated bulk properties of the actinide metals," *Phys. Rev. Lett.*, vol. 41, pp. 42–45, 1978.

[79] O. Eriksson, J. D. Becker, A. V. Balatsky, and J. M. Wills, "Novel electronic configuration in δ–pu," *Journal of Alloys and Compounds*, vol. 287, pp. 1–5, 1999.

[80] B. Johansson, "Nature of the $5f$ electrons in the actinide series," *Phys. Rev. B*, vol. 11, pp. 2740 – 2743, 1975.

[81] B. Johansson, "Structural and electronic relationships between the lanthanide and actinide elements," *Hyperfine Interactions*, vol. 128, pp. 41–66(26), 2000.

[82] L. Vitos, J. Kollár, and H. L. Skriver, "Ab initio full charge–density study of the atomic volume of α–phase fr, ra, ac, th, pa, u, np, and pu," *Phys. Rev. B*, vol. 55, pp. 4947–4952, 1997.

[83] J. Kollár and L. Vitos, "Anomalous atomic volume of α-pu.," *Phys. Rev. B*, vol. 55, pp. 15353 – (3), 1997.

[84] P. Söderlind, O. Eriksson, B. Johansson, and J. M. Wills, "Electronic properties of f-electron metals using the generalized gradient approximation," *Phys. Rev. B*, vol. 50, pp. 7291 – 7294, 1994.

[85] P. Söderlind, J. M. Wills, B. Johansson, and O. Eriksson, "Structural properties of plutonium from first–principles theory," *Phys. Rev. B*, vol. 55, pp. 1997 – 2004, 1997.

[86] J. van Ek, P. A. Sterne, and A. Gonis, "Phase stability of plutonium," *Phys. Rev. B*, vol. 48, pp. 16280 – 16289, 1993.

[87] M. D. Jones, J. C. Boettger, R. C. Albers, and D. J. Singh, "Theoretical atomic volumes of the light actinides," *Phys. Rev. B*, vol. 61, pp. 4644 – 4650, 2000.

[88] V. I. Anisimov, A. O. Shorikov, and J. Kuneš, "Magnetic state and electronic structure of plutonium from "first principles" calculations," *J. Alloys Compd.*, vol. doi:10.1016/j.jallcom.2006.10.150, 2006.

[89] A. Svane, L. Petit, Z. Szotek, and W. M. Temmerman, "Self–interaction correlated local spin density theory of $5f$ electron localization in actinides,"

[90] S. Y. Savrasov and G. Kotliar, "Ground state theory of δ–pu," *Phys. Rev. Lett.*, vol. 84, pp. 3670 – 3673, 2000.

[91] J. Bouchet, B. Siberchicot, F. Jollet, and A. Pasturel, "Equilibrium properties of δ-pu: Lda+u calculations (lda $\equiv$ local density approximation)," *J. Phys.: Condens. Matter*, vol. 12, pp. 1723–1733, 2000.

[92] A. O. Shorikov, A. V. Lukoyanov, M. A. Korotin, and V. I. Anisimov, "Magnetic state and electronic structure of the and phases of metallic pu and its compounds," *Phys. Rev. B*, vol. 72, pp. 024458–(18), 2005.

[93] A. B. Shick, V. Drchal, and L. Havela, ""coulomb–u and magnetic moment collapse in δ–pu," *Europhys. Lett.*, vol. 69, pp. 588–594, 2005.

[94] A. Shick, L. Havela, J. Koloren, V. Drchal, T. Gouder, and P. Oppeneer, "Electronic structure and nonmagnetic character of δ-pu-am alloys," *Phys. Rev. B*, vol. 73, pp. 104415–(4), 2006.

[95] L. Pourovskii, M. Katsnelson, A. Lichtenstein, L. Havela, T. Gouder, F. Wastin, A. Shick, V. Drchal, and G. Lander, "Nature of non-magnetic strongly-correlated state in δ-plutonium," *Europhys. Lett.*, vol. 74, pp. 479–485, 2006.

[96] L. V. Pourovskii, G. Kotliar, M. I. Katsnelson, and A. I. Lichtenstein, "Dynamical mean–field theory investigation of specific heat and electronic structure of α– and δ–plutonium," *Phys. Rev. B*, vol. 75, pp. 235107–(5), 2007.

[97] J.-X. Zhu, A. K. McMahan, M. D. Jones, T. Durakiewicz, J. J. Joyce, J. M. Wills, and R. C. Albers, "Spectral properties of δ–plutonium: Sensitivity to $5f$ occupancy,"

[98] J. H. Shim, K. Haule, and G. Kotliar, "What is the valence of a correlated solid? the double life of δ–plutonium,"

[99] W. A. Harrison, "Electronic structure of f–shell metals," *Phys. Rev. B*, vol. 28, pp. 550–559, 1983.

[100] W. A. Harrison and G. K. Straub, "Electronic structure and properties of d– and f–shell compounds," *Phys. Rev. B*, vol. 36, pp. 2695–2706, 1987.

[101] B. Johansson *Philos. Mag.*, vol. 30, p. 469, 1974.

[102] a. A. V. T. M. I. Katsnelson, I. V. Solovyev, "α–δ transition in plutonium as a mott transition in an f subsystem," *JETP Letters*, vol. 56, pp. 272–276, 1992.

[103] L. Severin, ""critical u/w" in f–shell metals," *Rhys. Rev. B*, vol. 46, pp. 7905–7908, 1992.

[104] R. Jullien, E. G. d'Agliano, and B. Coqblin, "Hybridized nondegenerate $6d$ and $5f$ virtual–bound–states model for actinides metals," *Phys. Rev. B*, vol. 6, pp. 2139 – 2155, 1972.

[105] R. Jullien and B. Coqblin, "Study of the d–f hybridization in actinide metals and alloys," *Phys. Rev. B*, vol. 8, pp. 5263 – 5271, 1973.

[106] K. Held, C. Huscroft, R. T. Scalettar, and A. K. McMahan, "Similarities between the hubbard and periodic anderson models at finite temperatures," *Phys. Rev. Lett.*, vol. 85, pp. 373 – 376, 2000.

[107] I. V. Solovyev, "First-principles wannier functions and effective lattice fermion models for narrow-band compounds," *Phys. Rev. B*, vol. 73, pp. 155117–(28), 2006.

[108] H. L. Skriver, *The LMTO Method*. Springer, Berlin, 1984.

[109] O. K. Andersen and O. Jepsen, "Explicit, first–principles tight–binding theory," *Phys. Rev. Lett.*, vol. 53, no. 27, pp. 2571–2574, 1984.

[110] P. Löwdin, "On the non-orthogonality problem connected with the use of atomic wave functions in the theory of molecules and crystals," *The Journal of Chemical Physics*, vol. 18, pp. 365–375, 1950.

[111] K. Haule, "Private communications with kristjan haule," tech. rep., 2006–.

[112] I. Turek, V. Drchal, J. Kudrnovsky, M. Sob, and P. Weinberger, *Electronic Structure of Disordered Alloys, Surfaces and Interfaces*. Springer, 1996.

[113] K. T. Moore, G. van der Laan, R. G. Haire, M. A. Wall, A. J. Schwartz, and P. Söderlind, "Emergence of strong exchange interaction in the actinide series: The driving force for magnetic stabilization of curium," *Phys. Rev. Lett.*, vol. 98, p. 236402, 2007.

[114] K. T. Moore, P. Soderlind, A. J. Schwartz, and D. E. Laughlin, "Symmetry and stability of δ plutonium: The influence of electronic structure," *Phys. Rev. Lett.*, vol. 96, p. 206402, 2006.

[115] K. T. Moore, M. A. Wall, A. J. Schwartz, B. W. Chung, D. K. Shuh, R. K. Schulze, and J. G. Tobin, "Failure of russell-saunders coupling in the 5f states of plutonium," *Phys. Rev. Lett.*, vol. 90, p. 196404, 2003.

[116] O. K. Andersen, O. Jepsen, and D. Glotzel, *Proceedings of the International School of Physics, Course LXXXIX, "Enrico Fermi" Varenna*, p. 59. North-Holland, Amsterdam, 1985.

[117] I. Paul and G. Kotliar, "Construction of localized basis for dynamical mean field theory," *European Physical Journal B: Condensed Matter Physics*, vol. 51, pp. 189–193, 2006.

[118] I. Paul, *Thermal and charge transport in correlated electron systems*. PhD thesis, Rutgers University, 2003.

[119] W. A. Harrison, *Elementary Electronic Structure (Revised Edition)*. World Scientific, 2004.

[120] W. A. Harrison and S. Froyen, "Universal linear–combination–of–atomic–orbitals parameters for d–state solids," *Phys. Rev. B*, vol. 21, pp. 3214–3221, 1980.

[121] B. Kanellakopulos, J. P. Charvillot, F. Maino, and W. Müller in *Trans–Plutonium 1975* (W. M uller and R. Lindner, eds.), pp. 181–190, Amsterdam: North–Holland, 1976.

[122] D. K. Fujita, T. C. Parsons, N. Edelstein, M. Noe, and J. R. Peterson, *Trans–Plutonium 1975*, pp. 173–179. Amsterdam: North–Holland, 1976.

[123] J. Kuneš, W. Ku, and W. E. Pickett, "Exchange coupling in eu monochalcogenides from first principes," *arXiv:cond–mat/0406229v1*, 2004.

[124] A. H. Morrish, *The Physical Principals of Magnetism*. New York: IEEE Press, 2001.

[125] J. Donohue, *The Structures of the Elements*. New York: John Wiley & Sons, 1974. reprint edition Robert E. Krieger, Malabar, Florida (1982).

[126] N. W. Ashcroft and N. D. Mermin, *Solid State Physics*, p. 77. Holt, Rinehart, and Winston, New York, 1976.

[127] R. G. Haire, J. R. Peterson, U. Benedict, C. Dufour, , and J. P. Itiè, "X–ray diffraction of curium–248–metal under pressures of up to 52 gpa," *Journal of the Less–Common Metals*, vol. 109, pp. 71–78, 1985.

[128] J. N. Stevenson and J. R. Peterson, "Preparation and structural studies of elemental curium-248 and the nitrides of curium-248 and berkelium-249," *Journal of the Less–Common Metals*, vol. 66, p. 201, 1979.

[129] X. Wan, Q. Yin, and S. Y. Savrasov, "Calculation of magnetic exchange interactions in mott-hubbard systems," *Phys. Rev. Lett.*, vol. 97, p. 266403, 2006.

Vita

Antonina I. Toropova

1995-2000 Baccalaureate degree in mathematical physics, the Independent University of Moscow, Moscow, Russia.

1995-2001 Master degree in physics, Department of Physics, Moscow State University, Moscow, Russia.

2002-2007 Graduate studies in physics, Department of Physics and Astronomy, Rutgers University.

2004-2006 Graduate assistantship, Department of Physics and Astronomy, Rutgers University.

Publications

1. "One-Electron Physics of the Actinides" A. Toropova, C. A. Marianetti, K. Haule, G. Kotliar, Phys. Rev. B 76, 155126 (2007)

2. "Magnetic Anisotropy and Electronic Structure of CrO2" A. Toropova, S. Savrasov, V. Udovenko, and G. Kotliar, Phys. Rev. B 71, 172403 (2005).

3. "Electronic Structure and Magnetic Properties of Solids" S. Y. Savrasov, A. Toropova, M. I. Katsnelson, A. I. Lichtenstein, V. Antropov, G. Kotliar, Z. Kristallogr. 220 (2005) 473488, arXiv:0409704.